

DESIGN AND EVALUATION OF A DIRECT DRIVE DUAL AXIS COUNTER  
ROTATING HYDROKINETIC DARRIEUS TURBINE SYSTEM

by

John Martin Crooks Jr.

A thesis submitted to the faculty of  
The University of North Carolina at Charlotte  
in partial fulfillment of the requirements  
for the degree of Master of Science in  
Mechanical Engineering

Charlotte

2022

Approved by:

---

Dr. Rodward L. Hewlin Jr.

---

Dr. Bamdad Lessani

---

Dr. Praveen Ramaprabhu

©2022  
John Martin Crooks Jr.  
ALL RIGHTS RESERVED

## ABSTRACT

JOHN MARTIN CROOKS JR.. Design and Evaluation of a Direct Drive Dual Axis Counter Rotating Hydrokinetic Darrieus Turbine System. (Under the direction of DR. RODWARD L. HEWLIN JR.)

The proposed work aims to design and develop a novel direct drive parallel stream counter-rotating Darrieus turbine system capable of producing power at low velocities (less than 2.0 m/s) for scientific and industrial applications along an intercoastal environment. This system consists of two Darrieus rotors arranged parallel and horizontally to the water stream and operate in counter-rotation due to the incoming flow. The parallel rotor design aims to work with one rotor directly driving an armature coil rotor and the other with a permanent magnet generator. The gearbox removal eliminates the mechanical losses due to friction; however, also reduces the rotational speed at which the generator spins. The parallel Darrieus rotor design is designed to rectify this by increasing the speed at which the generator effectively spins. A two-dimensional (2D) and three-dimensional (3D) computational fluid dynamic (CFD) simulation study assessed the hydrokinetic performance of the design. A scaled experimental design prototype was developed with two solid 3D printed cylinders serving as a surrogate for the armature coil and the permanent magnet rotor. The prototype was deployed in a water channel for static (non-movement of the rotors with the fluid flow) particle image velocimetry (PIV) studies. The PIV studies validate and verify the accuracy of the CFD simulations. This paper outlines the prototype development, PIV experimental setup and results, computational simulation setup and results, and additional recommendations for future work that could improve the overall performance of the proposed design.

## ACKNOWLEDGEMENTS

I would like to acknowledge my profound gratitude to Dr. Rodward L. Hewlin Jr. for his guidance, expertise, and support throughout this research. I would like to thank Dr. Bamdad Lessani and Dr. Praveen Ramaprabhu for their valuable inputs and for serving on my thesis committee. I would also like to thank Dr. Jerry Dahlberg for all of the technical expertise and helpful advice on the setup of the PIV experimentation in the water channel. A big thanks go to the UNC Charlotte High-Performance group and especially Jon Halter for helping with any issues with running simulations on the cluster. I would also like to thank Mr. Joel Pritchard of the UNC Charlotte Engineering and Construction Management (ETCM) machine shop for his help with machining parts for the DD-VADHT prototype. I would also like to gratefully acknowledge the North Carolina Renewable Ocean Energy Program for funding the research and making the building and testing of the physical prototype possible.

## TABLE OF CONTENTS

LIST OF TABLES	viii
LIST OF FIGURES	ix
LIST OF SYMBOLS	xiii
CHAPTER 1: INTRODUCTION	1
1.1. Renewable Energy	1
1.2. Turbines	2
1.2.1. Axial Flow vs. Cross Flow Turbines	2
1.2.2. Types of Vertical Axis Turbines	3
1.2.3. Advantages of Vertical Axis Turbines	5
1.3. Problem Statement and Specific Objectives	7
1.4. Organization of Thesis	7
CHAPTER 2: Literature Review	8
2.1. Computational Models	8
2.2. CFD in Vertical Axis Turbine Analysis	10
2.3. Counter-Rotating Turbines	11
CHAPTER 3: BACKGROUND	15
3.1. Fluid Flow Theory	15
3.1.1. Navier-Stokes Equations	15
3.1.2. Turbulence Modeling	15
3.1.3. Reynolds-Averaged Navier-Stokes Equations	17
3.1.4. Turbulence Modeling	18

	vi
3.1.5. Q-criterion	19
3.2. Hydrodynamics of Vertical-Axis Darrieus Turbines	21
3.3. Turbine Parameters	25
3.4. Particle Image Velocimetry Theory	26
CHAPTER 4: METHODOLOGY	29
4.1. Prototype Design	29
4.1.1. Prototype Frame Subassembly	30
4.1.2. Turbine Rotor Subassembly	31
4.1.3. Surrogate Generator Subassembly	35
4.2. Numerical Simulation Setup	36
4.2.1. CFD Turbine Geometry	37
4.2.2. Computational Domain and Boundary Conditions	39
4.2.3. 3D Mesh Generation	41
4.2.4. 2D Mesh Generation	48
4.3. Particle Image Velocimetry Setup	51
4.3.1. UNCC Water Channel	51
4.3.2. Prototype Adaptions to Water Channel	53
4.3.3. Mirror Setup	56
4.3.4. Prototype Adaptions for Steady-State Experiment	58
4.3.5. Model Surface Preparation	62
4.3.6. PIV Equipment	63
4.3.7. PIV Settings	64
4.3.8. PIV Software	65

	vii
CHAPTER 5: RESULTS	66
5.0.1. PIV Results	67
5.0.2. 3D CFD Simulation	70
5.1. 2D CFD Simulations	72
5.1.1. Mesh Independence Study	72
5.1.2. Tip Speed Ratio Study	79
5.1.3. Torque Ripple	85
5.1.4. Flow Field Analysis	87
5.1.5. Dynamic Performance Analysis	92
CHAPTER 6: CONCLUSIONS	96

## LIST OF TABLES

TABLE 3.1: List of k- $\epsilon$ model constants	19
TABLE 3.2: Prototype turbine parameters	25
TABLE 4.1: PIV configuration and setting parameters	65
TABLE 5.1: Mesh Independence Results	73
TABLE 5.2: Percent Difference	77
TABLE 5.3: Tip speed ratios and average coefficient of power over a single revolution	80
TABLE 5.4: Small-scale and full-scale turbine geometry parameters	93

## LIST OF FIGURES

FIGURE 1.1: Horizontal axis vs. vertical axis turbine diagram. Obtained from the work of Al-Kharbosity [29].	3
FIGURE 1.2: Schematic of types of vertical axis turbines : (a) Savonius (b) Darrieus (c) H-Darrieus (d) Gorlov Helix shape. Obtained from the work Castellan et al. [31].	5
FIGURE 1.3: Velocity streamline straightening effect on farm configuration. Obtained from the work of Antheaume et al. [32].	6
FIGURE 3.1: Diagram of velocity vectors and azimuthal position on a Darrieus turbine. Obtained from the work of Hall [63]	23
FIGURE 3.2: Angle of attack vs. azimuthal angle.	24
FIGURE 3.3: General particle image velocimetry experimental setup. Obtained from the work of Murgan et al. [64]	26
FIGURE 3.4: Position of particles in two frames in consecutive time steps during PIV. Obtained from the work of Raffel et al. [65]	27
FIGURE 3.5: Raw PIV image of flow over a wedge. Obtained from the work of Raffel et al. [65]	28
FIGURE 3.6: Post-processed image of flow over a wedge with velocity vectors and vorticity contours. Obtained from the work of Raffel et al.[65]	28
FIGURE 4.1: CAD model of prototype turbine system	30
FIGURE 4.2: Physical model of prototype turbine system	30
FIGURE 4.3: CAD model of frame subassembly of prototype system	31
FIGURE 4.4: Physical frame subassembly	31
FIGURE 4.5: CAD model of turbine subassembly of prototype system	32
FIGURE 4.6: CAD model of turbine blade with mounting points for carbon fiber supports	33
FIGURE 4.7: 3D printed turbine blades	33

FIGURE 4.8: Carbon fiber support CAD model for turbine blades	33
FIGURE 4.9: Central hub for turbine rotor	34
FIGURE 4.10: Physical carbon fiber supports for turbine blades	34
FIGURE 4.11: Surrogate generator subassembly of prototype system	35
FIGURE 4.12: Physical 3D printed surrogate generator subassembly of prototype system	35
FIGURE 4.13: CAD model of prototype turbine system used for PIV experimentation	37
FIGURE 4.14: Simplified CAD model of turbine system used for CFD simulation	37
FIGURE 4.15: Close-up image of the connection between the blades and supports in PIV prototype	38
FIGURE 4.16: Close-up image of simplified geometry between blades and supports in CFD model	38
FIGURE 4.17: Isometric view of full 3D CFD turbine system	39
FIGURE 4.18: Fixed computational domain dimensions	40
FIGURE 4.19: Rotating computational domains	40
FIGURE 4.20: Isometric view of surface mesh over single turbine system	41
FIGURE 4.21: Cross-section view of mesh around turbine blades on $xy$ -plane	43
FIGURE 4.22: Isometric view of surface mesh on turbine blades	43
FIGURE 4.23: Isometric view of full turbine system with a cross-section of mesh on $xy$ -plane	44
FIGURE 4.24: Cross-section view of rotating domain on $xy$ -plane	45
FIGURE 4.25: Cross-section view of close volumetric wake refinement on $xy$ -plane	46

FIGURE 4.26: Cross-section view of far volumetric wake refinement on $xy$ -plane	46
FIGURE 4.27: Isometric view of wall $y^+$ over single turbine system	47
FIGURE 4.28: Final 2D mesh around blades	49
FIGURE 4.29: Wall $y$ -plus values over the surface of 2D blades	50
FIGURE 4.30: Mesh of rotating domain for the 2D CFD simulations	50
FIGURE 4.31: Schematic view of UNCC water channel. Obtained from the work of Hellman [66]	52
FIGURE 4.32: Frame adaptations made to original prototype frame	54
FIGURE 4.33: Close-up image of slotted rails on the water channel walls	55
FIGURE 4.34: Schematic of laser setup used for PIV experiment	57
FIGURE 4.35: Mirror assembly used to position laser sheet at prototype model	58
FIGURE 4.36: Original PIV prototype setup	61
FIGURE 4.37: Revised PIV prototype setup	61
FIGURE 4.38: Final PIV prototype model setup	62
FIGURE 4.39: Laser used in PIV experiments	64
FIGURE 5.1: PIV velocity vector and contour reconstructed image	68
FIGURE 5.2: CFD velocity vector and contour plots	68
FIGURE 5.3: PIV and CFD velocity profile extraction in wake region behind turbine blades	69
FIGURE 5.4: ISO-surface of Q-Criterion = $75.0 / s^2$ with a velocity magnitude scalar overlaid	71
FIGURE 5.5: Baseline mesh around the cross-section of turbine blade	74
FIGURE 5.6: M1 mesh around the cross-section of turbine blade	74

FIGURE 5.7: M2 mesh around the cross-section of turbine blade	74
FIGURE 5.8: M3 mesh around the cross-section of turbine blade	74
FIGURE 5.9: Power coefficient vs. mesh size for steady mesh independence study	76
FIGURE 5.10: Percent error plot from previous mesh for steady simulation	76
FIGURE 5.11: Power coefficient vs azimuth angle for mesh sizes	78
FIGURE 5.12: Coefficient of power as a function of tip speed ratio	81
FIGURE 5.13: Power coefficient for the tip speed ratio of $\lambda = 2.75$	82
FIGURE 5.14: Power coefficient plots for $\lambda = 2.5$ , $\lambda = 2.75$ , and $\lambda = 3$	83
FIGURE 5.15: Individual blade vs combined power coefficient over a single revolution	84
FIGURE 5.16: Torque coefficient for the tip speed ratio of $\lambda = 2.75$	85
FIGURE 5.17: Torque ripple factor as a function of tip speed ratio	86
FIGURE 5.18: Instantaneous pressure coefficient contours	88
FIGURE 5.19: Instantaneous velocity magnitude contours	90
FIGURE 5.20: Pressure coefficient contours for the right turbine over a third of a revolution from $\theta = 15$ to $\theta = 135$	91
FIGURE 5.21: Power output as a function of turbine radius for various tip speed ratios	94

## LIST OF SYMBOLS

$\alpha$	Angle of Attack
$\delta_{ij}$	Kronecker Delta
$\kappa$	Turbulent Kinetic Energy
$\lambda$	Tip Speed Ratio
$\mu$	Dynamic Viscosity
$\nu$	Kinematic Viscosity
$\nu_t$	Eddy Viscosity
$\omega$	Angular Velocity
$\overline{S_{ij}}$	Mean Strain Rate Tensor
$\rho$	Fluid Density
$\tau_w$	Shear Stress
$\theta$	Azimuthal Angle
$A_{ref}$	Reference Area
$c$	Chord Length
$C_P$	Coefficient of Power
$C_T$	Coefficient of Torque
$g_i$	Body Accelerations Acting on the Continuum
$H$	Height of Turbine
$N$	Number of Blades

$P$	Power
$P_0$	Power Available
$Q$	Q-criterion
$R$	Radius of Turbine
$Re_0$	Freestream Reynolds Number
$Re_{rel}$	Relative Reynolds Number
$T$	Torque
$TRF$	Torque Ripple Factor
$U_\infty$	Freestream Velocity
$u_\tau$	Friction Velocity
$V_\theta$	Resultant Velocity Vector
$V_R$	Tangential Velocity of the Blade
$y$	Distance to Wall
$y^+$	Wall Y-Plus Value

## CHAPTER 1: INTRODUCTION

### 1.1 Renewable Energy

Conventional fossil fuel sources such as coal, oil, and natural gas have proven to be highly effective in generating energy on demand. They have been a driver of economic progress worldwide; however, several significant drawbacks to these energy sources have led to seeking alternatives [1–4]. Fossil fuels are compounds of hydrocarbons found in the earth’s crust and are derived from the remains of dead organic matter. This process occurs over millions of years and leads to an inherently finite resource. There are many predictions of when fossil fuels will completely be depleted, but there are estimates that oil and natural gas reserves could be exhausted by 2042 and coal in 2112 [5]. The other drawback of burning fossil fuels is the adverse environmental effects. Combustion of these fuels produces many harmful byproducts, including but not limited to carbon dioxide and fine particulate matter [6–8]. Greenhouse gases produced by these conventional fossil fuels are one of the leading causes of climate change. Estimates show that  $CO_2$  concentration has increased by around 48% since 1750 [9]. Air pollution generated from these fuels in the form of particulate matter is also very harmful to human health. Research indicates that up to 9 million people die annually from fine airborne particulate matter [10]. Due to these reasons, there has been a substantial increase in research on energy sources that are clean and renewable. The main area of renewable energy research is how to increase their efficiency and decrease their cost compared to fossil fuels. Renewable energies are any energy source that can be replenished by nature on a human time scale. They can be derived directly from the sun (solar energy), indirectly from the sun (wind energy and hydropower), or the natural mechanics of the earth (tidal and geothermal energy) [11].

Numerous forms of renewable energy are currently used at scale to generate electricity, including hydropower, wind energy, solar energy, bioenergy, geothermal energy, and marine energy. Among the above options, marine energy has the advantage of being predictable, stable during the day and night, and has a higher energy density than wind and solar energies [12]. There are two main types of ocean power: wave and tidal power [13]. Wave power takes advantage of the kinetic energy of surface oceanic waves. Tidal power is generated from the rise and fall of the sea level due to the gravitational forces generated from the sun and moon combined with the rotation of the earth [14–16]. Tidal energy can be used to generate electricity directly in the power grid [17] or as a power source for water desalination plants [18]. The theoretical potential for ocean power has been estimated to be around 7,400 exajoules which would exceed current and future human energy needs [19].

## 1.2 Turbines

### 1.2.1 Axial Flow vs. Cross Flow Turbines

Tidal stream generators convert the kinetic energy of moving seawater to mechanical energy by using rotating turbines similar to wind energy [20–24]. Several turbine designs have effectively utilized hydrodynamic lift [25–28]. There are two main categories of turbine designs: axial-flow and cross-flow. Classification of turbines depends on the flow’s direction relative to the rotation axis. Figure 1.1 below shows a schematic drawing illustrating the differences between the two types. Axial flow turbines are referred to as horizontal axis turbines because the axis of rotation is parallel to the ground plane. Axial-flow is the standard for most wind applications due to its higher overall efficiency. Cross-flow turbines are referred to as vertical-axis turbines because the axis of rotation is perpendicular to the ground plane.

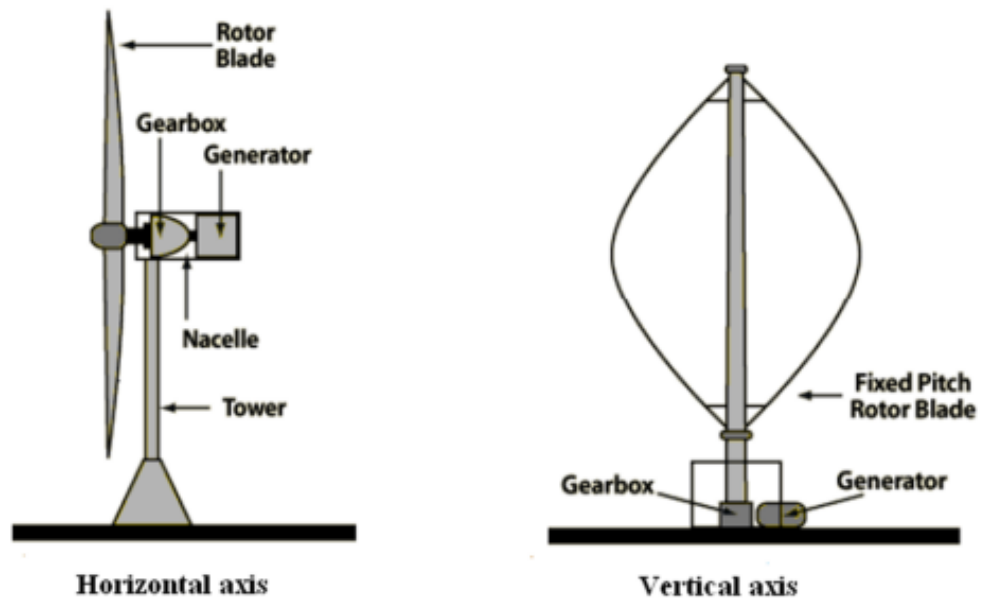


Figure 1.1: Horizontal axis vs. vertical axis turbine diagram. Obtained from the work of Al-Kharbosity [29].

### 1.2.2 Types of Vertical Axis Turbines

Cross-flow turbines utilize two types of aerodynamic forces: lift and drag. The primary drag-based vertical axis turbine is the Savonius turbine and is pictured in figure 1.2 (a). Drag-based vertical axis turbines operate due to the blades' curvature producing less drag when the turbine rotates against the wind than with the wind. Drag-based turbines are much less efficient than lift-based turbines and are, therefore, less popular in most applications. The one advantage of drag-based turbines is their superior reliability and lower cost than lift-based turbines.

Several types of vertical axis turbines utilize the lift force of airfoils. The general way these turbines operate is that during the rotation of the airfoil in a circular path, the relative oncoming flow to the blade is added to the freestream flow. The resultant vector creates a positive attack angle leading to the airfoil generating a lift force. The lift force generates a positive moment around the rotation axis, propelling the blade in the direction it is currently heading. This lift force leads to the turbine spinning

higher than the freestream velocity.

The classic design of vertical axis turbines is the Darrieus turbine [30] and is illustrated in figure 1.2 (b) below. This design consists of curved airfoils that attach to a rotating shaft's top and bottom. A variation of this design from the original patent is called a giro mill turbine or, more commonly, the H-Darrieus turbine. An image of the H-Darrieus turbine is given below in figure 1.2 (c). This design consists of straight airfoil blades that attach to the center rotating shaft via connection rods. This design is much cheaper to build due to the linear airfoil geometry; however, it is slightly less efficient.

There are a couple of problems with lift-based Darrieus turbines. The lift force is the driver of the rotation of the turbine. If a lift-based turbine is static, no net forces are acting upon it, and it will not generate torque, even if there is a high freestream velocity. This system is non-self-starting and requires energy to be put into it to start producing power. The other problem is with the distribution of the torque over the rotation. Each blade has a torque spike during a complete revolution. Over time these torque peaks can cause high stress in specific attachment areas leading to material fatigue failure.

Researchers have made many attempts to alter the Darrieus turbine design to overcome the torque pulsing and inability to self-start. The Gorlov turbine utilizes a helix shape and is presented in figure 1.2 (d). The idea behind the helix shape is that by curving the blades along the axis of rotation, the airfoil sections are distributed more evenly during a revolution. This helix geometry forms a system with an airfoil section at every possible angle of attack. The torque spikes in this system are much smaller than the original Darrieus turbine or the H-Darrieus turbine. The probability of self-starting is higher with the helix shape than with other vertical axis turbines.

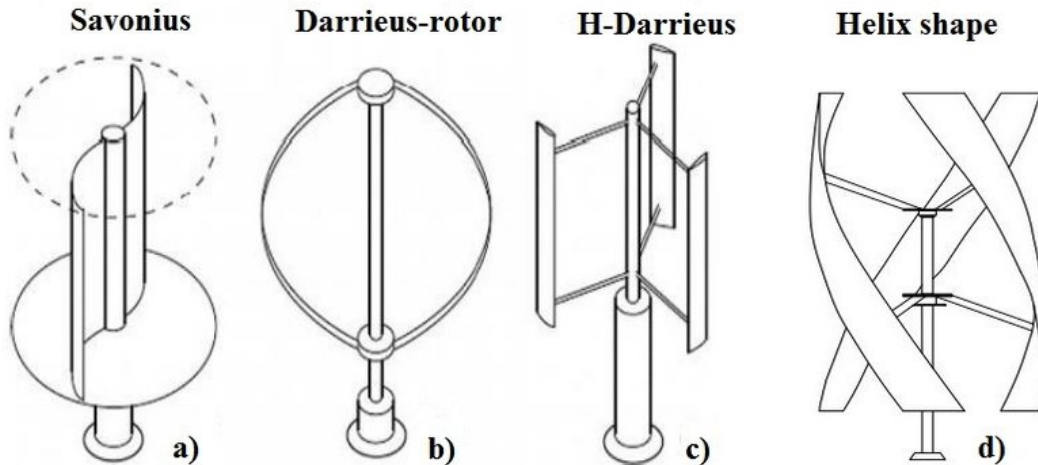


Figure 1.2: Schematic of types of vertical axis turbines : (a) Savonius (b) Darrieus (c) H-Darrieus (d) Gorlov Helix shape. Obtained from the work Castellan et al. [31].

### 1.2.3 Advantages of Vertical Axis Turbines

The main advantage of vertical axis turbines is that their design is relatively simple and easy to construct. The rectangular swept area and circular cross-sectional area of vertical axis turbines allow for close packing and higher density. When the flow encounters a high-pressure field generated from any turbine, a bypass effect occurs where the flow will curve around the swept area instead of passing through [32]. The increased packing density of vertical axis turbines allows for a decrease in this bypass effect and therefore increases individual turbine efficiency. The other benefit is that there can be a shared infrastructure. A farm of vertical axis turbines can share electric generators, reducing hardware and maintenance costs. Seawater's harsh and corrosive environment creates a need for increased maintenance; therefore, farm configurations of vertical axis turbines can keep these costs under control. Figure 1.3 below shows the straightening effect on a farm of vertical axis turbines from the work of Antheaume et al. The authors showed a 4.5 percent increase in the power coefficient for the case with five turbines over the case with a single turbine.

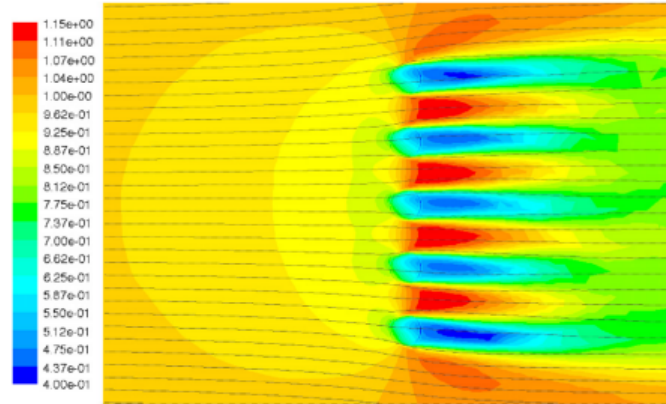


Figure 1.3: Velocity streamline straightening effect on farm configuration. Obtained from the work of Antheaume et al. [32].

The second advantage is that VAWTs do not need to be pointed in the direction of the flow [33]. Horizontal axis turbines typically need the axis of rotation to be normal to the flow direction to maximize efficiency. Complex mechanisms that will rotate the horizontal turbine in yaw to line up with the direction of oncoming flow are required. Smaller horizontal turbines employ a tail on the end and allow free rotation. Larger-scale horizontal turbines use a much more complicated system to yaw the turbine. These larger turbines contain wind direction, speed, and temperature sensors. An onboard computer processes the data and rotates the turbine in yaw to maximize the power output while keeping the rotation speed within operating conditions. This mechanism adds complexity and raises costs considerably. Vertical axis turbines do not need any of these mechanisms. Ocean horizontal axis turbines would also need to consider the harsh sea environment on flow sensor equipment and maintenance of these systems.

### 1.3 Problem Statement and Specific Objectives

The ultimate goal of the proposed work is to design and develop a novel parallel-stream counter-rotating Darrieus turbine system capable of producing power at low velocities (less than 2.0 m/s) for scientific and industrial applications along inter-coastal shoreline areas. The specific objectives for this research are listed below.

- Conduct 2D and 3D computational fluid dynamic (CFD) simulations on the proposed turbine design for flow pattern analyses and torque output.
- Develop a scaled turbine prototype to deploy in a water channel for experimental performance output and flow pattern evaluation.
- Conduct particle imaging velocimetry (PIV) analyses on the developed prototype in the water channel for verification and validation of CFD simulations.

### 1.4 Organization of Thesis

**Chapter 1:** Provides an introduction to the topic, the specific objectives of this research, and an outline of the rest of the document.

**Chapter 2:** Review of previous literature on the topic area and the areas where there are gaps in knowledge.

**Chapter 3:** Description of governing equations on fluid flow and vertical axis turbines.

**Chapter 4:** Numerical setup for CFD simulations, prototype turbine design, and particle image velocimetry setup.

**Chapter 5:** Results and discussion of various CFD studies along with verification of these studies with the experimental PIV studies.

**Chapter 6:** Concludes this research and provides information on further research on this topic.

## CHAPTER 2: Literature Review

### 2.1 Computational Models

Much research on vertical-axis turbines for wind applications has led to mathematical models being developed to predict performance and design parameters. According to Islam et al. [34], the three most common models from the literature are momentum, vortex, and cascade models. Momentum models calculate fluid velocity by equating the force on each blade with the fluid's rate of change of momentum. This rate of change of momentum is equal to the overall difference in velocity multiplied by the mass flow rate. The first momentum model was generated by Templin [35] in 1974, which utilized a single streamtube. Templin's model used the basic concept from the windmill actuator disc theory to help predict straight blade vertical axis wind turbines. The entire swept area of the turbine is enclosed in a single streamtube. The first assumption in this model is that the induced rotor axial flow velocity is constant throughout the entire disc model. The induced velocity is calculated by equating the drag in the streamwise direction with the axial momentum. In 1975, Wilson and Lissaman [36] took this single streamtube model and made improvements by incorporating multiple streamtubes. This model divided the single streamtube from Templin into a series of parallel individual streamtubes. The momentum theory is then applied to each of the individual streamtubes. In 1988 Paraschivoiu [37] improved on the multiple streamtube models by developing a double-multiple streamtube model. This model separates the calculations done in each streamtube into upstream and downstream components.

Vortex models are potential flow models that calculate the velocity field through the local vorticity on the blade's surface and in the wake region. The blades are

represented in this model by a lifting line vortex. The strength of these vortices is determined using the specific airfoil coefficients in conjunction with the blade's relative velocity and angle of attack. The model was first introduced in 1975 by Larsen [38], where the theory was used to analyze a cyclogiro windmill. This model by Larsen is two-dimensional; however, the tip vortices from the turbine blades can be considered. The angle of attack on the blade is small enough to where the stall effect is neglected in this model. The following extension on the vortex model was presented by Strickland et al. [39], where a three-dimensional model was introduced along with incorporating an aerodynamic stall. The model by Strickland et al. is termed a dynamic vortex model due to the transient effects being accounted into the calculations. The model was compared with experimental results and showed good correlations. Vortex models have a higher degree of accuracy than momentum models; however, their computational cost is much higher.

Cascade models use the cascade theory from turbomachinery and apply those principles to vertical axis turbines. Hirsch et al. [40] first proposed a cascade model. This model takes each turbine blade and positions them in a planar surface, called the cascade, and is spaced out by the circumference divided by the number of blades in the rotor. A relationship is generated between the wake and freestream velocity using Bernoulli's equation, while the induced velocity is generated as an empirical expression. The blade is broken up into elements, and similar to the double-multiple streamtube momentum model, the upstream and downstream calculations are completed independently. This model considers the local changes in Reynolds numbers on the blades and the finite aspect ratios. The cascade model works well for turbines with high tip speed ratios, and its reasonable computational cost is advantageous over the vortex and momentum models.

## 2.2 CFD in Vertical Axis Turbine Analysis

Advancements in computational resources in recent years have allowed the rise of computational fluid dynamics to be utilized in the analysis of vertical axis turbines. Mathematical models work well to give reasonable estimates of the general overall performance of a turbine; however, they use many assumptions and simplifications. CFD allows for a more accurate performance solution and a better understanding of the time-dependent flow field. There are two main ways that CFD can be implemented to emulate the motion of a vertical-axis turbine. The first method is called a moving reference frame (MRF). An MRF simulation takes an unsteady problem and simplifies the fluid flow equations to achieve a steady simulation given a constant rotational velocity. The most significant advantage is that steady simulations are typically much less computationally expensive, allowing solutions to be obtained much faster. The disadvantage is that a time-average solution is achieved, and the unsteady effects are removed. An MRF simulation is best for steady simulations with unsteady components, such as vehicles with rotating wheels. There is an application with vertical axis turbines where an MRF simulation could be used in the design phase to get rough performance estimates without running full unsteady simulations. The other motion emulation technique is a rigid body motion called a sliding mesh. A sliding mesh technique generates a time-accurate solution where the solid wall boundaries move about the rest of the stationary outer domain. In a vertical axis turbine simulation, a cylindrical body with the turbine blade geometry is prescribed a rotation rate while the rest of the domain is stationary. An internal interface is set between rotating and stationary domains, allowing mass transfer. The mesh in the rotating and stationary domains stays the same, and the rotating domain is the only motion. An unsteady solution is obtained by having a specified time step and then running a set amount of inner iterations until convergence for the individual time step. This leads to understanding the flow field throughout the entire set of azimuth positions.

There is a method termed an overset mesh which allows for two separate meshes, a near-surface mesh, and a far-surface mesh. The two meshes are overlapped, and an interpolation between the meshes is conducted to achieve the best mesh at that time step. An overset mesh is typically used when emulating motion due to the mesh having a higher quality. The overset mesh is used in cases with translation or a combination of rotation and translation. In CFD simulations, a sliding mesh method is used since there is only rotation cutting down on computational resources to re-mesh after every time-step.

Multiple studies have used this sliding mesh technique to analyze the performance of vertical-axis hydrokinetic turbines. Maitre et al. [41] analyzed a two-blade turbine using the sliding mesh technique and compared the results to experimental data. There were discrepancies between the simulated data and the measured values in the stall regime. The authors attributed this error to limits in the closure problem of the RANS model.

### 2.3 Counter-Rotating Turbines

Parametric analysis of Vertical axis Darrieus hydrokinetic turbines is necessary to find the best way to reduce the cost of manufacturing, maintenance, and increasing performance. One obvious weakness of tidal turbines is the price of manufacturing. These turbines are required to operate in seawater, which is quite costly due to the corrosive nature of the ocean. There have been attempts by designers to reduce the price of tidal turbines. Nevertheless, there should be a trade-off between reducing the price and improving or maintaining the turbine's performance. From a performance perspective, Darrieus turbines are generally installed in rivers flowing at velocities ranging from 0.5 to 2.5 m/s. Depending on the diameter, these turbines also spin at 150-500 rpm. A rotor spins at its rated speed to achieve the designed power coefficient while the generator turns at a different speed (usually higher). A gearbox manages the shaft speed and torque before the generator. However, the gearbox is

also responsible for approximately 10 percent of energy loss due to friction. Several studies have been conducted to evaluate the performance of hydrokinetic Darrieus turbine systems designs and rotor configurations.

In Clarke et al. [42], a horizontal three-blade hydrokinetic rotor was coupled to a four-blade rotor. The hydrokinetic performances were evaluated, and it was reported that the overall coefficient of hydrodynamic performance was 0.43. Usui et al. [43] developed an experimental model where the same coefficient of hydrodynamic performance was observed. Both studies suggest that series-stream counter-rotating turbines (SS-CRTs) do not improve the hydrokinetic performance coefficient over conventional designs because the rotors work as a single system extracting energy from a single flow stream. Didant et al. [44] designed a direct drive system for wind energy applications to improve the power output and rotational speed over conventional designs. The reported results demonstrated an improvement in system performance. Unlike SS-CRTs, parallel stream systems utilize the rotor capacitor more efficiently, and the system swept area is the total of both rotor areas. This theory has been investigated in only a few studies.

In the work of Janon and Boonsuk [45], the authors investigated the starting time profile of a direct-drive vertical axis Darrieus hydrokinetic turbine with an axial-flux permanent magnet generator. The turbine system was designed to reduce the overall frictional loss by eliminating the gearbox. The turbine and generator radiuses were varied, and the authors reported that the variation in radiuses influenced the total moment of inertia, the hydrodynamic torque, and the relative speed at which the winding coils cut through magnetic fields. A MATLAB code was developed to assess the starting period and performance of the turbine design. It was reported that the starting period could be split into three phases; swing rotation, transient rotation, and steady-state rotation. The starting time was different for the turbine system configurations. The larger turbine radius produces more torque and shortens the

starting time.

In the work of Janon, a MATLAB code was developed to assess the torque coefficient and ripple profiles for a hydrokinetic counter-rotating Darrieus turbine system of the same design. The author reported two significant issues with wind and hydrokinetic Darrieus turbines: friction loss and low angular velocity. Hydrokinetic Darrieus turbine designs have been developed and reported incorporating two or more horizontal turbines placed together in series, where a geared mechanism enabled the turbines to turn in the counter rotation with controlled angular velocity. This idea has one major drawback: the two turbines work within one swept area. The design investigated in the reported work combined features that never have been implemented in one system before this work. The design incorporates a direct-drive system on a pair of horizontal-axis Darrieus turbines that turn in counter-rotation to double the angular velocity. The rotors are arranged in parallel so that each rotor extracts energy from a separate stream of water. The results reported suggest that a four-blade system possessed the lowest ripple.

Several studies have been conducted about decreasing frictional losses in the rotor system, increasing the rotational speed of the rotors, and investigating starting profiles [46–49]. There have also been studies that have delved into the torque characteristics and power output profiles of single-stream systems [50–52]; however, there are no studies to the author’s knowledge that have gathered experimental or CFD data on the hydrodynamic performance of direct drive parallel-stream counter-rotating turbine systems. There is a need for investigative work to be conducted that improves the design of hydrokinetic Darrieus turbine systems that extracts energy more effectively out of a single stream of water. Although there has been computational and experimental research conducted on single axis systems [53–55], dual axis rotor systems, and hydrokinetic Darrieus turbine systems placed in series [56], there is little research solely on direct drive parallel axis Darrieus turbine systems [57].

In this work, it is hypothesized that a direct drive system would aid in eliminating a large magnitude of friction losses while operating at low angular velocities and producing low ripple. Similar to the aforementioned work, the present work aims to eliminate a large magnitude of friction loss by designing a system without a gearbox. Consequently, the system becomes a direct-drive vertical axis Darrieus hydrokinetic turbine. When the gearbox is removed from the system, it is typically expected for the generator's rotational velocity to drop to a level that is too low for power generation. To overcome the lower rotational speed from the gearbox removal, the counter-rotation of the two turbine systems is designed to help increase the overall hydrodynamic efficiency of the system in conjunction with the parallel rotors extracting flow from separate streams.

## CHAPTER 3: BACKGROUND

### 3.1 Fluid Flow Theory

#### 3.1.1 Navier-Stokes Equations

The governing equations that describe viscous fluid flow are the Navier-Stokes (N-S) equations. These equations are a set of second-order partial differential equations expressing the conservation of mass and momentum for a fluid particle. The N-S equations apply Newton's second law of motion to the fluid flow movement. Equation 3.1 represents the conservation of mass of a fluid particle. Equation 3.2 represents the conservation of momentum of a fluid particle. The Navier-Stokes equations are presented below [58, 59].

$$\frac{\partial u_i}{\partial x_i} = 0 \quad (3.1)$$

$$\rho \left( \frac{\partial u_i}{\partial t} + u_j \frac{\partial u_i}{\partial x_j} \right) = - \frac{\partial p}{\partial x_i} + \rho g_i + \mu \frac{\partial^2 u_i}{\partial x_j^2} \quad (3.2)$$

Equations 3.1 and 3.2 are both for incompressible flow conditions and are written in index notation for simplification.

#### 3.1.2 Turbulence Modeling

Turbulent flow is characterized by random and chaotic motion. Understanding and predicting turbulence is vital because most engineering applications work in this flow regime. The velocity and other scalar fields fluctuate randomly in the temporal domain and are highly disordered in the spatial domain. Turbulence creates a flow field with a large spectrum of length and time scales. Numerically solving this extensive

range of scales makes the computational cost nearly impossible for most engineering applications. A turbulence model is introduced to circumvent the high computational cost of resolving the entire range of length scales. Turbulence models vary in the size of the length scales they solve explicitly. The computational resources required are inversely proportional to the length scales that are explicitly solved. Turbulence modeling techniques are therefore classified by their computational cost.

The most computationally expensive model is called Direct Numerical Simulation (DNS). DNS does not model any turbulence, so the length and time scales must all be resolved. A DNS must resolve the smallest dissipative scales known as the Kolmogorov scales  $\eta = (\nu^3/\epsilon)^{1/4}$ . Since DNS resolves the smallest scales of a flow, it can be used to run numerical experiments and allows data to be collected that traditional flow experimentation, such as particle image velocimetry, cannot achieve. DNS, however, is computationally cost-prohibitive and can only be applied to simple geometries such as a wall-mounted cube and, therefore, cannot be used in most industrial applications.

The next model used to numerically solve the N-S equations is the Large Eddy Simulation (LES). An LES simulation reduces the computational cost by ignoring the smallest scales of a flow and only resolves the largest scales. This determination is achieved by applying a low-pass filter to the general Navier-Stokes equations. LES was first introduced to simulate atmospheric conditions and air currents since the small scales are ignored, and the interest is on the pattern of the largest scales. This approach of LES has been applied further to engineering applications such as combustion and areas solving the large scales of turbulent flow is required. This approach is less computationally expensive than DNS but is limited by the computational resources available.

The most widely used approach to solve these equations numerically is to time average the Navier stokes equations leading to the Reynolds-averaged Navier-Stokes equations (RANS). The RANS model is the least computationally expensive because

none of the length scales are resolved explicitly. All length scales are modeled in the RANS approach, which leads to lower computational expense.

### 3.1.3 Reynolds-Averaged Navier-Stokes Equations

The Reynolds-averaged Navier-Stokes equations (RANS) are based on decomposing an instantaneous quantity into a mean value and a fluctuating value. This mathematical technique is called Reynolds decomposition and is represented below in equation 3.3.

$$u_i = \overline{u_i} + u_i' \quad (3.3)$$

Substituting equation 3.3 into the Navier-Stokes equations of conservation of mass and momentum and then time-averaging the resultant equation yields the Reynolds-averaged Navier-Stokes equations. Equation 3.4 below is the RANS continuity equation and is almost identical to the general conservation of mass of the Navier-Stokes equations. The RANS conservation of momentum equations is equation 3.5 below. Equation 3.6 below represents the strain rate tensor based on the mean velocity.

$$\frac{\partial \overline{u_i}}{\partial x_i} = 0 \quad (3.4)$$

$$\frac{\partial \overline{u_i}}{\partial t} + \overline{u_j} \frac{\partial \overline{u_i}}{\partial x_j} = -\frac{1}{\rho} \frac{\partial \overline{p}}{\partial x_i} + 2\nu \frac{\partial \overline{S_{ij}}}{\partial x_j} + \frac{\partial}{\partial x_j} \left( -\overline{u_i' u_j'} \right) \quad (3.5)$$

$$\overline{S_{ij}} = \frac{1}{2} \left( \frac{\partial \overline{u_i}}{\partial x_j} + \frac{\partial \overline{u_j}}{\partial x_i} \right) \quad (3.6)$$

A non-linear term appears in equation 3.5, which, when multiplied by the fluid density ( $\rho$ ), yields the term in equation 3.7. This term, called the Reynolds stress term, is the main challenge in simulating turbulent flow fields. This new term creates the closure problem with ten unknowns and four equations. A model that will describe

this Reynolds stress as a function of only the mean velocity and remove the fluctuating component must be introduced.

$$-\overline{\rho u'_i u'_j} \quad (3.7)$$

### 3.1.4 Turbulence Modeling

The most common turbulence model for solving the RANS equations is the k-  $\epsilon$  model. The k-  $\epsilon$  model is a two-equation model that describes turbulent flow with two transport equations. One transport equation is for the turbulent kinetic energy ( $k$ ), and the second is for the rate of dissipation of turbulent kinetic energy ( $\epsilon$ ) [60] [61].

The k-  $\epsilon$  model and some other turbulence models are based on the concept of eddy viscosity. The eddy viscosity model is used to overcome the closure problem by relating the turbulence stress to the mean flow. Equation 3.8 below shows the eddy viscosity model and its relationship to the Reynolds stresses.

$$-\overline{u'_i u'_j} = 2\nu_t \overline{S_{ij}} - \frac{2}{3}\kappa \delta_{ij} \quad (3.8)$$

With  $\nu_t$  as the eddy viscosity,  $\overline{S_{ij}}$  as the mean strain rate tensor,  $\kappa$  as the turbulent kinetic energy, and  $\delta_{ij}$  as the Kronecker delta.

The two transport equations for the k-  $\epsilon$  are listed below. Equation 3.9 below is the transport equation for the turbulent kinetic energy. Equation 3.10 below is the transport equation rate of dissipation of turbulent kinetic energy.

$$\frac{\partial \kappa}{\partial t} + \frac{\partial \overline{u_j \kappa}}{\partial x_j} = \frac{\partial}{\partial x_j} \left( \left( \nu + \frac{\nu_t}{\sigma_\kappa} \right) \frac{\partial \kappa}{\partial x_j} \right) - \epsilon + P \quad (3.9)$$

$$\frac{\partial \epsilon}{\partial t} + \frac{\partial \overline{u_j \epsilon}}{\partial x_j} = \frac{\partial}{\partial x_j} \left( \left( \nu + \frac{\nu_t}{\sigma_\kappa} \right) \frac{\partial \epsilon}{\partial x_j} \right) + C_1 \frac{P \epsilon}{\kappa} - C_2 \frac{\epsilon^2}{\kappa} \quad (3.10)$$

Equation 3.11 below represents the eddy viscosity variable for the k-  $\epsilon$  model in terms of turbulent kinetic energy and the rate of dissipation of turbulent kinetic energy.

$$\nu_t = C_\mu \frac{\kappa^2}{\epsilon} \quad (3.11)$$

There are five adjustable constants for this model that allow it to be fitted to the application if needed. The standard values for these constants are listed in table 3.1 below.

Table 3.1: List of k-  $\epsilon$  model constants

Constant	Values
$C_\mu$	0.09
$\sigma_\kappa$	1
$\sigma_\epsilon$	1.3
$C_1$	1.44
$C_2$	1.92

### 3.1.5 Q-criterion

The concept of vorticity in fluid dynamics is understood to a certain extent; however, being able to identify these areas in a complex 3D flowfield is much less evident. Identifying coherent vortices in a flow and how they interact with the simulated body is critical in understanding the flowfield. Due to the complex nature and uniqueness of each CFD simulation, there is no single agreed-upon way to identify and visualize these coherent structures. The most common way to identify these vortices is to calculate the vorticity and find the maximum values in the flow field. The Q-criterion is one of the most popular ways beyond the vorticity magnitude. Positive values of the Q-criterion define areas where the vorticity magnitude is larger than the strain rate

or viscous stress. The definition of the Q-criterion starts with the velocity tensor in equation 3.12.

$$\nabla u = \frac{\partial u_i}{\partial x_j} \quad (3.12)$$

Equation 3.12 is decomposed into a symmetric tensor and a skew-symmetric tensor leading to equation 3.13

$$\frac{\partial u_i}{\partial x_j} = \frac{1}{2} \left( \frac{\partial u_i}{\partial x_j} + \frac{\partial u_j}{\partial x_i} \right) + \frac{1}{2} \left( \frac{\partial u_i}{\partial x_j} - \frac{\partial u_j}{\partial x_i} \right) \quad (3.13)$$

where the symmetric tensor in equation 3.14 is denoted as  $S_{ij}$  and is defined as the strain rate tensor. The skew-symmetric tensor in equation 3.15 is denoted as  $\omega_{ij}$  and is defined as the rotation rate tensor. The rotation rate tensor can also be defined as the vorticity tensor.

$$S_{ij} = \frac{1}{2} \left( \frac{\partial u_i}{\partial x_j} + \frac{\partial u_j}{\partial x_i} \right) \quad (3.14)$$

$$\omega_{ij} = \frac{1}{2} \left( \frac{\partial u_i}{\partial x_j} - \frac{\partial u_j}{\partial x_i} \right) \quad (3.15)$$

Referring back to the definition of Newton's law of viscosity in equation 3.16, it can be shown that the viscous stress tensor is only a function of strain rate.

$$\tau_{ij} = \rho\nu \left( \frac{\partial u_i}{\partial x_j} + \frac{\partial u_j}{\partial x_i} \right) \quad (3.16)$$

Given this, the Q-criterion can be defined in equation 3.17 as the second invariant of the velocity gradient tensor. This definition shows that Q will only be positive when the vorticity exceeds the strain rate tensor.

$$Q = \frac{1}{2} \left( \|\omega\|^2 - \|S\|^2 \right) \quad (3.17)$$

### 3.2 Hydrodynamics of Vertical-Axis Darrieus Turbines

The total torque output, torque coefficient, and power coefficient can be used to characterize the performance of a turbine. The total torque is the sum of the pressure and viscous forces multiplied by the distance from the centroid of the airfoil to the turbine axis of rotation [62]. The equation for total torque is defined in equation 3.18 below:

$$\vec{T}(\theta) = (\vec{r} \times \vec{F}_p(\theta)) + (\vec{r} \times \vec{F}_v(\theta)) \quad (3.18)$$

Where  $\vec{T}$  is the total torque vector,  $\vec{F}_p$  is the force due to pressure,  $\vec{F}_v$  is the viscous shear force, and  $\vec{r}$  is the vector that is the distance from the centroid of the airfoil to the center of rotation. The total power available to be extracted by a turbine is equal to the amount of kinetic energy that passes through the swept area of the rotor blades and is given by equation 3.19 below:

$$P_0 = \frac{1}{2} \rho A_{ref} U_\infty^3 \quad (3.19)$$

Where  $\rho$  is the fluid density,  $U_0$  is the freestream velocity.  $A_{ref}$  is the swept area of the turbine and is given by equation 3.20 below:

$$A_{ref} = 2HR \quad (3.20)$$

Where H is the height of the turbine blades and R is the turbine's overall radius from the airfoil's center chord line to the axis of rotation. The actual power extracted from the turbine is based on the torque generated multiplied by the angular velocity and given in equation 3.21 below:

$$P = T\omega \quad (3.21)$$

The instantaneous torque and instantaneous power coefficient can then be calculated using total torque and is given in equations 3.22 and 3.23 below:

$$C_T(\theta) = \frac{T(\theta)}{\frac{1}{2}\rho U_\infty^2 A_{ref} R} \quad (3.22)$$

$$C_P(\theta) = \frac{T(\theta)\omega}{\frac{1}{2}\rho U_\infty^3 A_{ref}} \quad (3.23)$$

Where  $\rho$  is the fluid density,  $U$  is the freestream velocity,  $A_{ref}$  is the swept area, and  $\omega$  is the rotational velocity. The flow field of hydrokinetic Darrieus turbines is quite complex. There is an interaction between shed vortices and blades which is an unsteady phenomenon. The blades have constantly changing angles of attack, adding further complexity to the hydrodynamics. Figure 3.1 below shows the resultant velocity vector at different azimuthal angles  $\theta$ .  $U_\infty$  represents the free stream velocity of the flow field. The tangential velocity of the blade is given by:

$$V_\theta = \omega R \quad (3.24)$$

Where  $R$  is the overall radius of the turbine and  $\omega$  is the angular velocity of the blade. Given these two velocities, a resultant velocity vector can be calculated at any azimuthal angle and is given by equation 3.25 below.

$$V_R = \sqrt{(U_\infty + V_\theta \cos\theta)^2 + (V_\theta \sin\theta)^2} \quad (3.25)$$

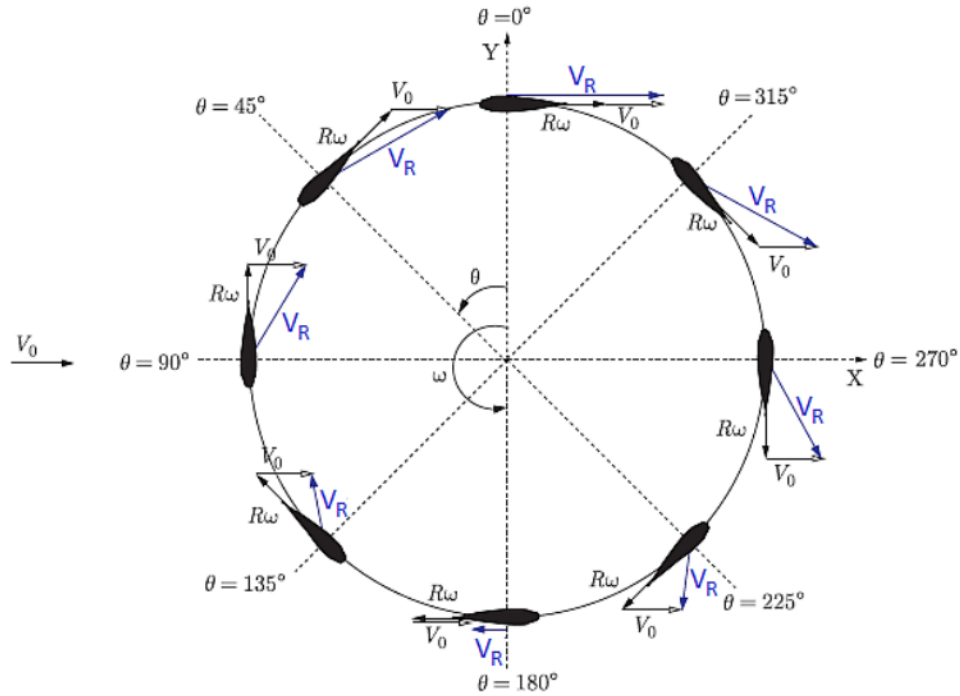


Figure 3.1: Diagram of velocity vectors and azimuthal position on a Darrieus turbine. Obtained from the work of Hall [63]

The ratio of the tangential velocity,  $V_\theta$ , to the freestream velocity is referred to as the turbine's tip speed ratio. The tip speed ratio is related to the turbine's efficiency, and the optimal value is based on the blade geometry and other factors. The formula for the tip speed ratio is given in equation 3.26 below.

$$\lambda = \frac{\omega R}{U_\infty} \quad (3.26)$$

The angle between the chord line of the airfoil and the resultant velocity vector  $V_R$  is called the angle of attack  $\alpha$  and is presented below in figure 3.27. The angle of attack varies over a single rotation and is shown for a few tip speed ratios in figure 3.2

$$\alpha = \tan^{-1} \left( \frac{\sin(\theta)}{\cos(\theta) + \lambda} \right) \quad (3.27)$$

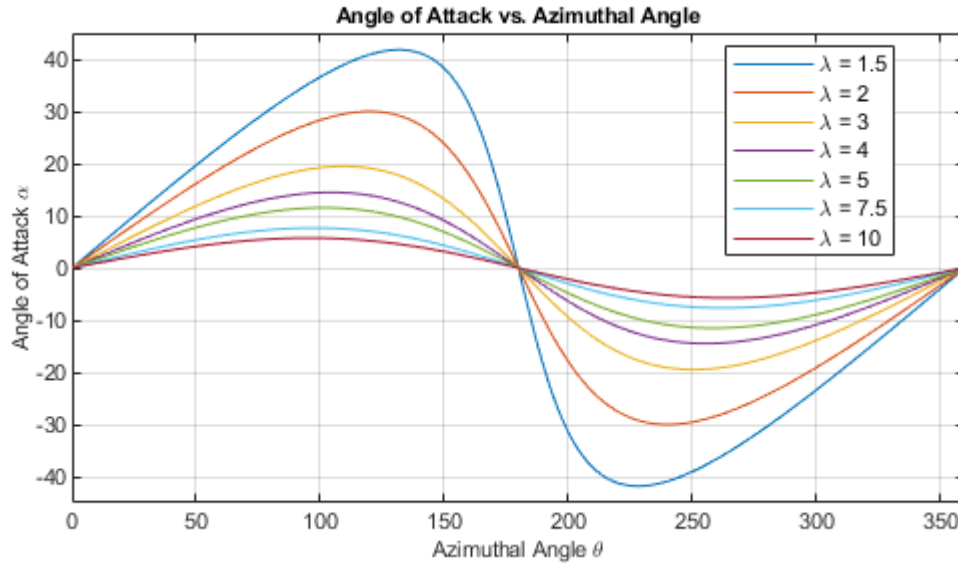


Figure 3.2: Angle of attack vs. azimuthal angle.

Hydrokinetic Darrieus turbines can be further characterized by their Reynolds number. The Reynolds number is the ratio of the inertial forces to viscous forces. Reynolds number is used to determine if the flow is laminar and the viscous forces are dominant or turbulent, where the inertial forces are dominant. Two different Reynolds numbers can characterize a turbine system. The first uses the freestream velocity of the flow, and the other uses the resultant velocity vector. The two Reynolds numbers are given in equations 3.28 and 3.29 below where  $c$  is the chord length,  $\mu$  is the dynamic viscosity, and  $\rho$  is the fluid density.

$$Re_0 = \frac{\rho U_\infty c}{\mu} \quad (3.28)$$

$$Re_{rel} = \frac{\rho V_{RC}}{\mu} \quad (3.29)$$

The freestream Reynolds number works for classifying the flow when the turbine is being simulated at a steady state. When the turbine is in rotation, the relative velocity of the turbine is better at characterizing the flow.

### 3.3 Turbine Parameters

A straight H-Darrieus turbine with a 3-blade configuration was utilized for this study. The 3-blade design is the most common model used in vertical-axis turbines. The H-Darrieus design was chosen due to a few factors. Most of the research on vertical-axis hydrokinetic turbines has shown that Darrieus turbines effectively produce power. Wind-powered Darrieus turbines spin at much higher rotational velocities, generating significant stresses at connection points, which can lead to material fatigue and, eventually, failure. Due to the higher density of water and lower rotational speeds, this is less of an issue in hydrodynamic turbine systems. Table 3.2 below shows the specific turbine parameters used in both experimental and computational studies.

Table 3.2: Prototype turbine parameters

Parameter	Symbol	Value
Freestream Velocity	$U_\infty$	1 <i>m/s</i>
Chord Length	$c$	1.3 <i>in</i>
Turbine Radius	R	8.5 <i>in</i>
Turbine Height	H	10 <i>in</i>
Blade Profile	-	NACA 0018
Number of Blades	N	3
Tip Speed Ratio	$\lambda$	2

### 3.4 Particle Image Velocimetry Theory

Particle image velocimetry is an optical method of obtaining instantaneous information on the magnitude and direction of the velocity in a flow field. The fluid is injected with seeding particles which are assumed small enough to follow the movement of the flow without interference. The flow is then illuminated with a light source to allow optical sensors to capture the particles. The velocity in the flow is then calculated based on the displacement of the particles over a known time. A typical PIV setup is given in figure 3.3. It consists of a study segment, laser source, laser sheet, and camera.

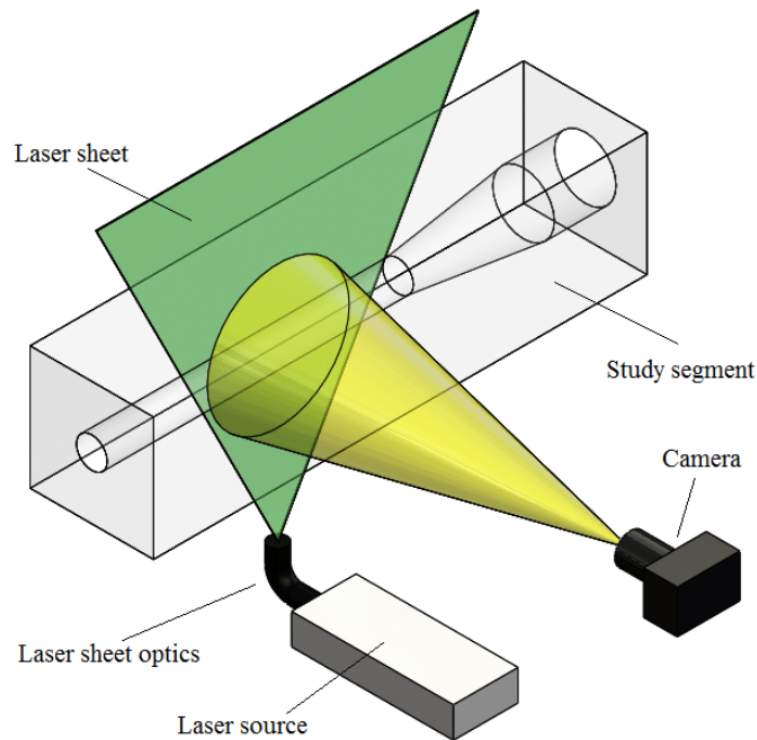


Figure 3.3: General particle image velocimetry experimental setup. Obtained from the work of Murgan et al. [64]

A laser is typically used for PIV experiments because it produces a high-powered light beam. A laser sheet is used to produce a 2-dimensional plane. This laser sheet is achieved by using multiple lenses on a laser. A cylindrical lens is used to bend the

laser beam into a plane, and then a spherical lens is used to compress the plane into a thin sheet. The seeding particles used are one of the determining factors in the accuracy of the PIV measurement. The particles should be small enough to follow the actual path of the fluid while being large enough to reflect enough of the light source to be visible to the camera. The typical particles used depends on the fluid being used for the experiment. The most common type of particles is spherical such as hollow glass beads. Oil droplets are used when the fluid is a gas, not a liquid.

After the experiment and the desired number of images are captured of the flow, they are compiled and post-processed. Pairs of images are analyzed to track the movement of particles over time to generate a velocity field. The image pairs are split into small windows called interrogation areas. Figure 3.4 below shows an example interrogation area along with the particles it contains and how they are tracked over time. Using signal processing techniques, a displacement vector is calculated per interrogation area between the two frames. The velocity is derived from this displacement vector and the time between frames.

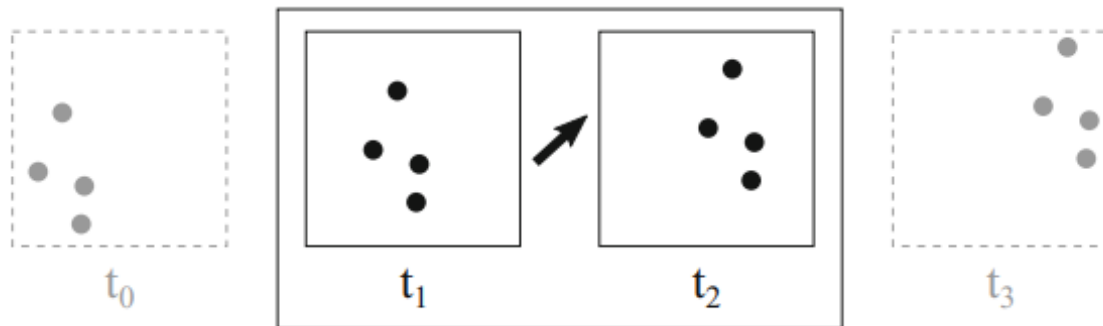


Figure 3.4: Position of particles in two frames in consecutive time steps during PIV. Obtained from the work of Raffel et al. [65]

An example of a particle image velocimetry experiment is shown to give clarity on how the complete PIV process works. Figure 3.5 below shows an image of what a PIV camera would capture before post-processing. The object of interest, in this case, is a wedge shape. The tracer particles show up as white dots on a black background.

Figure 3.6 shows the same image after post-processing. Velocity vectors are shown as the arrows in the image with a scalar scene of vorticity overlapped.

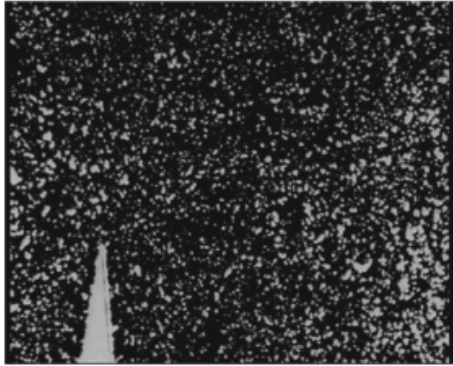


Figure 3.5: Raw PIV image of flow over a wedge. Obtained from the work of Raffel et al. [65]

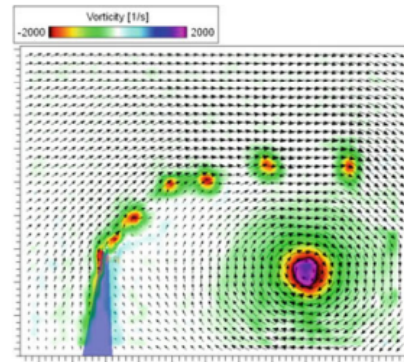


Figure 3.6: Post-processed image of flow over a wedge with velocity vectors and vorticity contours. Obtained from the work of Raffel et al.[65]

The main advantage of particle image velocimetry is that it is non-intrusive. The flow can be analyzed without adding any measurement sensors. This freedom allows the true nature of the flow to be measured without distortion. PIV is necessary when studying flow where any distributions upstream will cause distortions, such as the near-wall region in a laminar boundary layer.

If the tracer particles are chosen incorrectly, there is the possibility that a differential in density will occur between the particles and the fluid. This difference can cause the particles not to follow the fluid directly and may lead to inaccurate results. The other drawback of a standard PIV system is that it only captures a two-dimensional plane in the flow. There can be significant magnitudes of flow in the third dimension, such as vortices, and are missed when looking at a strictly two-dimensional plane. There are more sophisticated PIV systems that incorporate multiple cameras synced together to have the capacity to capture all three dimensions.

## CHAPTER 4: METHODOLOGY

### 4.1 Prototype Design

A scaled prototype of the proposed turbine system was designed and built for experimental performance output and flow pattern evaluation. The computer aided design software (CAD) Solidworks (2020) was used to design the DD-VADHT prototype. Particle image velocimetry (PIV) experimentation was conducted on the model to understand hydrodynamic performance and validate the 2D and 3D computational fluid dynamic simulations. These studies were conducted at the University of North Carolina at Charlotte's water channel. The dimensions of the entire test section of the water channel are 1 meter wide, 1 meter tall, and 9 meters long. The value of the water channel used in this experiment was the large test section allowed for a larger prototype to be deployed (1:2) than is typically used in PIV experimentation. The setup and procedures used in the PIV studies and the results obtained are given in the following chapters. The proposed design consists of two separate turbine systems that operate in counter-rotation. Each turbine system consists of two Darrieus rotors that are in parallel and rotate in opposite directions. One rotor will drive an armature coil, and the other will drive a permanent magnet generator. This system is designed without a gearbox between the rotor shaft and generator, creating a direct-drive system. Figure 4.1 below presents a CAD image of the proposed prototype design. Figure 4.2 presents an image of the finished DD-VADHT prototype. The prototype design can be split into three main subassemblies. These subassemblies are the frame, turbine, and generators. The design aspects as well as the methods of manufacturing are discussed in further detail in the following sections.

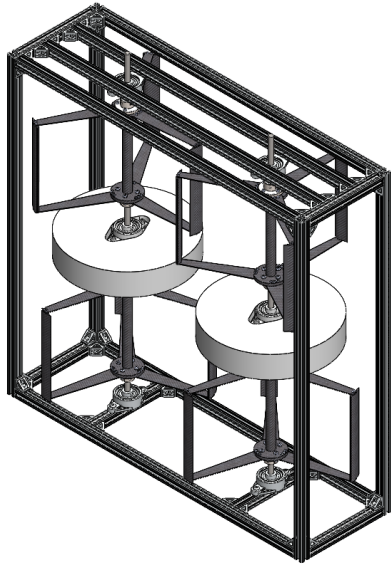


Figure 4.1: CAD model of prototype turbine system

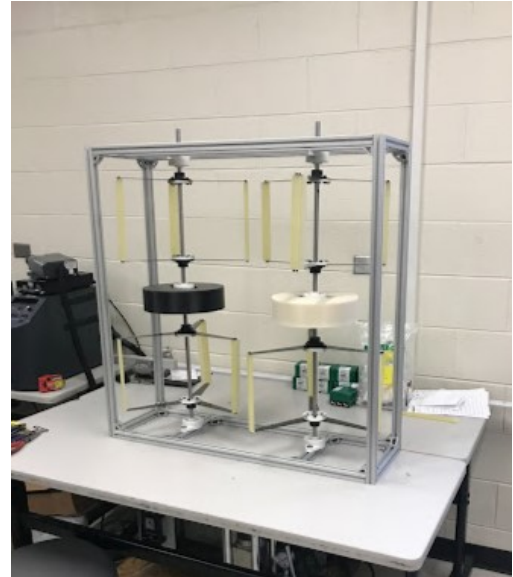


Figure 4.2: Physical model of prototype turbine system

#### 4.1.1 Prototype Frame Subassembly

The first design constraint considered was the overall size of the scaled turbine. The design needed to fit inside the UNCC water channel test section. The UNCC water channel, as previously stated, had an overall cross-sectional area of 1 meter by 1 meter, so the design needed to adhere to those dimensions. During the design process, a trade-off was considered between the overall size of the design and the blockage effect. Due to the nature of the proposed turbine, it consisted of two counter-rotating turbine systems, with each turbine consisting of two turbines in parallel. This unique requirement created a design that used the swept of four turbines; therefore, the size of the overall system needed to be larger to accommodate these four turbines.

The first part that was designed was the frame assembly that would be used to secure the turbines in the water channel. The frame material used consisted of silver anodized aluminum T-slotted framing rails. Open gusset brackets were used to connect all t-slotted rails. There were a couple of main benefits to using the T-slot railing over other framing options. The first was that the anodized aluminum had corrosion

resistance and would survive being submerged in the water channel for periods. The second reason was that the T-slots allowed for design flexibility. This flexibility allows for additions without requiring the entire prototype to be redesigned. Cross rails were added to the top and bottom, allowing the corrosion-resistant bearings to be secured. These bearings were used to allow the motion of the turbine rotors. The CAD model of the proposed prototype design is given in figure 4.3. Figure 4.4 gives an image of the physical prototype.

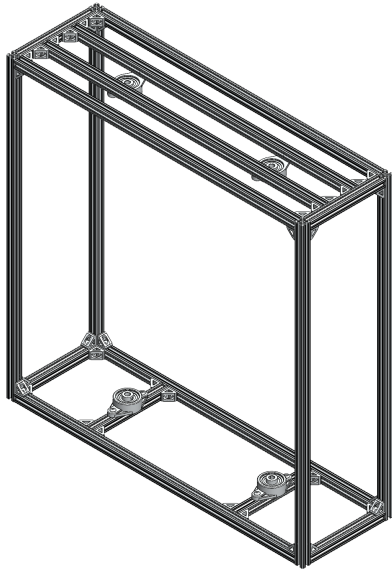


Figure 4.3: CAD model of frame sub-assembly of prototype system



Figure 4.4: Physical frame subassembly

#### 4.1.2 Turbine Rotor Subassembly

The turbine rotor assembly was the next subassembly that was designed. The turbine system had a unique constraint: the top and bottom rotors had to rotate in opposite directions. Each turbine needed to have independent rotation and therefore have a separate shaft. This requirement was only for the DD-VADHT prototype model since there is only a surrogate for the generator. An operational turbine system will include a permanent magnet generator. Each turbine's rotor was connected to corrosion-resistant ball bearings on each side to achieve independent rotation. One

ball bearing was secured to the frame assembly, while the other was secured to the surrogate generator assembly. This design allowed for the rotor on the top and bottom to spin in opposite directions. The overall design of each turbine rotor is given in figure 4.5.



Figure 4.5: CAD model of turbine subassembly of prototype system

#### 4.1.2.1 Airfoil Blades

The airfoil blade profile that was used for each rotor was NACA 0018. Additive manufacturing (3D printing) was the best way to produce all of the blades. This is due to the required ease of use and time scale. The turbine blades were produced with a ProJet 3500 HDmax Printer. The CAD model of the blade is presented in figure 4.6. An image of the printed rotor blades is given in figure 4.7 below. Using additive manufacturing presented the unique challenge of securing the blades to the carbon fiber supports. Brass screw-to-expand inserts were used to fix this problem. These were inserted into the printed parts and expanded when screws were applied, allowing for the airfoils to be connected to the supports. The printer uses UV-curable plastic to manufacture the parts which cause them to be semi-translucent.



Figure 4.6: CAD model of turbine blade with mounting points for carbon fiber supports

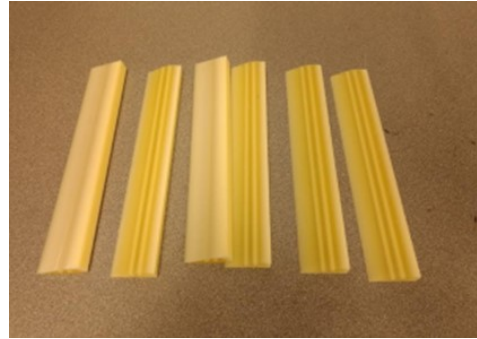


Figure 4.7: 3D printed turbine blades

#### 4.1.2.2 Blade Support Rods

The blades for the turbine are connected to the central hub with support pieces. Energy is transferred from the flow of water to the turbine blades and then through the support pieces into the drive shaft. This generates a large amount of force through the supports and, therefore, the material needed to have high strength without having too much flow disruption. The support rods were created with carbon fiber to achieve the strength requirement. Each piece was cut out of a carbon fiber sheet using a Wazer waterjet machine. Figure 4.8 below gives a CAD model of the support piece. Each support utilized two mounting points on the side connecting to the airfoil and three mounting points to the central hub.



Figure 4.8: Carbon fiber support CAD model for turbine blades

The drive shaft for each turbine rotor is connected to two ball bearings on each side. Each rotor used one drive shaft and went through the entire turbine subassembly. Easy-access flange-mounted shaft supports were used to connect the rotor to the drive

shaft. Two shaft supports were used on each rotor and were attached to the central hub. The shaft supports used a clamp mechanism to hold the shaft in place and, with the connection to the central hub, allowed the turbine to rotate as a single part. The CAD model of the shaft support with fasteners is given in figure 4.9 below. The flange-mounted shaft support is connected to the central hub with four fasteners. The clamp mechanism on the shaft support contains two fasteners used to constrain the rotation of the drive shaft. Figure 4.10 below shows images of the physical support rods connected to the central hub and the flange-mounted shaft supports.

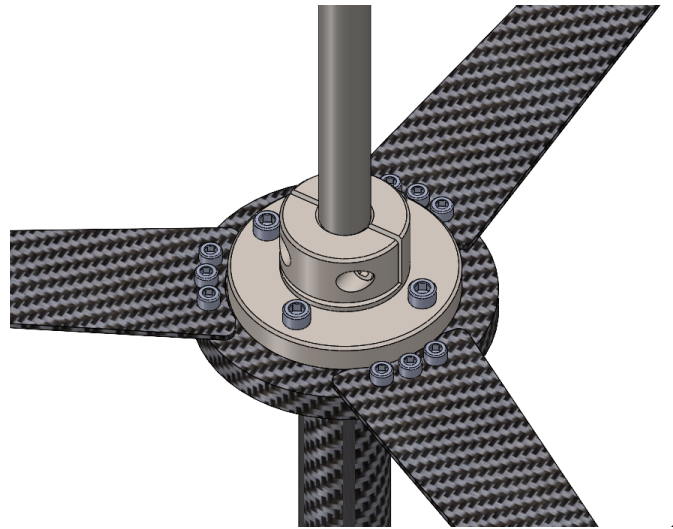


Figure 4.9: Central hub for turbine rotor



Figure 4.10: Physical carbon fiber supports for turbine blades

### 4.1.3 Surrogate Generator Subassembly

The proposed Darrieus turbine system utilized an axial-flux permanent magnet generator due to the spinning of the counter-rotating top and bottom rotors in opposite directions. As stated in this thesis, the generator's design was not included in the scope of work. Due to the generator's blunt geometry and flow disruption, it was included in the model. In place of a generator, a surrogate generator was designed. This surrogate generator served two purposes. The first, as already stated, was to account for the flow disruption on the turbines from the generator geometry. The second was the surrogate generator was utilized as a mounting point for the bearings to allow independent rotation of the top and bottom turbine rotors. The turbines were constructed using additive manufacturing. The machine that was used was a ProJet 3500 HDmax Printer. Additive manufacturing was used because it allowed the bearing to be set inside the surrogate generator. An image of the CAD model of the generator is given in figure 4.11 below. The bearing is shown mounted into the generator subassembly in this image. A physical image of the surrogate generator without the bearings is given in figure 4.12 below. The contour of the bearing casing is shown along with the mounting points. Brass screw-to-expand inserts were used to mount the bearings to the generators.

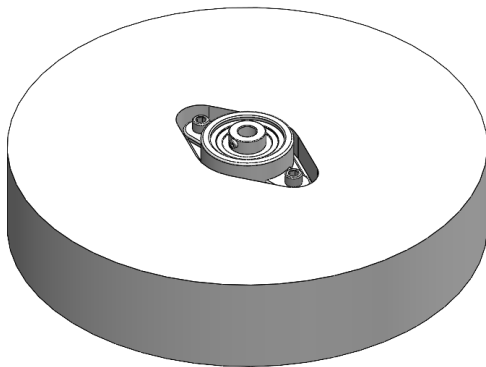


Figure 4.11: Surrogate generator sub-assembly of prototype system



Figure 4.12: Physical 3D printed surrogate generator subassembly of prototype system

## 4.2 Numerical Simulation Setup

This chapter describes the setup of the computational fluid dynamic (CFD) simulations. This setup includes the simplified CAD input geometry, mesh setup, computational domain, and physics models used in the 3D CFD simulations. The commercial CFD code STAR-CCM+ v15.04 is used to generate the mesh and run the simulations. The general discretization scheme used by STAR-CCM+ is the finite volume method. The density definition in all simulations is incompressible flow. A second-order upwind discretization scheme calculates the face values of the convection and diffusion terms. Euler implicit scheme, a first-order temporal scheme, approximates the transient term. Roe FDS is used for the calculation of the coupled inviscid flux. A rigid body motion model is used to simulate the movement of the two turbines. Since there is a prescribed constant rotation rate, the entire rotating subdomain mesh is rotated, and the main computational domain is stationary. The rotation of the transient simulation required a coupled flow solver over a segregated flow solver. The coupled flow model solves the continuity and momentum equations simultaneously as a vector of equations. The strength of the coupled solver is that it works well when there is a dominant source term, such as rotation or heat flux. The other advantage of using the coupled flow solver is that the CPU solver time scales linearly with the mesh size. The rate at which the solver converges does not decay with the refinement of the mesh. Weiss-Smith method is used for the preconditioning treatment. An unsteady implicit model is selected as the time-integrating approach to identify the turbine's wake and show how the blades' vortices affect others during rotation. A coupled flow solver utilizes two pseudo-time-marching approaches: explicit and implicit. The time scale of the studied unsteadiness determines the choice between the two. The explicit unsteady approach works best when the order of the time scales is of the acoustic processes, such as shock front tracking. This makes the explicit time-marching approach not suitable for this study. The implicit unsteady approach works best when the time

scales of the unsteadiness are in the same order as either the convection or diffusion process. This approach is more suitable for this application. In the implicit unsteady approach, a time step is chosen, and for each physical time step, inner iterations are carried out to converge the solution at that specific instant in time.

#### 4.2.1 CFD Turbine Geometry

Generating an input geometry for a CFD simulation is one of the most time-consuming steps and is typically the bottleneck in the simulation pipeline. CAD models used in the design process have many intricate features that cause problems for simulation software, including gaps, surface interference, fasteners, and unnecessary tiny features. Due to limits on computational resources, these features need to be removed so that the most simplified version of the geometry that still accurately models the flow can be analyzed. All of the fasteners and hardware from the PIV prototype model for this simulation were removed. These features were considered to have negligible effects on the hydrodynamic performance of the turbine.

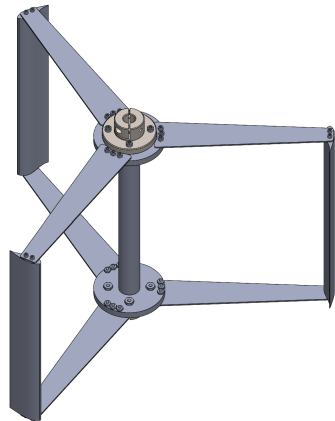


Figure 4.13: CAD model of prototype turbine system used for PIV experimentation

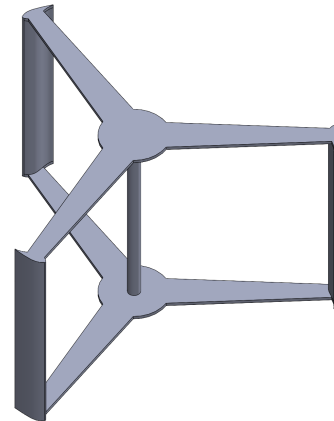


Figure 4.14: Simplified CAD model of turbine system used for CFD simulation

Figure 4.13 below represents the CAD model of the prototype turbine used in the PIV experimentation. This model includes hardware used to secure the blades to the central hub. This model also includes all the fasteners connecting the turbine airfoil

blades to the connecting rods. These features were removed to take the prototype geometry and simplify it for the numerical simulations. The simplified geometry is shown in figure 4.13 below.

The simplifications were minimal to keep the geometry as close as possible to the prototype geometry. The turbine blades and the supports connecting to the center hub were merged to create a single manifold part. This merge was done to remove the small surface edges on the support pieces and simplify the meshing. Figures 4.15 and 4.16 below show a close view of where the blade and the support connect for the PIV prototype model and CFD model. The difference in geometry between these two models can be observed as minimal.

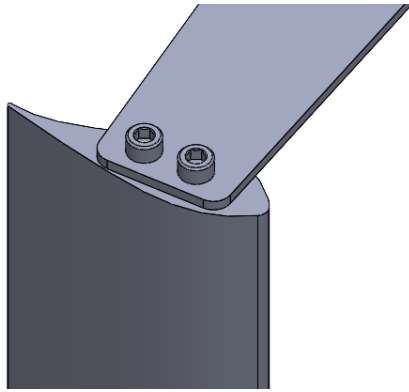


Figure 4.15: Close-up image of the connection between the blades and supports in PIV prototype

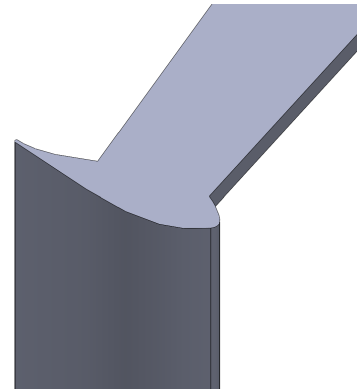


Figure 4.16: Close-up image of simplified geometry between blades and supports in CFD model

The full 3D CFD model was generated to include two counter-rotating turbines. Only one set of turbines is modeled in this simulation to reduce computational cost. The turbine system on the top can be considered to have the same overall hydrodynamic performance as the bottom, and therefore only one set of counter-rotating turbines is analyzed. Figure 4.17 below gives an isometric view of the complete turbine system.

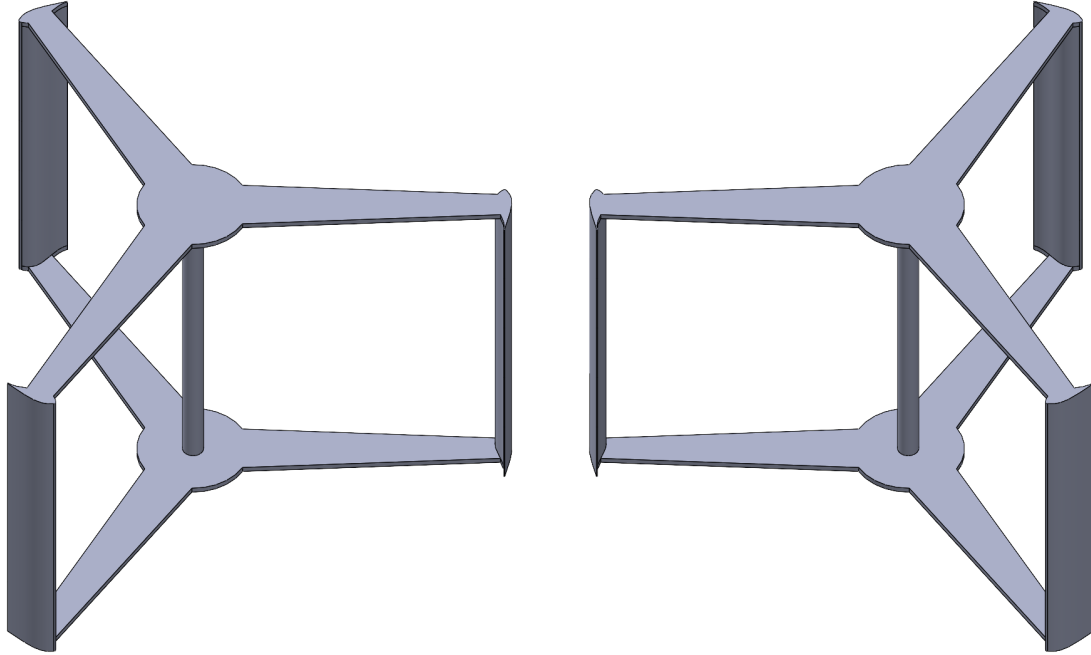


Figure 4.17: Isometric view of full 3D CFD turbine system

#### 4.2.2 Computational Domain and Boundary Conditions

Based on previous research on 3D CFD simulations on vertical axis turbines [62], a rectangular test section was generated around the turbine model. The diameter of a single turbine was used to characterize the computational domain. The diameter of a single turbine is  $D = 17in$ . The total length of the domain in the free-stream direction is equal to  $L = 32D$ . The turbine system is set  $8D$  behind the velocity inlet and  $24D$  in front of the pressure outlet. The total width of the domain is equal to  $12D$ . The velocity inlet was set to a value of 1 m/s, and a pressure outlet was set on the opposite side. Symmetry boundaries were applied to the top, bottom, and sides which were used as planar slip walls with the shear stress equal to zero. The computational domain is broken up into two domains: fixed and rotating. A diagram of the main computational with the dimensions is given in figure 4.18 below.

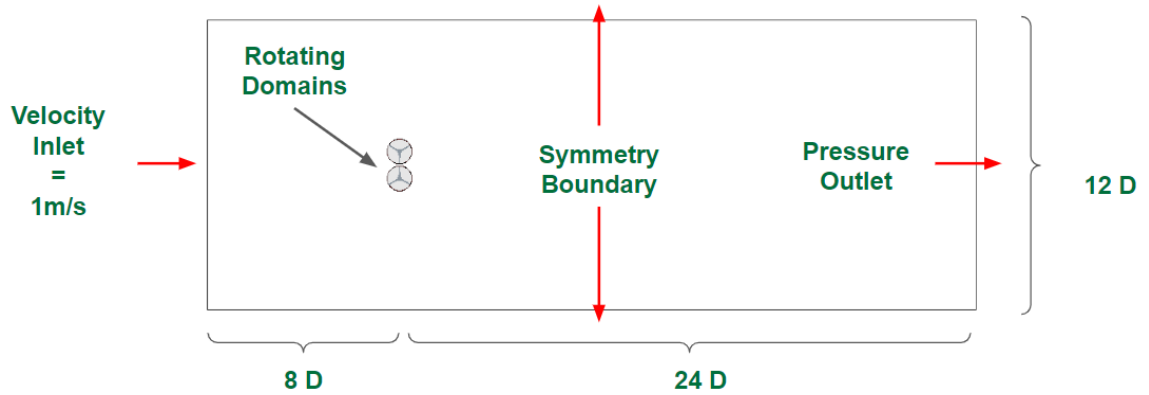


Figure 4.18: Fixed computational domain dimensions

The rotating domain is the prescribed motion region relative to the fixed main computational domain. Figure 4.19 shows the two rotating computational domains used along with the airfoil blades and the center shaft. There is an internal interface wall between the fixed and rotating computational domains that allow for mass transfer.

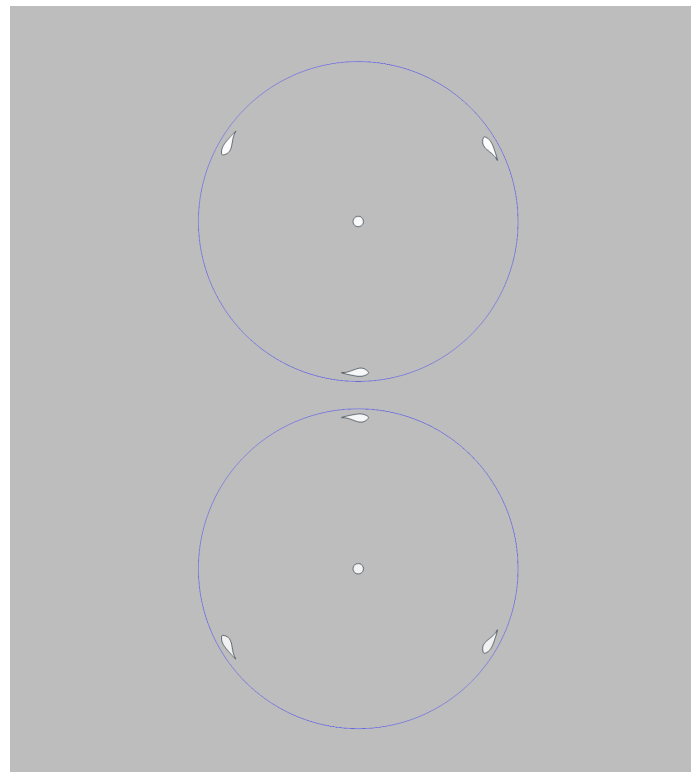


Figure 4.19: Rotating computational domains

### 4.2.3 3D Mesh Generation

Mesh generation discretizes a continuous geometrical domain into a set of discrete cells. The governing equations of fluid flow described earlier in this thesis are solved in each of these discrete cells. The accuracy of the numerical simulation is based on the quality of the mesh. Given the desire for a transient study and a reasonable simulation running time, a trimmed cell mesh was selected for the three-dimensional study. Prism layer cells were generated around the near wall region to capture the flow in the boundary layer accurately. The flow around the turbine blades was specifically of interest due to most of the forces generated in this area. The blades required a fine surface mesh in this area. The surface mesh for a single turbine rotor is given in figure 4.20.

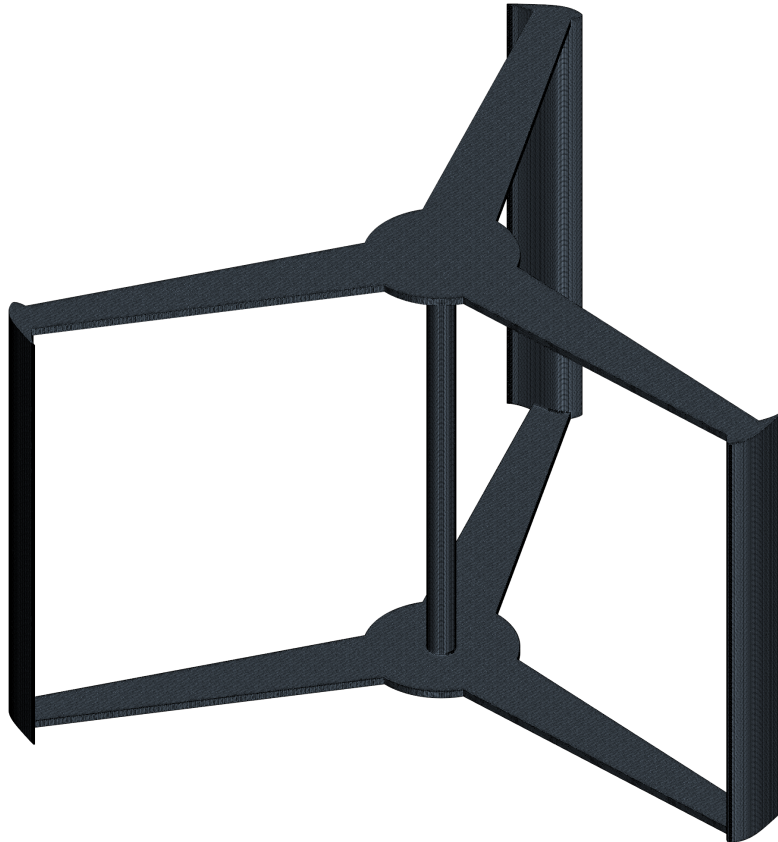


Figure 4.20: Isometric view of surface mesh over single turbine system

#### 4.2.3.1 Blade Mesh Refinement

The geometry of the turbine blades required a more refined mesh than the rest of the rotor. The flow structures around these blades are complex, and having a high-quality mesh in this area is essential in understanding the performance output of the turbine in terms of lift generated and, therefore, torque generation. Custom controls were applied to achieve a higher-density surface mesh on the blades. A standard target surface size of 0.35 inches was used for all of the surfaces on the turbine rotor. A custom target surface size of 0.028 inches was selected to have a finer surface size for the blades. The airfoil's trailing edge includes a small radius, and therefore the minimum surface size needed to be reduced for the blades. A minimum surface size of 0.0035 inches was used to allow the mesh to capture the trailing edge accurately. To ensure the wake generated from the blades was captured, there needed to be a smooth transition from the blade's surface to the core mesh. This transition was adjusted by implementing a custom volumetric growth rate. A volumetric growth rate specifies the speed the cells transition from the surface to the outer core mesh. A slow growth rate was implemented, which gives four equal-sized cell layers per transition. A total of 6 prism layers were used with a total prism layer thickness of 0.021 inches. A prism layer stretching factor defined the thickness of each cell as a ratio of the previous layers. A prism layer stretching factor of 1.5 was used for this study. The surface mesh for the airfoil blade, along with the connecting rod, is given in figure 4.22 below. There is an increase in the number of cells near the leading and trailing edge of the airfoil along with a high density of cells on the surface of the blade.

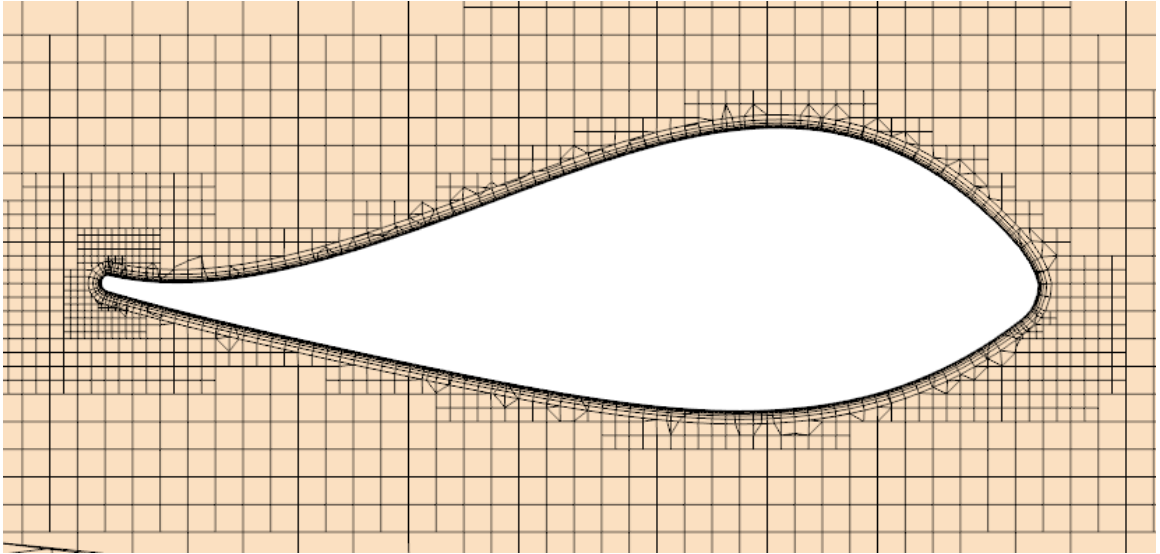


Figure 4.21: Cross-section view of mesh around turbine blades on  $xy$ -plane

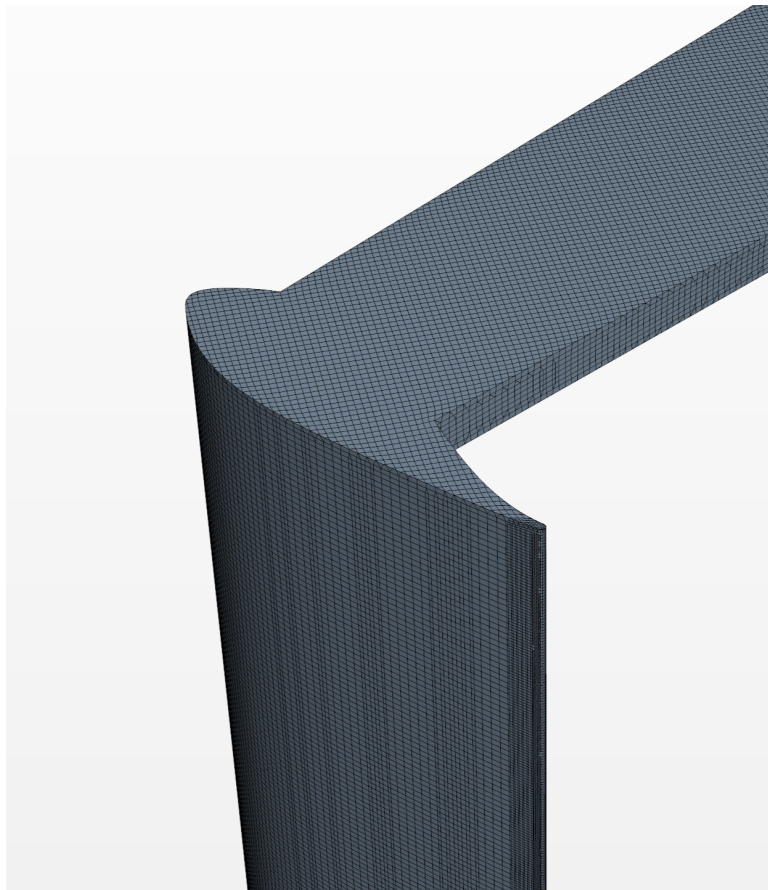


Figure 4.22: Isometric view of surface mesh on turbine blades

### 4.2.3.2 Rotating Domain Mesh

The exact value of 0.1 inches for the volumetric isotropic trimmer was used in the rotating domain. This allows a smooth blend between the rotating and main computational domains. Figure 4.24 below shows the mesh as the cross section at the mid-plane of the turbine for the rotating domain. There is a constant cell size as the mesh transitions from the rotating to the main computational domains. A single mesh was used for both the steady and transient cases; therefore, there needed to be a constant transition between the two domains. Due to the transient case, the mesh inside the rotating domain needed to be much finer. The mesh must capture the flow behind each blade for all azimuth angles. With a moving reference frame transient simulation, the only way to achieve this was to have a fine volumetric mesh inside the rotating domain. An image of the two turbine rotors in counter-rotation, along with the rotating subdomains and the close wake refinement, is given in figure 4.23 below. The cross-section view of the mesh at the middle plane of the turbine is given in this figure.

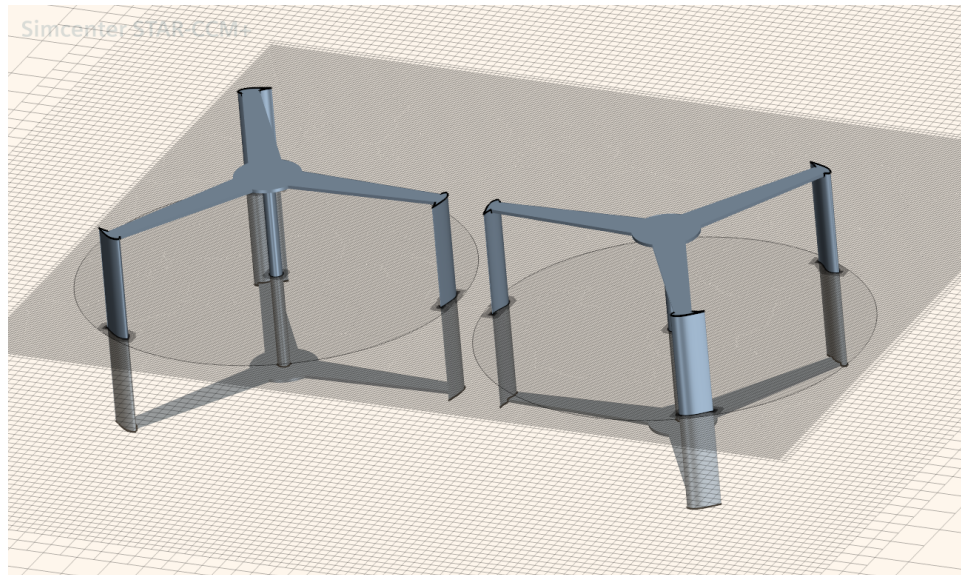


Figure 4.23: Isometric view of full turbine system with a cross-section of mesh on  $xy$ -plane

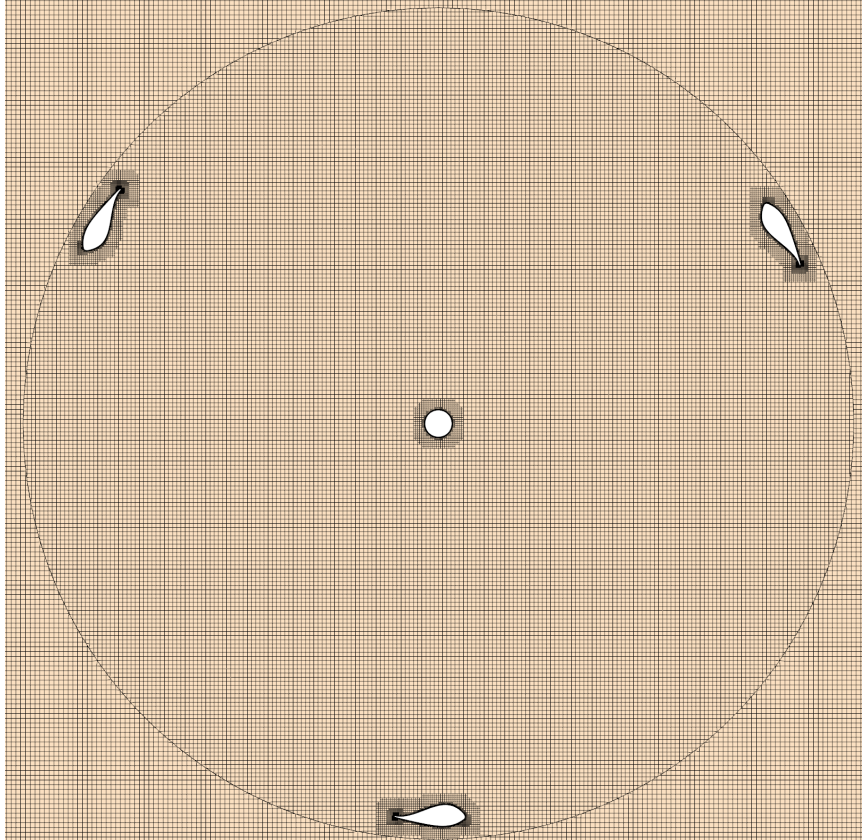


Figure 4.24: Cross-section view of rotating domain on  $xy$ -plane

#### 4.2.3.3 Wake Refinement

The wake region was an area of interest in this study to understand the vortices. As the turbine rotates, the blades encounter the wake of previous blades, disrupting the lift and torque produced by the blade. There were multiple volumetric areas with an isotropic refinement of the cells to have a finer mesh. This study used two wake refinement zones, referred to in this thesis as close and far volumetric refinements. The close wake refinement is shown in figure 4.25. A custom isotropic trimmer size was used with a cell size of 0.1 inches in this area.

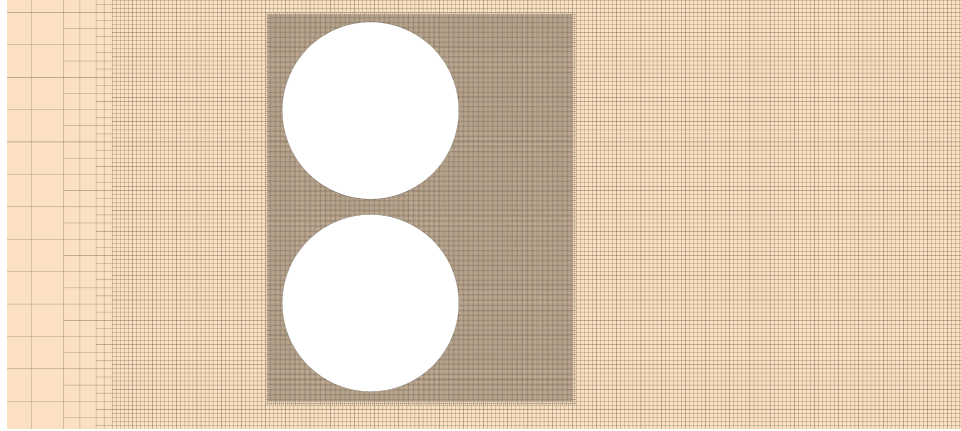


Figure 4.25: Cross-section view of close volumetric wake refinement on  $xy$ -plane

The far wake region used a coarser volumetric isotropic trimmer size. For the transient case, there was a desire to understand the wake downstream of the turbine; therefore, the far wake region was generated. The mesh in this volume did not need to be resolved to the same level as the close wake region. This far wake region used a custom isotropic trimmer value of 0.5 inches. Figure 4.26 below shows the far and close wake regions. The rotating domains where the turbine rotors are located were removed for clarity. The outer region in this figure shows the mesh outside of the far wake volumetric refinement. The mesh in this area is coarse due to computational resources and flow outside the area of interest.

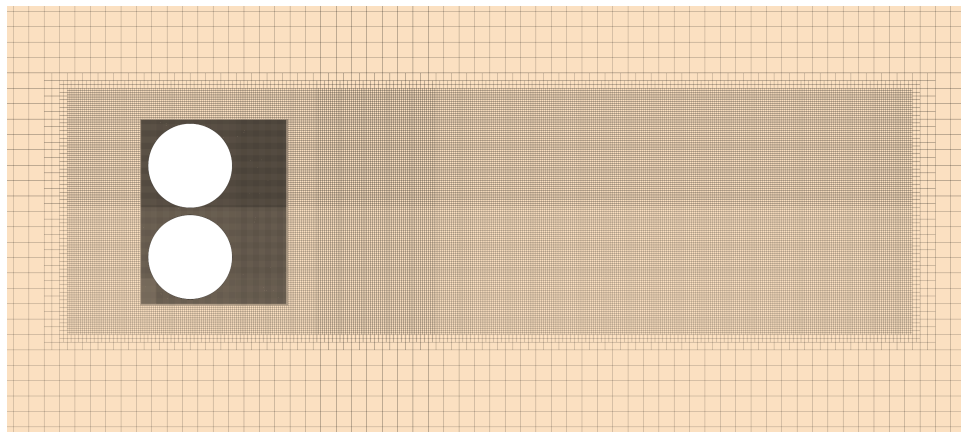


Figure 4.26: Cross-section view of far volumetric wake refinement on  $xy$ -plane

4.2.3.4 Wall  $y^+$ 

The wall  $y^+$  value was calculated over the entire surface of the rotor to ensure that the mesh generated was suitable and that the boundary layer was resolved. The prism layer of cells next to the walls was selected so that the value of the wall  $y^+$  was less than 5. The wall  $y^+$  value is a non-dimensional wall distance and is defined in equation 4.1 below where  $u_\tau$  is the friction velocity,  $y$  is the distance to the surface, and  $\nu$  is the kinematic viscosity. The friction velocity can be defined as given in equation 4.2 below with  $\tau_w$  as the shear stress on the wall and  $\rho$  as the fluid density

$$y^+ = \frac{u_\tau y}{\nu} \quad (4.1)$$

$$u_\tau = \sqrt{\frac{\tau_w}{\rho}} \quad (4.2)$$

Figure 4.27 below shows the scalar scene with the wall  $y^+$  value over the rotor blade. The maximum wall  $y^+$  values are on the edges of the airfoil blades, and therefore those areas had mesh refinement.

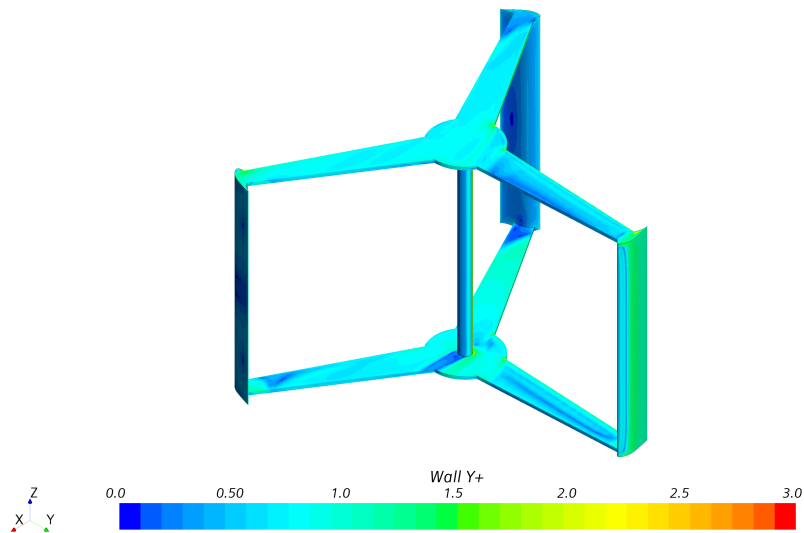


Figure 4.27: Isometric view of wall  $y^+$  over single turbine system

#### 4.2.4 2D Mesh Generation

The 2D mesh was constructed with the same size computational domain as the 3D mesh, ensuring as slight variation as possible between 2D and 3D simulations. The 2D simulation is a cross-section of the 3D model at the mid-plane of the blade. The same overall physics models, as well as boundary conditions, were used in the 2D simulations. A velocity inlet was used as the flow driver, and a pressure outlet was used on the other side of the computational domain. Symmetry planes were used as the sides of the computational domain as planar slip walls with the shear stress equal to zero. Two rotating domains inside of a stationary domain were used to emulate the rotation of the turbines for the unsteady simulations.

##### 4.2.4.1 Blade Mesh Refinement

Refining the mesh around the blade geometry was the most critical aspect when designing the mesh. The mesh design was centered around a good density over the surface of the airfoil and provided quality mesh around the trailing edge. The mesh around the airfoil for the 2D case is given in figure 4.28. The prism layer meshed was used to capture the boundary layer over the airfoil. Forty prism layers were used with a total thickness of 0.1 *in*. A surface growth rate of 1.1 was used to ensure a smooth transition from the prism layer mesh to the outer mesh. The target surface size was 1 percent of the base size. The minimum surface size was 0.1 percent of the base size. A volumetric control was applied to the rotating domain with a value of 7.5 percent of the base size. This was done to ensure a fine enough mesh inside the rotating domain to capture vortices that could interact with other blades. A surface control was applied to the rotating domain edge, which for a 2D simulation, was reduced to a circle. A custom surface size of 0.05 *in* was applied to this surface to ensure that the cells inside and the outside of the rotating domain are roughly the same size to reduce interpolation error. The prism layers on this surface were disabled on both

sides due to them not being necessary. The size of the cells inside the rotating domain was chosen to be equal to those outside of the rotating domain to reduce any error from the internal interface interpolation.

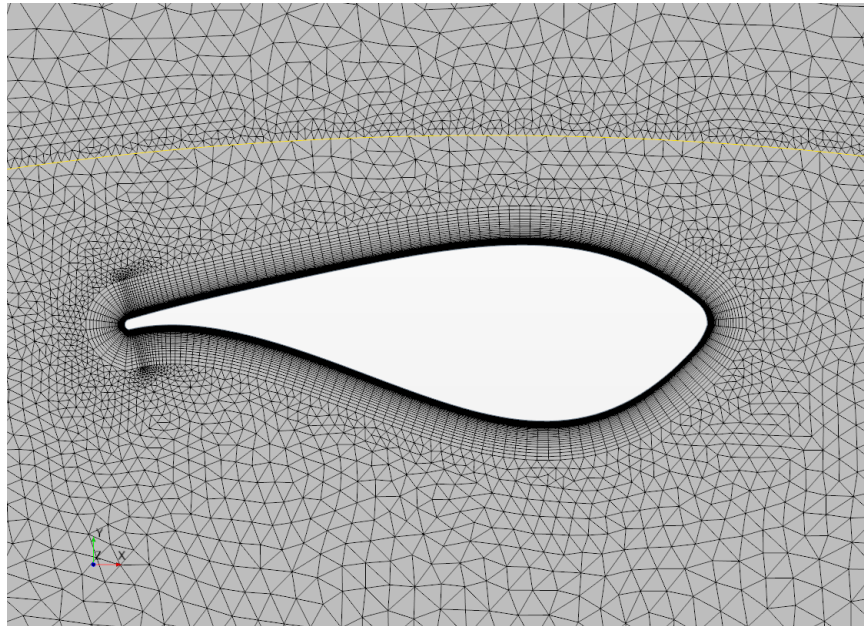


Figure 4.28: Final 2D mesh around blades

The mesh needed to generate wall  $y$ -plus values over the surface of the blades that were less than 1. Since the 2D simulations have a much smaller mesh size, it was computationally possible to use a value of 1 over a value of 5 used in the 3D simulations. This was done by calculating and setting the first layer height on the surface of the airfoil blade to  $5e-6$  m. Figure 4.29 below shows the wall  $y$ -plus value over the surface of one of the airfoils. The highest wall  $y$ -plus are on the airfoil's trailing edge and have a maximum magnitude of around 0.75. The rest of the surface of the airfoil has a much lower value of  $y$ -plus, which provides evidence that the mesh does an excellent job of resolving the near-wall region. The high wall  $y$ -plus in this area further confirms that the airfoil's trailing edge is essential and needs careful attention on the mesh density.

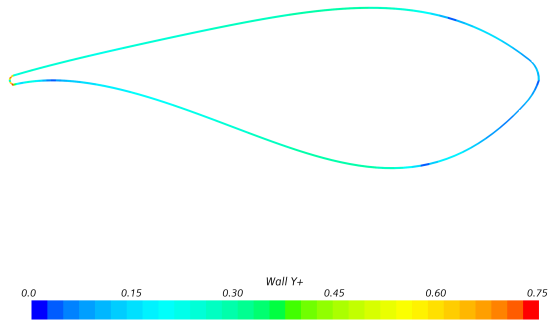


Figure 4.29: Wall  $y$ -plus values over the surface of 2D blades

#### 4.2.4.2 Rotating Domain Mesh

Figure 4.30 below gives an image of the rotating domain for the 2D simulations. Due to the volumetric refinement inside the rotating part, the cell density is much finer than the 3D mesh. The 2D simulations were aimed at understanding the turbine performance in terms of torque and power output. The wake region was not an area of interest in these simulations; therefore, there was no further refinement. This is contrary to the 3D simulations where the wake region was analyzed and compared to the PIV experimentation. In these simulations, the wake region needed further volumetric refinement so that the vortex-blade interactions could be analyzed.

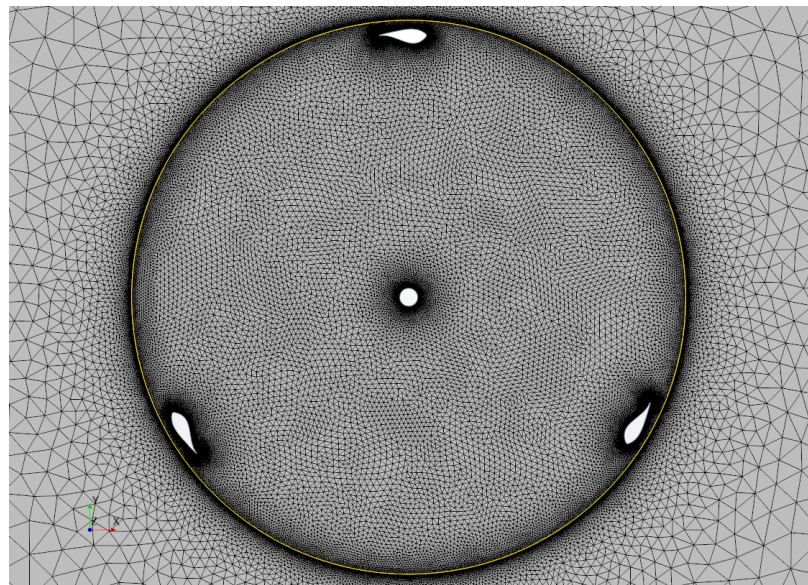


Figure 4.30: Mesh of rotating domain for the 2D CFD simulations

### 4.3 Particle Image Velocimetry Setup

#### 4.3.1 UNCC Water Channel

The particle image velocimetry experiments were conducted at North Carolina's Motorsports and Automotive Research Center on the campus of The University of North Carolina at Charlotte. The facility utilizes an open recirculating water channel design. The advantage of a recirculating design is that once at a steady state, the seeding density is considered constant. In addition, the open-top channel design allows for easy access to the channel to deploy and retrieve models. The UNCC water channel contains a square 1-meter test section 3 meters in length. The channel's maximum flow velocity is  $1 \frac{m}{s}$  allowing for a maximum Reynolds number of a  $10^6$  over a body that has a characteristic length of 1 meter[66]. The channel design consists of a submerged pump that is the driver of the flow. After the pump section, the water travels through a section of PVC pipe, dampening the magnitude of vortices in the flow. The water then travels through two turning vanes to be directed toward the test section. The water travels through another flow straightener to reduce the turbulence and have a more uniform flow field. This flow straightener consists of a honeycomb structure with a diameter of  $6.4mm$  and a length of  $5cm$ . This flow straightener is designed to reduce vortices generated from the turning vanes. The water then flows through a nozzle section, accelerating the flow and decreasing the small vortices created by the honeycomb flow straightener. The water then enters the test section at the desired flow rate. The channel is designed to accommodate many different types of models and therefore does not have a single test section mounting system. Universal mounting rails on the side of the channel walls allow for many models of different sizes and configurations to be deployed. The flow then passes through the test section and travels through two more turning vanes before returning to the pump to start the cycle again. Figure 4.31 below shows the schematic drawing of the design of the UNCC water channel.

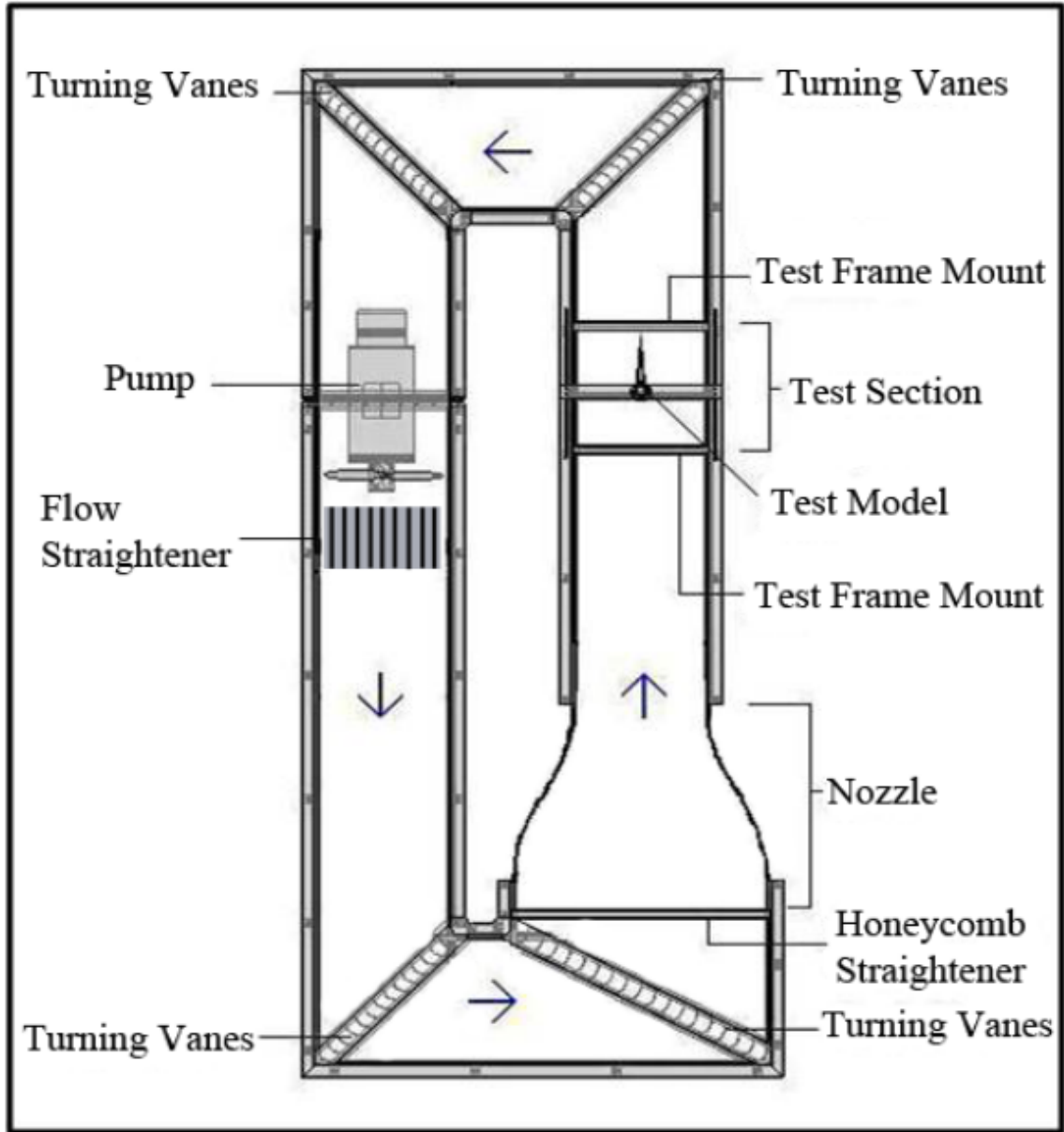


Figure 4.31: Schematic view of UNCC water channel. Obtained from the work of Hellman [66]

### 4.3.2 Prototype Adaptions to Water Channel

Fitting the turbine into the water channel for the PIV experiment required several adaptions to the exterior frame of the prebuilt prototype. The water channel at UNCC was designed to accommodate many different model mounting mechanisms. The channels test section is designed with two main features to deploy models: a universal test frame and slotted tracks with linear bearings. The universal test frame consisted of two grooves  $1m$  apart that ran down one side of the channel wall, across the bottom, and up the other. This allows for frames to be built, models placed and secured inside, and the entire system slid into place. Due to the turbine prototype size, these grooves would not have been feasible. The second feature is the slotted rails on both channel walls that run the entire test section length. These rails are designed to fit linear bearings allowing for further customization. A traverse mechanism has been utilized and is mounted to these rails to hold smaller models in place. The models are mounted to this traverse mechanism, allowing their movement to be precisely controlled inside the water channel. The model with all four turbines was much larger than the capability of the traverse mechanism. Given the size of the turbine system relative to the test section dimensions, the slotted rails with linear bearings that the traverse mechanism utilized was the best option to secure the turbine. The traverse mechanism needed to be removed to free the top of the water channel and allow the entire test section length to be utilized for the turbine PIV experiment.

The frame of the turbine prototype was designed to be adaptable and allow for changes. Mounting the model to the slotted rails required additions to the original prototype frame to be made. The adaptions needed to be designed to allow easy deployment and retrieval of the turbine system in the water channel. The turbine needed to be easily removed to minimize the exposure to the corrosive environment of the water as well as ensure that the turbine would not damage the channel. The adaptions to the prototype consisted of 4 vertical supports constructed from T-slotted

framing at each of the corners of the original turbine frame. Connected to these supports were two horizontal pieces of T-slotted framing that went across the width of the channel. The end of each of these horizontal supports was bracketed with holes that allowed for mounting to linear bearings using threaded-stud knobs. These knobs were used to remove the turbine from the water channel without needing any tools and only required two people to remove them. Figure 4.32 below shows the frame adaptations to accommodate the prototype in the water channel. The image shows the vertical and horizontal supports from a side view.

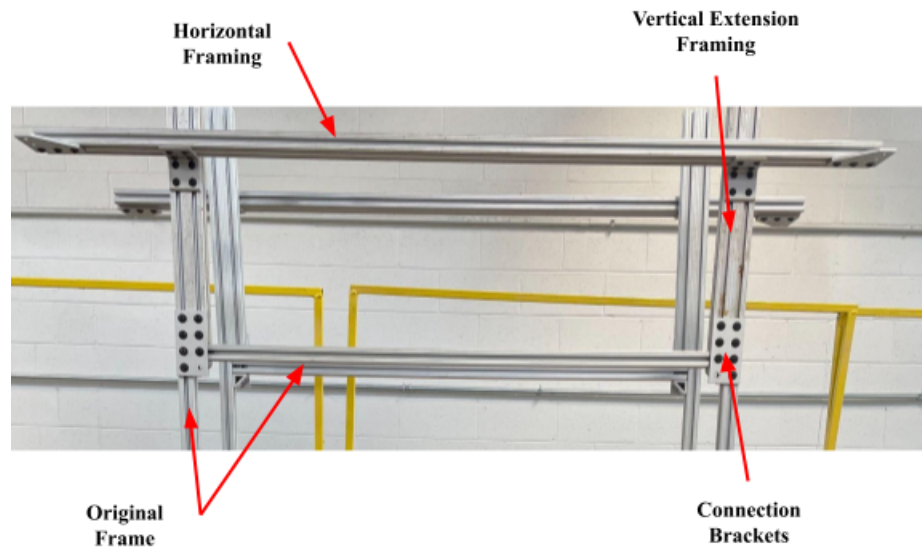


Figure 4.32: Frame adaptations made to original prototype frame

Rectangular brackets were used on all four corners to connect the original frame to the vertical extensions. All adaptations used the same aluminum T-slotted framing as the original frame. The advantage of T-slotted framing is that it quickly adapts to design changes and can be adjusted without the need for complete disassembly. The vertical supports were adjusted to a distance where the entire original frame was submerged. These adjustments were made to ensure the prototype was submerged entirely while the water was static and when the channel was operating. It was ob-

served during operation that the vertical supports generated minimal turbulence. The section being tested is assumed to be far enough away that any turbulence generated by these supports had a minimal effect on the test model. In future experimentation, these supports would have a more streamlined geometry to reduce the turbulence generated from the cavities in the T-slotted framing.

The placement of the slotted rails and the linear bearings are shown in figure 4.33. A close-up image of the top of the near side wall is shown in this figure. The slotted rails along the water channel's sides are shown with linear bearings. These bearings are allowed to move up and down the entire length of the test section. Triangular brackets were used to secure the horizontal frame to the linear bearings. The turbine was placed into the channel, and the bearings were adjusted until the entire system was square to ensure that the turbine was directly perpendicular to the flow during the experiment. The bearings were then securely tightened to the slotted rails so that the prototype was placed in the same position during experimentation. This ensured that there was as little variation as possible in the position of the prototype model inside the channel when the turbine was removed and then replaced.

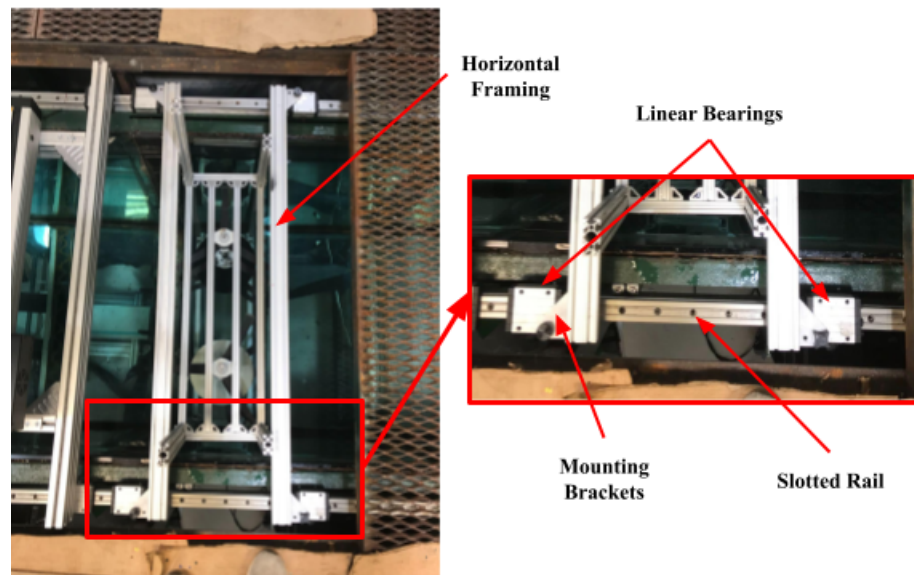


Figure 4.33: Close-up image of slotted rails on the water channel walls

### 4.3.3 Mirror Setup

The typical PIV experiment in the UNCC water channel uses a setup where the test model is mounted to the top of the channel with a servo-controlled traverse. The laser is positioned under the test section generating a vertical laser sheet that spans the streamwise direction of the flow. The camera is mounted on the wall side of the water channel. This setup is excellent for small models that will attach to the traverse. However, this setup is inappropriate when analyzing a vertical axis turbine since the area of interest is a parallel plane to the ground. The typical approach to adapt the PIV setup to capture the flow in this plane would be to use a submerged periscope laser downstream of the model that can project a laser sheet back towards the test section and would cause minimal blockage. This option was not feasible due to cost. The current laser setup used for the channel needed to be modified to fit the experiment.

The solution to adapting the existing equipment for the experiment was to keep the laser under the model but move it downstream and deflect the light sheet toward the model. This assembly would take the place of a submerged periscope laser and allow a laser sheet to be projected onto the test model. The same laser used in the water channel could then be used for this experiment, and the only modification would be its position under the channel. Figure 4.34 shows a schematic of how the mirror assembly was configured inside of the channel and the camera position relative to the model. This image is a side view cross-section of the water channel with the flow moving from left to right. As described earlier in this thesis, the prototype was set into the water channel and secured to the slotted rails. The camera was moved from the typical side mounting point on the channel to a position under the channel. This allowed the camera to capture the flow patterns in the required plane. The original camera mount, consisting of T-slotted framing used for previous experiments, was modified to hold the camera in a position under the bottom of the water channel.

The PIV laser was moved from its typical position, where the traverse is located, to a point further downstream of the testing model. The mirror size was selected to ensure the entire laser sheet was projected downstream. This was required to cut down reflections of the laser beam hitting the mirror mount and for safety concerns due to the laser's high-power nature.

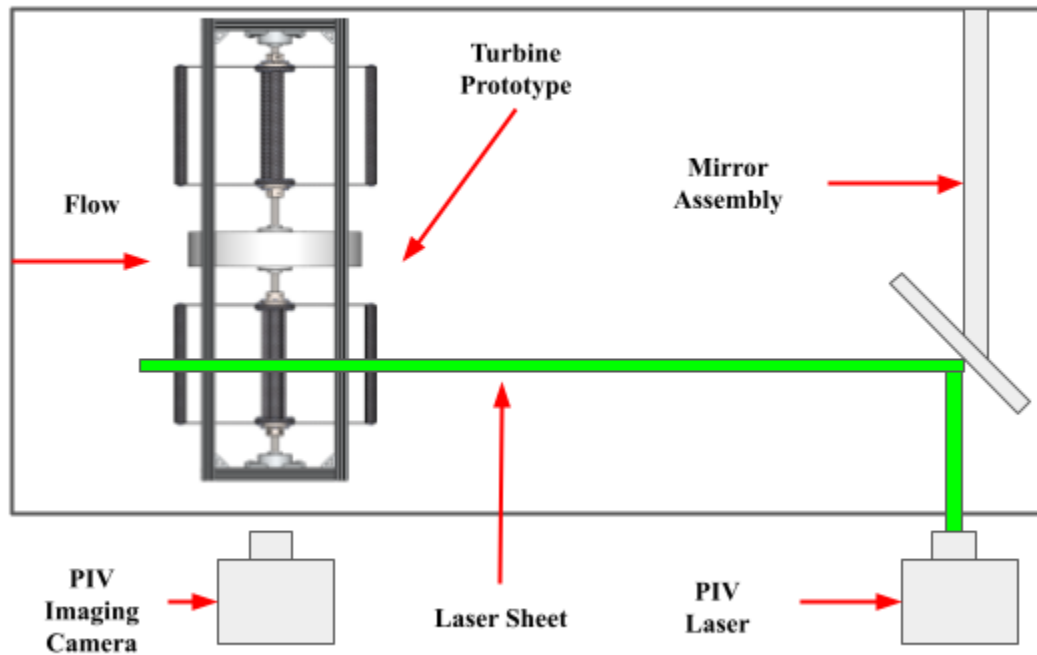


Figure 4.34: Schematic of laser setup used for PIV experiment

A mirror assembly was fabricated to deflect the laser light. The design consisted of a long piece of vertical T-slotted framing connecting to a small mirror with an exterior frame. The vertical support is connected to the mirror frame with a hinged mount for adjustments. The top of the vertical support was secured to a horizontal T-slotted framing. This horizontal support spanned the width of the channel and connected to two additional linear bearings on the slotted rails of the channel walls. The mirror was originally set at a 45-degree angle but needed to be adjusted slightly to account for the deflection of the long vertical mount during the operation of the

water channel. Figure 4.35 below shows an image of the mirror assembly with the laser sheet. This figure shows the light projected through the tempered glass of the channel's bottom panel. The light is deflected from the mirror and projects a quality laser sheet on the test model.

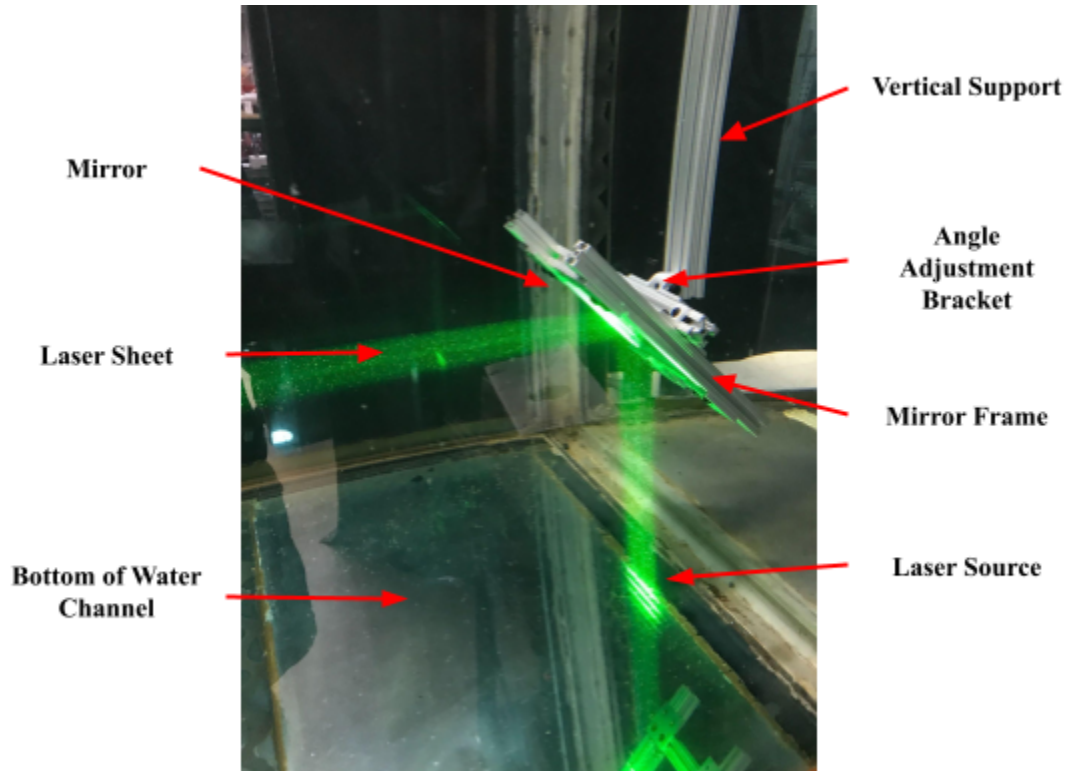


Figure 4.35: Mirror assembly used to position laser sheet at prototype model

#### 4.3.4 Prototype Adaptions for Steady-State Experiment

Design changes needed to be made to the original turbine prototype. Due to the size of the designed complete turbine system, it was decided that it was not feasible to run a transient study. The original prototype of the turbine system was designed for a transient experiment where the turbine blades would rotate, and the flow pattern would be analyzed. This experiment would give insight into the flow dynamics of two counter-rotating turbines and would be used to compare to CFD simulations. After fitting the turbine system to the water channel and reconfiguring the laser and camera position, the task of getting quality images was considered. The highest priority in

the PIV experimentation was to resolve the flow so that the results could be used to verify the CFD simulations. With the adaptations to the camera position and laser required, a transient study could not be conducted for the following reasons. The first problem was a result of the laser position. The laser was positioned downstream and, via the mirror assembly, projected a laser sheet back at the model. One of the significant drawbacks of PIV experimentation is shadows created by objects. PIV only works on areas of fluid where there are light-illuminating tracer particles. When the light hits a test object, a shadow is created behind it, and the flow data is lost. This was the problem with the setup used for the turbine prototype. When the blades spin, shadows are cast on the rest of the model, causing a significant data loss. There are ways to circumvent this problem by reflecting the light sheet at the model using additional mirrors; however, this was outside the scope of this study due to time and cost reasons. The second problem that stopped a transient experiment from being run was the camera field of view. The camera was set at a position under the water channel. The distance between the camera and the bottom turbine did not allow it to capture both turbines. The camera was mounted on the floor under the water channel and could not be lowered further. The way the original prototype was designed did not allow the bottom turbine pair to be moved up without significant changes. The other issue relating to the camera was that the bottom frame obstructed the camera from capturing the flow. The turbine frame could have been designed to position the camera under the prototype. The best solution would be to have mounted the turbine from the top and remove the framing altogether, along with reducing the scale of the turbine system. These solutions would have allowed for a clearer transient solution but were outside of the scope of this thesis once the prototype was built, along with all of the adaptations made to the water channel.

A steady state experiment was settled upon instead of a transient due to the reasons above. One of the most vital aspects of the counter-rotating turbines is the area

where the two turbines pass each other. The flow between the turbines decreases the by-pass effect, where the flow curves around the swept area of turbines instead of passing through. A steady state setup gives experimental data of the velocity when the turbine blades are directly next to each other to analyze this flow feature further and also help validate the CFD results of the steady and transient simulations.

Adaptions needed to be made to the prototype to switch from transient to steady. This required removing components to simplify the model. It was decided that the best way to run a steady state simulation with the modified PIV setup was to remove the top turbine pair. The area between the turbine blades and their wake was the main area of focus of the steady study. This required only one pair of turbines, and due to the camera's position, the bottom pair was the best choice. In addition, since the camera was positioned underneath the water channel, the top turbine would not be in view. To alter the original prototype design to hold the bottom pair of turbines, removing the generator surrogates was also required. Once the top turbine pair was removed from the prototype, the top section of the original frame was moved down. This frame was secured so the rotating shaft could be secured to the frames ball bearings instead of the ball bearing inside the generator assembly. Figure 4.36 below shows the original prototype model configuration with the top and bottom pairs of turbines and the surrogate generators. Figure 4.37 shows the prototype configuration after the adaptions were made to the frame. Using the T-slotted framing, the open gusset brackets were loosened, and the top frame was lowered. The bearings used for the top pair of turbines were kept in place and used as the mounting point for the top of the bottom pair of turbines. This was the turbine configuration used for the steady-state PIV experiment.

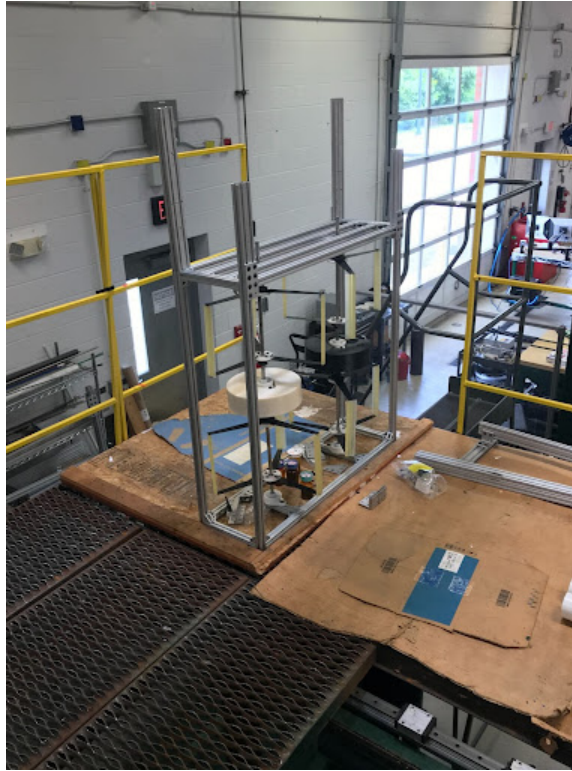


Figure 4.36: Original PIV prototype setup



Figure 4.37: Revised PIV prototype setup

#### 4.3.5 Model Surface Preparation

When running the PIV experiment, the reflectivity and scattering of laser light was another issue that was presented when trying to get high-quality images. This occurs when the light hits the model and reflects, causing the camera not to be able to capture accurate vector fields. The airfoil blades used for the model were manufactured using additive manufacturing. The UV-curing thermoplastic material used in this process was semi-translucent. When preliminary PIV experiments were run, the camera had difficulty picking up the model due to light scatter. These issues can typically be resolved by adjusting the camera's distance or the laser intensity. The camera placement could not be moved due to the modified camera setup. The best approach was to coat the model's blades, being illuminated with an over-the-counter fluorescent orange paint. This orange paint was used with a low pass filter on the camera to generate the clearest image of the particles without reflection.

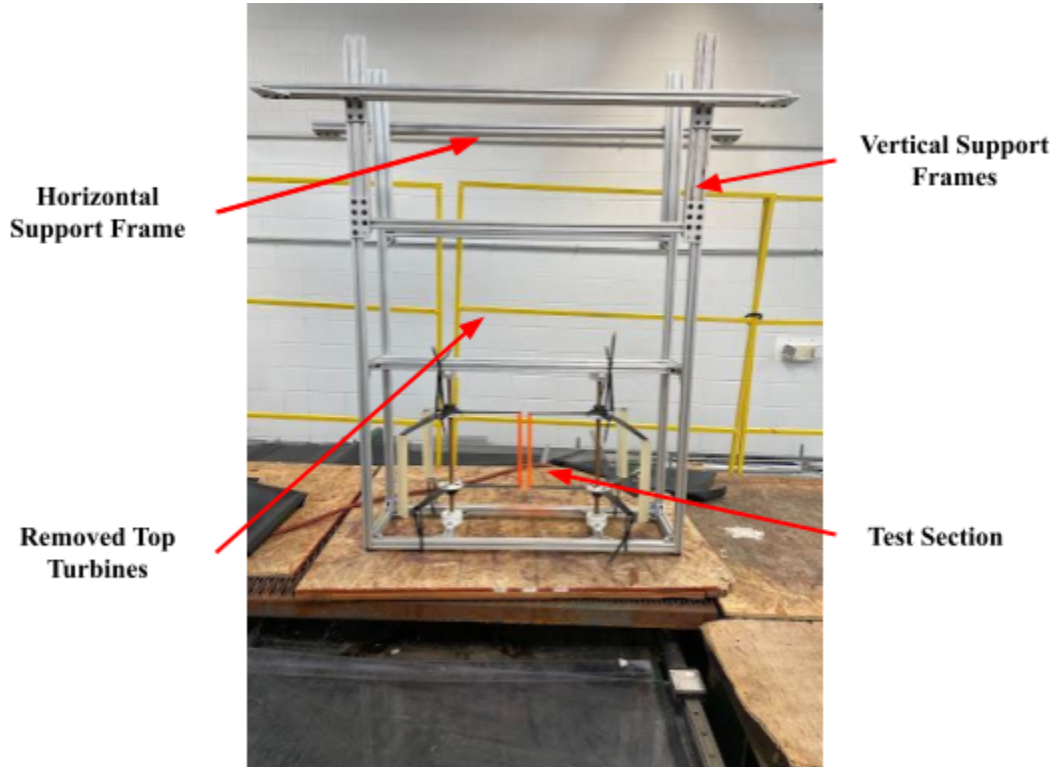


Figure 4.38: Final PIV prototype model setup

Figure 4.38 is the final prototype model used for the steady-state PIV experiment. The airfoils in this image have been coated with this fluorescent orange paint three times. The last adaptation needed for the steady state experiment was securing the rotors so that the two airfoil blades were directly next to each other. The turbines were mounted with ball bearings on both sides. The solution to set them in a static position was to use high-strength cable ties due to their adjustability and ease of removal. The turbines were secured to the frame on the top and bottom.

#### 4.3.6 PIV Equipment

##### 4.3.6.1 Camera

The camera used for capturing the images is the Dantec Dynamics FlowSense USB 2M-165. This camera captures images at 165 frames per second and has a sensor resolution of 1,920 x 1,200 pixels. This camera connects to a computer directly via a USB3 port, so a frame grabber is unnecessary. This camera has a maximum PIV operating velocity of 5  $m/s$ , which makes it ideal for the water channel's maximum 1  $m/s$  velocity.

##### 4.3.6.2 Laser

The Dantec Dynamics RayPower 2000 PIV laser was used in the water channel. The laser operates at a wavelength of 532  $nm$  and an output power of 2000  $mW$ . The beam it produces has a full angle divergence of less than 1.2  $mrad$ . The laser produces a laser sheet that is approximately 2  $mm$  thick. Figure 4.39 shows an image of the laser underneath the water channel as it projects the laser sheet toward the mirror assembly.

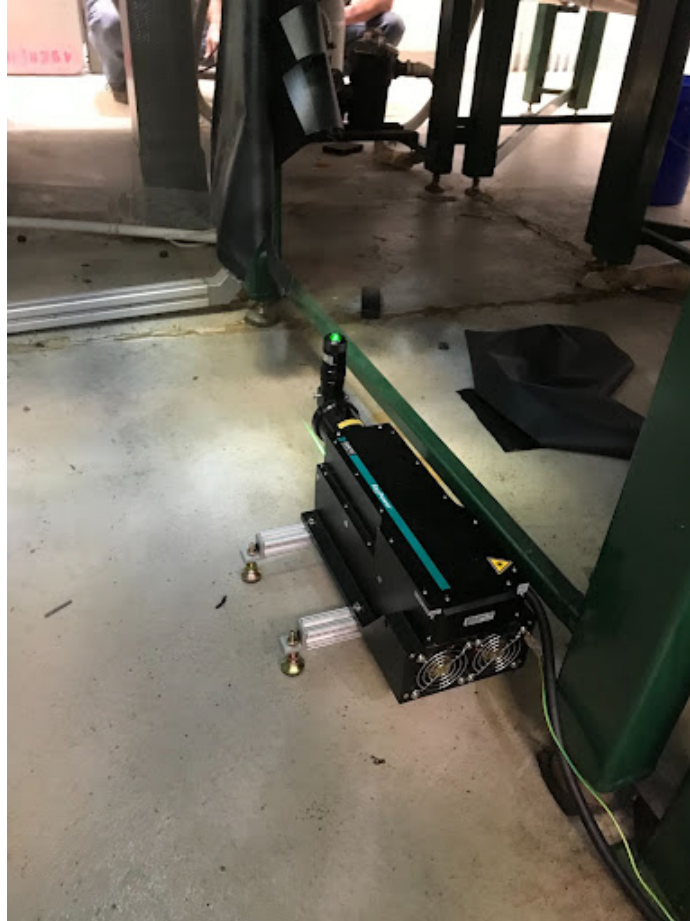


Figure 4.39: Laser used in PIV experiments

#### 4.3.7 PIV Settings

The configuration and equipment settings used for the laser and camera are given in table 4.1 below. These settings were kept consistent throughout the experimentation. Calibration of the PIV setup was done by lowering a piece with a known distance into the water channel and capturing an image. This image was later used in the post-processing software PIVlab to calculate the physical distance of each pixel and the distance each particle travels, leading to velocity vectors to be calculated.

Table 4.1: PIV configuration and setting parameters

Setting	Description	PIV Parameter
Calibration	Object distance from millimeters to pixels	195.38 px/in
Lens distance	Physical distance between the camera lens and the section	-
Inlet velocity	Average inlet velocity on the water tunnel	1 [m/s]
Lens opening	Size of the lens aperture	35mm f2.1 lens
Laser energy	Energy emitted by the laser during acquisition	2000 [mw]
Particle type	Seeding particle diameter and type	1 [ $\mu$ m] Glass hollow
Time	Time interval between frames	10 [ms]

#### 4.3.8 PIV Software

The open-source software PIVlab was used for all post-processing images captured during experimentation. PIVlab is a MATLAB toolbox that allows for velocity vector data to be derived from image data quickly on a personal computer. More information on the background of PIVlab and accuracy tests is available [67]. The software uses a Fast Fourier Transform (FFT) and cross-correlation technique. The FFT and cross-correlation software allows the local velocity vectors to be reconstructed [68]. For all PIVlab image processing, the FFT cross-correlation PIV algorithm with multiple passes (4 passes) and large deforming windows for enhancing the signal-to-noise ratio was used along with velocity vector smoothing and large magnitude velocity vector value outlier rejection. An interrogation area of 64 px was used for the first pass, and an area of 32 px was used for passes 2-4. The Gauss 2X3-point was used as the sub-pixel estimator.

## CHAPTER 5: RESULTS

The overall objective of the PIV experimentation was to compare the flow around the prototype model with CFD simulations. This comparison is intended to verify that the CFD model is simulating the problem's correct physics and validate the CFD results. The ability to accurately validate a 2D or 3D CFD simulation with PIV experimentation is challenging due to the flow field's complexity and the limits of available equipment. Nevertheless, the PIV experimentation produced valuable data about counter-rotating Darrieus turbines and confidence in the preliminary CFD simulation results presented below.

A (3D) computational fluid dynamic study was initially conducted to be used for both steady-state and transient operating conditions of the turbine system. As stated earlier in this thesis, the prototype CAD model needed small and intricate features to be removed to reduce computational cost. A simplified 3D CAD model was generated for a steady-state CFD simulation where the turbine blades were held in place. Due to computational and time restrictions, running this full 3D simulation for all transient simulations was not feasible. The model was reduced to two-dimensional (2D) geometry allowing for a much quicker turnover time for each simulation. This reduction in computational cost allowed for a range of tip speed ratios to be simulated, which would not have been possible for 3D simulations in the given time. The main difference between 2D and 3D simulations is the finite nature of the airfoils where tip vortices are generated. These tip vortices are sources of drag that are not accounted for in 2D simulations; however, their magnitude, when compared to the overall size of the blades, is considered to be small and only causes a slight reduction in the calculated performance parameters.

### 5.0.1 PIV Results

PIV analysis was conducted with a region of interest behind both turbine blades along with the space between the two blades. As stated in the PIV setup section, a transient analysis was not able to be conducted and the focus of the experiment was shifted to a steady study where the blades were held in place. The flow around the static blades was compared to the 3D CFD model to verify that the simulations were accurate. This wake region behind the blades was selected due to this area having the clearest raw PIV images and the lowest amount of laser glare. Before analysis, a mask was generated around the blades and other features. The velocity profile was selected behind both turbine blades to compare PIV experimentation and CFD simulations. The velocity was selected as the parameter to compare to due to the limitations of PIV experimentation being able to only calculate velocity vectors. Figure 5.1 shows the reconstructed PIV velocity magnitude contour plot along with the region of interest and data extraction line with a 1 m/s inlet velocity. In addition, figure 5.1 shows the masks used for the PIV image processing. The masks are areas where shadows are created from the model and there are no reflections from tracer particles in the flow. This loss of data is an additional reason why the flow in the wake region was selected to compare the CFD and PIV data. In this image, figure 5.1, the laser sheet is projected from top to bottom. Figure 5.2 below shows the velocity magnitude contour plot from the 3D CFD simulation at the same point as the laser sheet in the PIV experimentation. The CFD simulation used a 1 m/s inlet velocity boundary condition. The same region of interest and data extraction line is in the wake region. The 3D CFD simulation was used to make sure that the tip vortices are accounted for to make the simulation as accurate as possible when compared to the PIV experimentation.

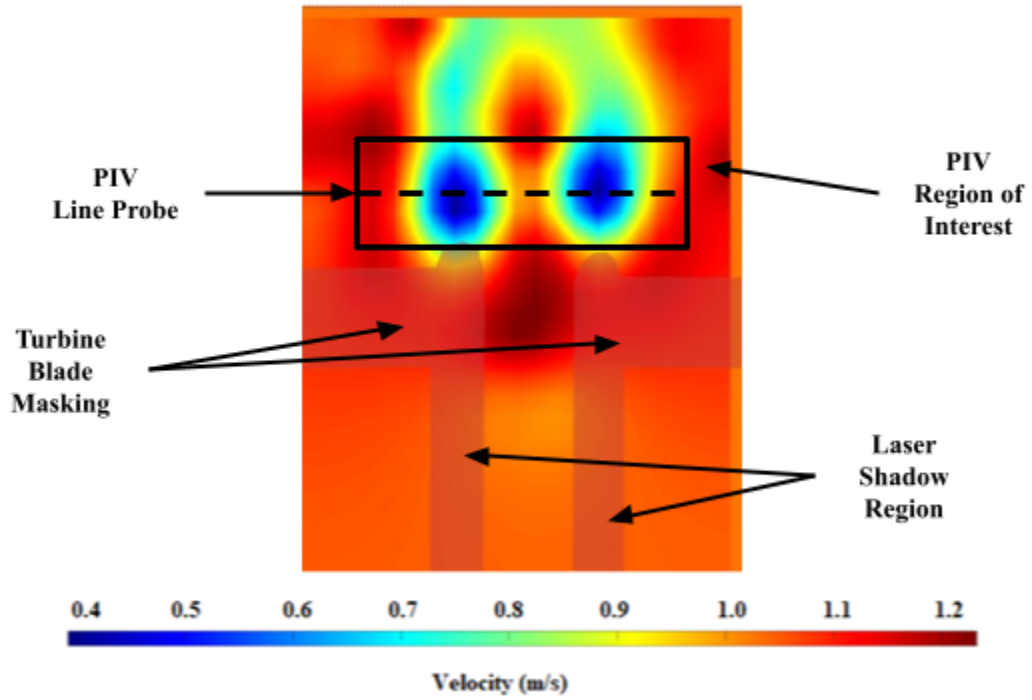


Figure 5.1: PIV velocity vector and contour reconstructed image

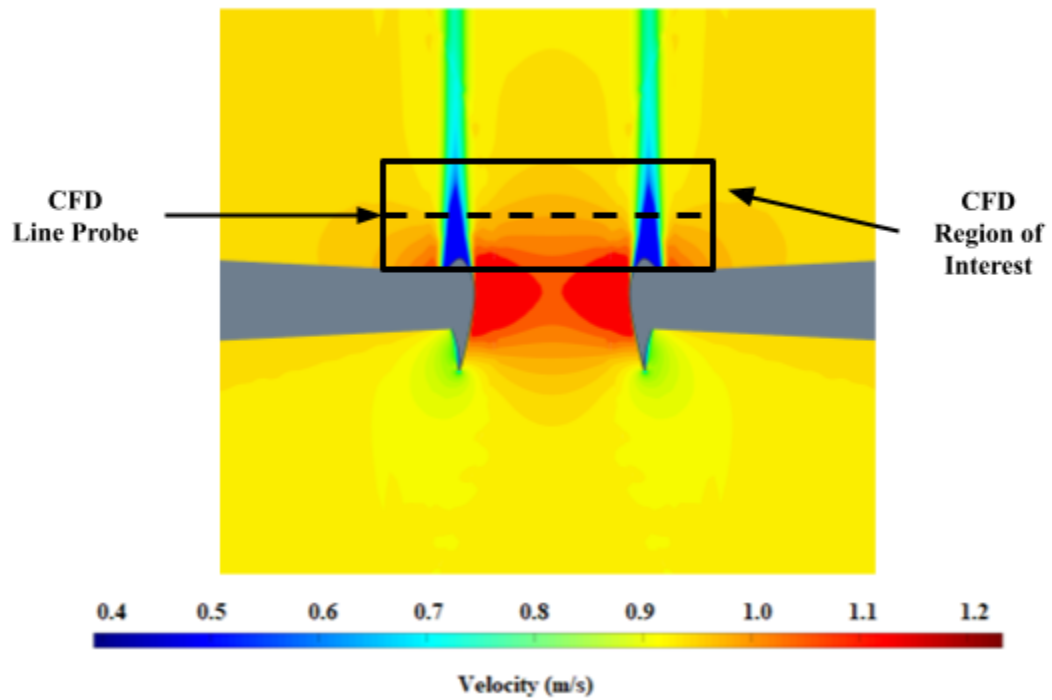


Figure 5.2: CFD velocity vector and contour plots

There are many similarities between the overall flow patterns when comparing figure 5.1 and 5.2. The first is that both show similar wake regions behind the turbine blades. The other distinct feature is the increase in flow velocity between the two blades. The region where the blades are the closest creates an area of high velocity and lower pressure. Figure 5.3 below shows a plot of the velocity magnitude for the PIV and CFD behind the turbine blades along the data extraction line. The plot includes the standard deviation for the PIV data as compared to the CFD data. The most significant deviation between the experimental and computational results occurs near the curves of the blades. This is attributed to the laser glare from the surface of the blades, which causes lower-quality data to be captured from the camera and makes the ability to resolve accurate velocity vectors a challenge. The results from the PIV are within 84% agreement with the CFD when comparing the overall average velocity magnitude of all data points.

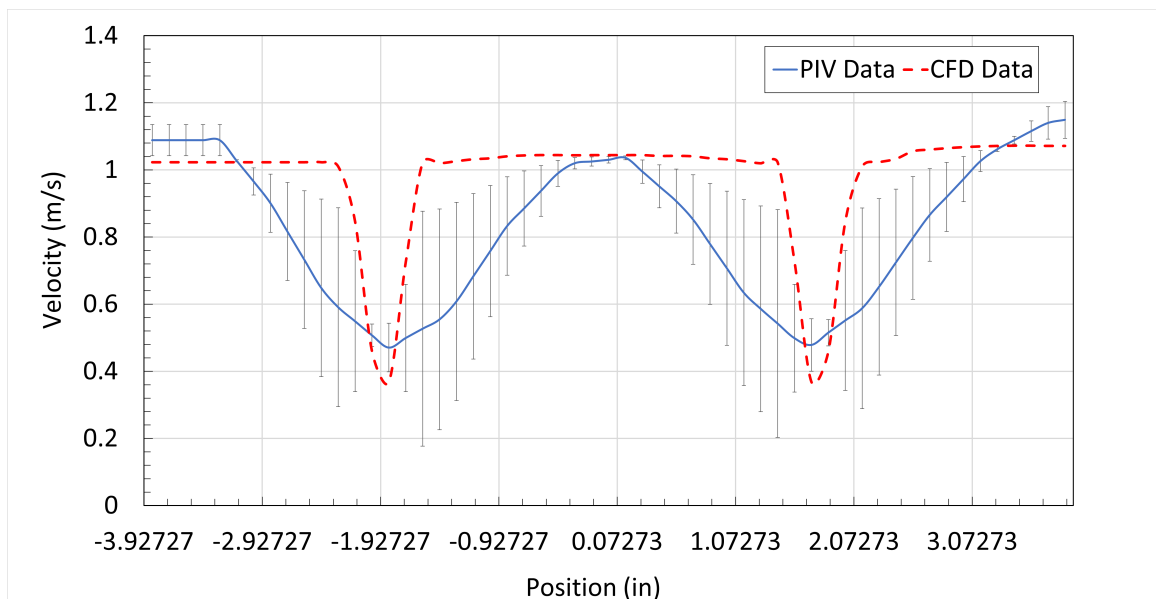


Figure 5.3: PIV and CFD velocity profile extraction in wake region behind turbine blades

### 5.0.2 3D CFD Simulation

The CFD simulation used as a comparison to the PIV experiment was a 3D simulation of the small-scale prototype model. A 3D simulation was used instead of a 2D simulation to capture the effects of the finite length of the blades. Vortices are produced at the tips of each blade and are impossible to capture in a 2D plane. The 3D simulation is the most accurate representation of the actual geometry analyzed in the water channel and is therefore used to compare with the PIV experiment. The 3D simulation also allows for 2D cross-sections that are not only at the mid-plane of the blades but also at various positions along the length of the blades. Along with generating scalar scenes of the velocity in a 2D plane, the flow over the entire turbine was analyzed using the 3D simulation. Identifying where vortices occur in the flow over the turbine model gives insight into how the wake from one blade interacts with others during operation.

#### 5.0.2.1 Q-Criterion

The flow over the 3D geometry of the turbine system was conducted with the blades fixed in position. Holding the blades in a fixed position replicates the conditions the turbine system was subjected to in the PIV experimentation. Since conducting full 3D transient simulations was not feasible, the only 3D simulation was at steady state conditions. The steady simulation, however, still gives a good insight into the flow field, especially the finite aspects of the airfoils. An isosurface of Q-criterion was selected to visualize the vortical structures in the flow field around this complex geometry. There are many ways to identify regions of high vorticity in a flow, with the Q-criterion being one of the most popular. Figure 5.4 below shows the 3D geometry of the two counter-rotating turbines with a Q-criterion isosurface with a value of  $75.0/s^2$ . Overlaid on the Q-criterion isosurface is the velocity magnitude scalar.

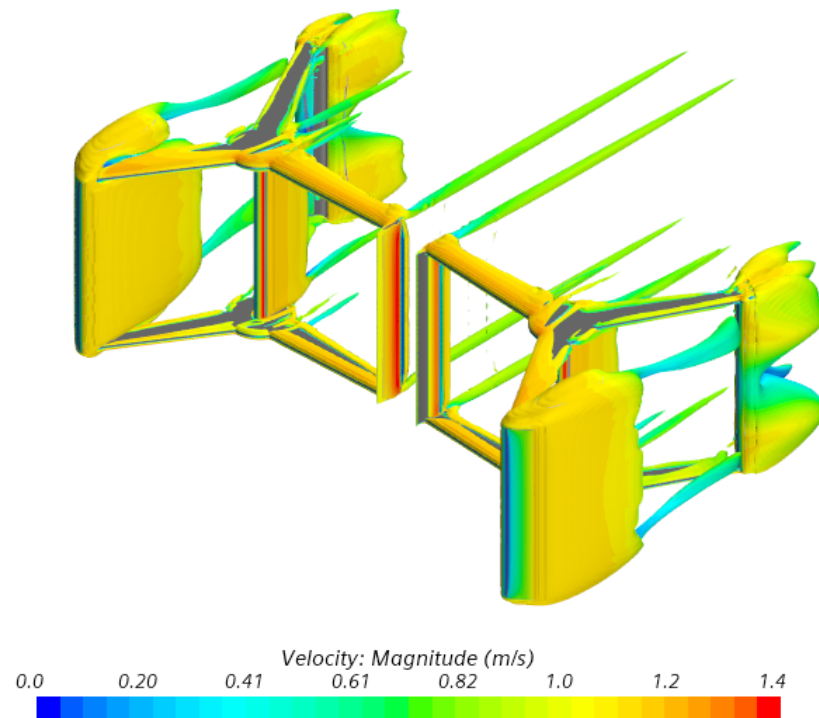


Figure 5.4: ISO-surface of  $Q\text{-Criterion} = 75.0 / s^2$  with a velocity magnitude scalar overlaid

There are a few interesting aspects of the vortical structures to note in the figure 5.4 above. The first is that the blades with a large angle of attack create a large vortical structure behind them. This creates a large wake region behind the turbine blade and can potentially cause the loss of lift from the blades behind it. Additionally, there is a vortical structure behind the center shaft that also has the possibility of causing a vortex-blade interaction. The flow around the two center blades is the second fascinating phenomenon. It can be seen from the velocity magnitude scalar that there is a high velocity in this area. The more interesting phenomenon occurs on the ends of the blades. A tip vortex occurs on both the top and bottom sides of the airfoil blades; however, there is very little vorticity on the rest of the length of the blade. This signifies that the vorticity magnitude is much higher than the strain rate tensor

in these areas, equating to a very defined vortex. Running a transient simulation on this 3D simulation, calculating the performance parameters, and comparing them to the performance parameters of the 2D CFD simulations could help to determine how much of an effect these tip vortices have on the overall efficiency.

## 5.1 2D CFD Simulations

2D simulations were carried out on the two counter-rotating turbines. There is always a compromise that needs to be made between computational cost and reliable results when running computational studies. The objective of the 2D CFD simulations was to understand the turbine's power output with the flow field's counter-rotating aspect taken into account. The main difference between a 2D and 3D simulation is the finite nature of the blades when running a 3D simulation. The 2D simulation cannot take into account the drag induced by the tip vortices on the top and bottom of the blades; however, it is a good approach when assessing the performance output of a turbine.

### 5.1.1 Mesh Independence Study

The first step in analyzing the turbine performance was to perform a mesh independence study. A mesh independence study ensures that the results from a simulation are independent of the grid size and verifies that the solution reflects the specific physics and boundary conditions of the problem. Due to computational resources, a trade-off must be made between run time and simulation accuracy. The level of accuracy required is problem-dependent, and the criteria for satisfactory results necessitates careful decision-making. The mesh independence study for this thesis was carried out for both the steady and unsteady simulations. The steady case was used to help reduce the amount of run time of the simulations and help determine where independence was achieved before running full unsteady simulations. Once a clear understanding of where the independence occurs for the steady state flow over the

turbines, the unsteady simulations were carried out, and the power coefficient over a single revolution was plotted. The results of this unsteady mesh independence verify that the torque and power outputs from the simulations are independent of the mesh size. The power coefficient of the left and right turbines were used as the parameter of interest for the static and dynamic simulations. The power coefficient is the ratio of power generated by the turbine to the entire amount of available energy flowing through the swept area. The power coefficient, therefore, can be used as an overall turbine efficiency at a specific set of operating conditions. The mesh independence study was conducted by selecting and running a coarse baseline mesh. The base size was then reduced in steps until the difference in power coefficients was less than 1 percent. A 1 percent difference was chosen over a 5 percent difference due to the lower computational cost of a 2D simulation. Table 5.1 gives the values of the base sizes for all meshes along with their cell count and the power coefficients for both turbines. A coarse base size of 10 inches was used for the baseline case. The base size was then reduced in half for mesh 1 (M1) and mesh 2 (M2). The base size was reduced by 2.5 for mesh 3 (M3). The refinement ratio is the current mesh cell count divided by the previous mesh cell count. A minimum refinement ratio of 1.1 was used according to Roache’s Grid Convergence Index [69], leading to a minimum of a 33 percent increase in grid size. The lowest refinement ratio used was between the baseline mesh and mesh 1, resulting in a 1.53 ratio in cell count.

Table 5.1: Mesh Independence Results

Mesh	Base Size	Refinement Ratio	Cell Count	Left $C_P$	Right $C_P$
Base	10in	-	85,995	0.09298	0.09291
M1	5in	1.53	131,750	0.09742	0.09772
M2	2.5in	1.61	212,454	0.10189	0.10276
M3	1in	2.01	427,539	0.10183	0.10243

Figures 5.5 - 5.8 below show the changes in the mesh around the airfoil blades. The number of prism layers was kept constant along with the first layer height and the total thickness of the prism layer. Forty prism layers were used with a total thickness of 0.1 inches. This ensured that the boundary layer was contained in the prism layer for all mesh simulations to reduce variability. The first cell height from the wall was  $5.0 \text{ E-}6$  meters to ensure that the wall  $y$ -plus value was under 1. The target cell size on the surface of the blades was selected as 1 percent of the base. The minimum cell size was selected as 0.1 percent of the base size. The trailing edge of an airfoil requires a good quality mesh due to the turbulent flow in this area. The airfoil used in this thesis has a small radius at the trailing edge and therefore requires a mesh refinement in this area. Figure 5.5 below shows how the baseline mesh does a poor job of capturing the airfoil's trailing edge.

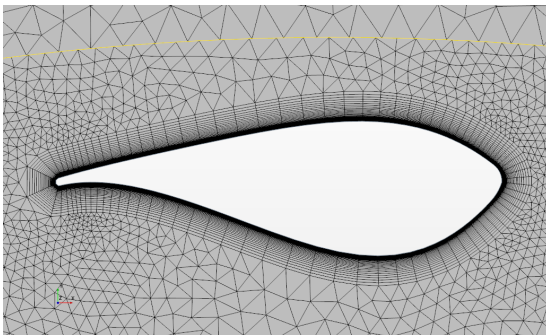


Figure 5.5: Baseline mesh around the cross-section of turbine blade

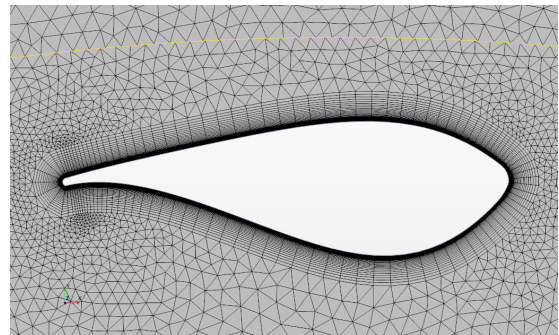


Figure 5.6: M1 mesh around the cross-section of turbine blade

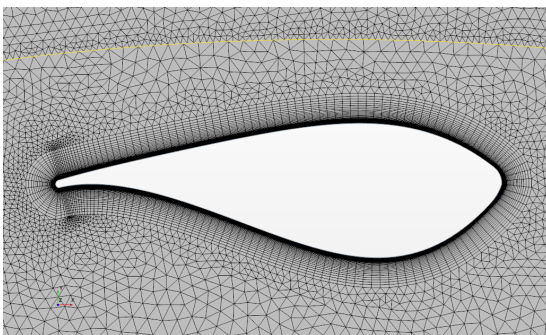


Figure 5.7: M2 mesh around the cross-section of turbine blade

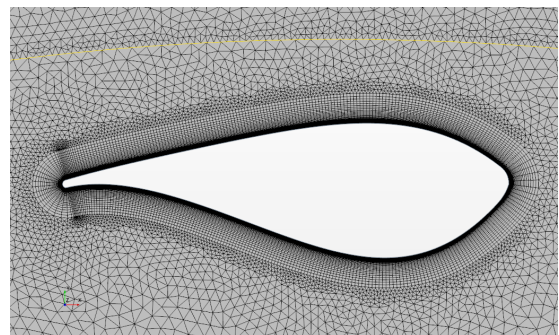


Figure 5.8: M3 mesh around the cross-section of turbine blade

This is due to the radius of the trailing edge being approximately the same order of magnitude as the minimum cell size. The decrease in base size improves the M1 mesh, as shown in figure 5.5, but there is still a coarse density of cells near the trailing edge. As the mesh is further improved with a decrease in base size, there is a higher level of refinement at the trailing edge for mesh 2. There is not much difference in the level of detail in the density of cells at this trailing edge in mesh 3 compared to mesh 2. The power coefficient for both turbines was plotted against the mesh cell count for all four meshes. The value of this power coefficient is only used as a measure of where mesh independence is achieved and is not used to classify the system's performance. It can be seen from figure 5.9 that after mesh 2, the values reach an asymptotic relationship, and further refinement has little change on the power coefficients. Mesh 2 was chosen to be used for the complete unsteady analysis since any further refinement does not provide a more accurate solution. A mesh independence study strives to achieve the coarsest mesh possible that still gives accurate results that do not vary with increases in cell count. The slight changes after mesh 2 in the values of the power coefficient are considered negligible and inside the tolerance of a 1 percent difference. The power produced by the right and left turbines are nearly identical, which is expected, with slight variations attributed to the solvers' numerical errors.

The percent difference of the power coefficients between meshes was calculated for M1-M3 and is given in table 5.2. Figure 5.10 shows the percent difference of that mesh with the previous mesh. Mesh 1 was compared to the baseline mesh. The relative 1 percent difference is highlighted as dotted lines to show where the acceptable level of refinement is located. This plot shows that after mesh 2, any further refinement would fall inside of the allowable tolerance. All of the percent differences are within around 5 percent or under, leading to an even higher level of confidence in the mesh independence study results. The baseline case could have been coarser if a 5 percent difference had been used as the independence criteria.

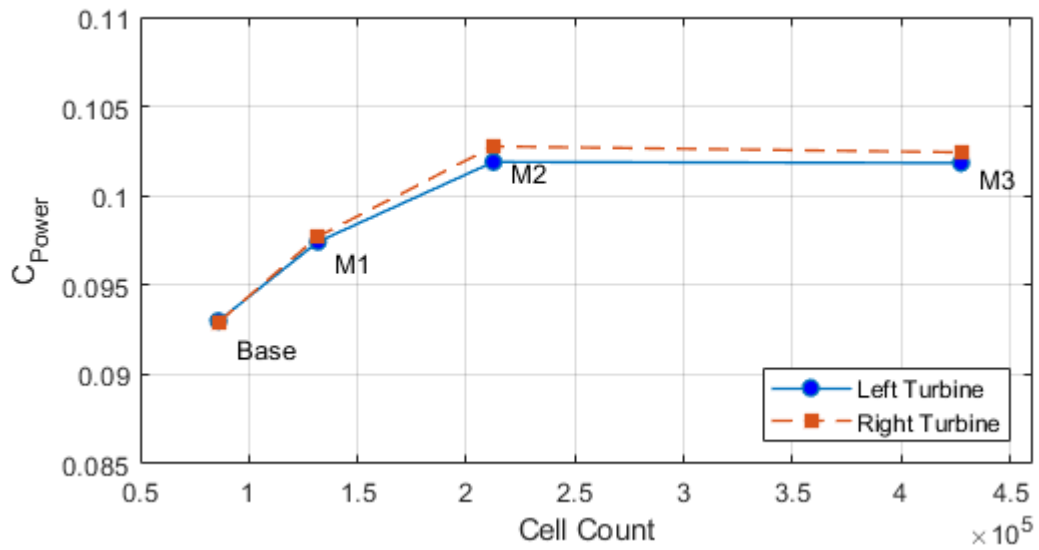


Figure 5.9: Power coefficient vs. mesh size for steady mesh independence study

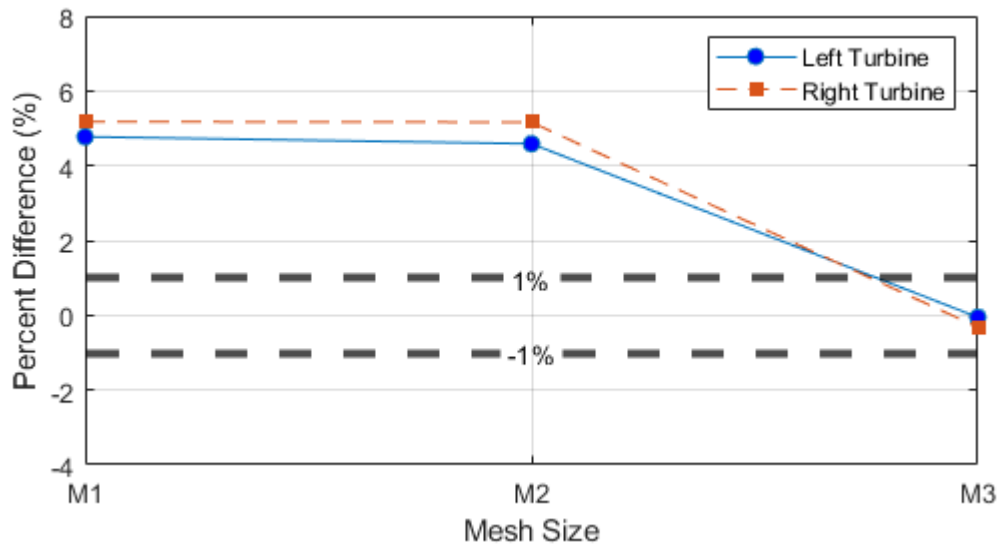


Figure 5.10: Percent error plot from previous mesh for steady simulation

Table 5.2: Percent Difference

Mesh	% Difference Left	% Difference Right
M1	4.77	5.17
M2	4.59	5.16
M3	-0.05	-0.32

Once independence was found for the steady simulation, the motion was added to simulate the movement of the turbines leading to a transient or unsteady simulation. Unsteady simulations for the baseline through mesh 2 were conducted to see how the power coefficient varied over a full rotation between the meshes. Since mesh 2 was decided as the point of independence for the steady case, mesh 3 was not included in the unsteady simulation. For the unsteady mesh independence, the same parameters were used as the steady case; therefore, the mesh size was the only variable that changed. A time step of 0.002 seconds was used for each transient simulation. Each simulation was run for 3 complete revolutions. To achieve a tip speed ratio of 2, a rotational velocity of  $9.263 \text{ rads/sec}$  was used, equating to a total simulation time of 2.0348 seconds. Five hundred iterations were used to ensure the solution converged at each time step. This is a large number of inner iterations; however, due to the limited size of a 2D simulation mesh, it did not hinder the simulation run time to a significant degree. Figure 5.11 below is the plot of the power coefficient for each mesh over a single revolution of the turbine. The baseline mesh power output shows the most variation over a full rotation. The trough of the plot of the baseline mesh shows noise which can be attributed to the mesh coarseness. Mesh 1 and mesh 2 show power coefficients that are very similar, which is the expected result. Mesh 2 has a slightly higher overall power coefficient plot; however, the difference is negligible. The three peaks correspond to each of the blades producing peak power during a full rotation. After each large peak in power, three small dips can be attributed to the wake-blade

interaction. The power coefficient peak values in this plot are approximately 0.35, which, compared to similar turbines, is low. It is important to note that this is the power coefficient of the small-scale turbine operating at a freestream flow velocity of  $1\text{ m/s}$ . This would be the power coefficient of the turbine system if it were deployed into an ocean environment at the current small-scale size and a  $1\text{ m/s}$  flow velocity. In a later section of this thesis, the full-scale turbine performance will be analyzed by adjusting the radius of the small-scale simulation and calculating total power output.

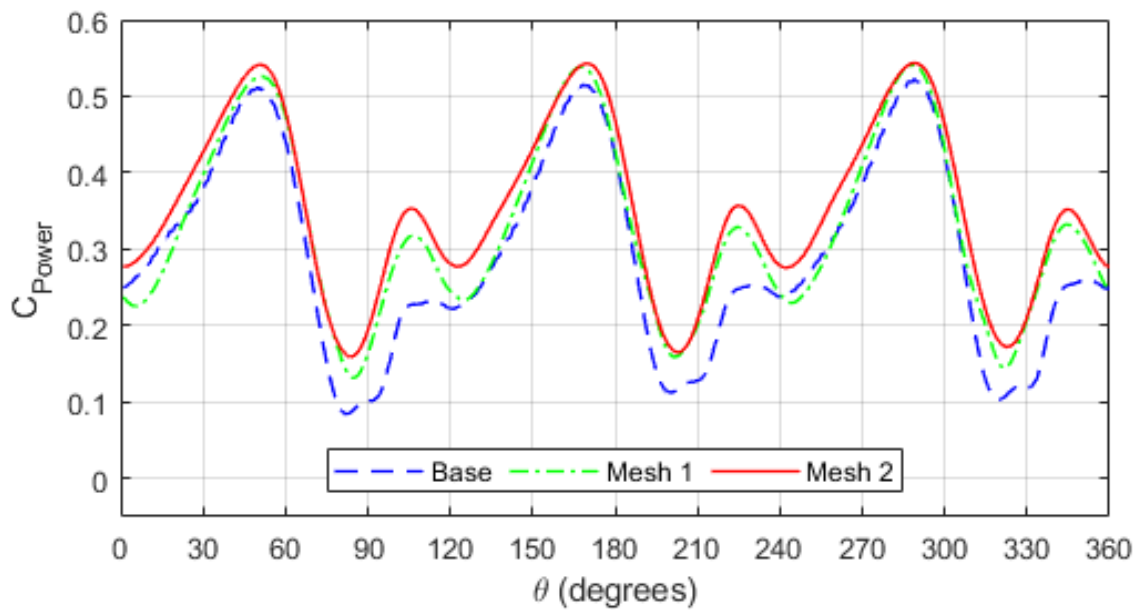


Figure 5.11: Power coefficient vs azimuth angle for mesh sizes

### 5.1.2 Tip Speed Ratio Study

The performance of any turbine is mainly dependent on two factors. The first is the geometry of the turbine, including the chord length, turbine radius, turbine height, number of blades, and airfoil design. The second factor that significantly affects the overall efficiency is the tip speed ratio that a turbine is specified to operate at during steady-state conditions. The tip speed ratio, as defined earlier in this thesis, is the ratio between the tangential velocity of the blade to the incoming freestream velocity. A tip speed ratio study is required to determine the optimal tip speed for the given turbine geometry. This thesis aims to analyze a turbine operating at low flow conditions commonly occurring in river or estuary environments. For these reasons, it was decided to limit the freestream velocity since there is little potential for higher flow velocities in these marine environments. The freestream velocity in all CFD simulations was set at a standard 1 m/s; therefore, a change in tip speed ratio in this paper results only in a change in rotational velocity. A tip speed ratio study was conducted using the mesh from the mesh independence study to find the approximate optimal tip speed ratio for the case of the counter-rotating turbine geometry. This results in finding a rotational velocity that generates the highest power coefficient, leading to the highest efficiency. For each tip speed ratio simulation, a time-step corresponding to 1 degree of rotation was chosen to allow for sufficient resolution. During each time step, 50 inner iterations were run to ensure convergence. Each simulation was run for a total of 8 revolutions to allow the transients of the flow to dissipate. The average power coefficient over a full rotation was calculated for tip speed ratios of  $\lambda = 1$ ,  $\lambda = 1.5$ ,  $\lambda = 1.75$ ,  $\lambda = 2$ ,  $\lambda = 2.125$ ,  $\lambda = 2.25$ ,  $\lambda = 2.375$ ,  $\lambda = 2.5$ ,  $\lambda = 2.75$ , and  $\lambda = 3$ .

Table 5.3: Tip speed ratios and average coefficient of power over a single revolution

TSR	Rotational Speed (rads/s)	$C_{P_{avg}}$
1	4.632	0.06634
1.5	6.948	0.1413
1.75	8.106	0.2188
2	9.264	0.3506
2.125	9.843	0.3895
2.25	10.421	0.4237
2.375	11.000	0.4488
2.5	11.580	0.4685
2.75	12.738	0.4895
3	13.895	0.4369

Figure 5.12 below shows the results of the power coefficients of the tip speed ratios listed above in table 5.3. The figure shows a sharp increase in power coefficient starting around  $\lambda = 1.75$  and peaking around  $\lambda = 2.75$  and then declining afterward. This is the typical relationship between the power coefficient and tip speed ratio. Any rotational velocity lower than this value is suboptimal because the airfoil blade is not generating the full potential lift available. This loss of potential lift is what causes a less efficient system. The increasing rotational velocity of the blades past this optimal TSR decreases the performance. This is due to the drag generated by the airfoil overpowering the amount of lift and decreasing the system's overall efficiency. Figure 5.12 therefore shows that the most efficient operating tip speed ratio is  $\lambda = 2.75$ . It is important to note that this peak power coefficient is strictly for the turbine configuration with counter-rotation, and with the geometry listed above in this thesis. Changing the geometry or removing one of the turbines would alter the peak tip speed ratio.

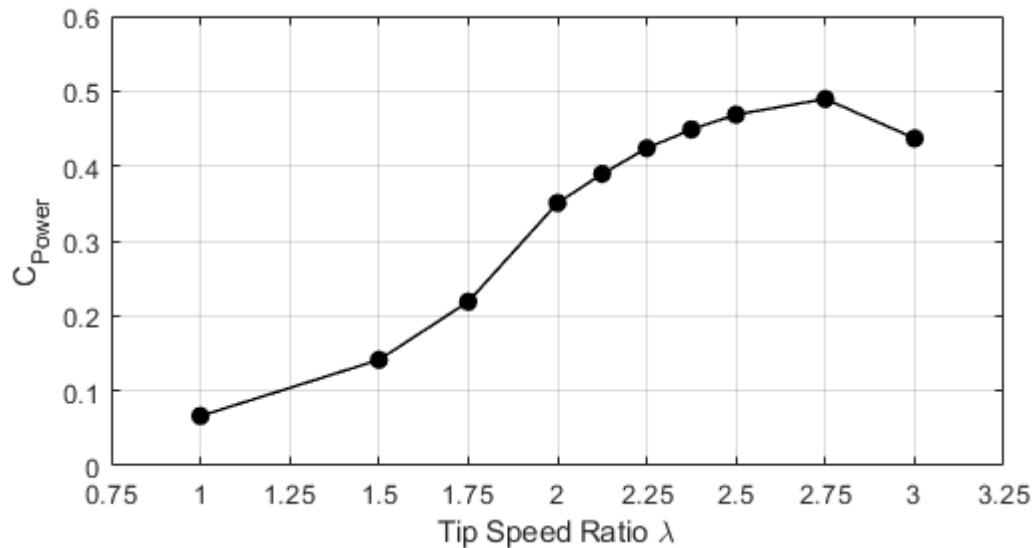


Figure 5.12: Coefficient of power as a function of tip speed ratio

The power coefficient curve of the optimal tip speed ratio of  $\lambda = 2.75$  is given in figure 5.13. The power coefficient is plotted with the azimuth angle for a single revolution. All tip speed ratio simulation curves show similar characteristics concerning the regions where power is produced from each blade. Each power coefficient plot shows two peaks. These two peaks are labeled as the primary and secondary in figure 5.13 below. The primary peak in power corresponds to the lift produced by the turbine blade, accelerating it further in the direction of rotation. This primary peak would generally be observed as a stand-alone peak in a system that contains a single rotating turbine. An interesting phenomenon occurs when a second turbine is added to the system in parallel but in counter-rotation with the original turbine. A secondary peak is observed in the power curves in a system with counter-rotating turbines. This secondary peak in torque corresponds to the moment when the two turbines pass each other and is due to the complex flow patterns in this region. The flow in this area will be analyzed further in this thesis to understand the pressure and velocity field and determine the mechanism causing this secondary peak in torque. It is hypothesized that this secondary power peak increases the system's overall efficiency by capturing

potential energy and converting it into kinetic energy that would typically be lost in a single turbine system.

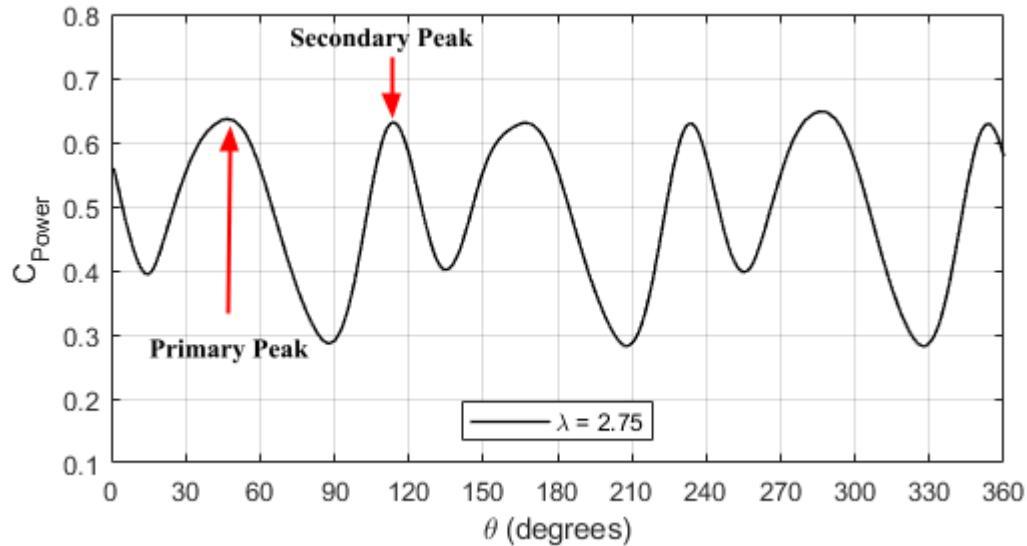


Figure 5.13: Power coefficient for the tip speed ratio of  $\lambda = 2.75$

To give more insight into how the primary and secondary peaks in power change with tip speed ratio, the power coefficient plots for tip speed ratios of  $\lambda = 2.5$  and  $\lambda = 3$  are plotted along with the optimal tip speed ratio of  $\lambda = 2.75$ . Figure 5.14 below shows all three power coefficient plots for the given tip speed ratios over a single revolution for one turbine. A tip speed ratio of  $\lambda = 2.5$  gives a curve with a higher primary peak and a lower secondary peak than a tip speed ratio of  $\lambda = 2.75$ . The slower rotational velocity for  $\lambda = 2.5$  generates a smaller low-pressure region between the blades resulting in a smaller suction effect. This results in a smaller average power coefficient over the entire revolution.

A tip speed ratio of  $\lambda = 3$  produces a curve with a smaller primary and secondary peak compared to a tip speed ratio of  $\lambda = 2.75$ . This generates an overall power coefficient lower than a TSR of  $\lambda = 2.75$ . There is a balance between the amount of lift generated in the direction of rotation and the overall drag produced by the airfoil. The airfoil reaches a specific rotational speed where this lift-to-drag ratio is the most

efficient. Once this rotational speed is passed, the drag force takes over in magnitude and reduces the torque the system can produce. This increase in drag is the cause of a lower average power coefficient over the revolution.

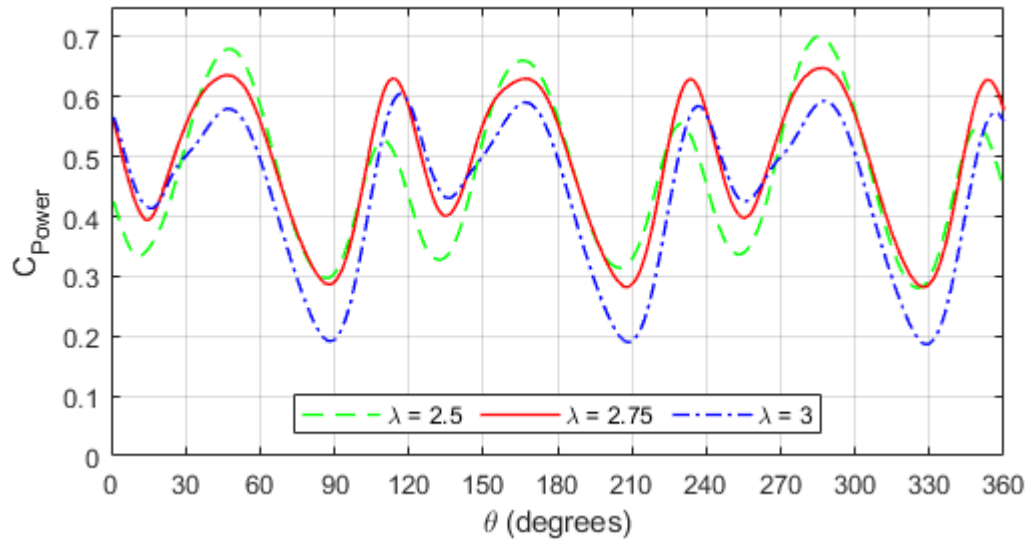


Figure 5.14: Power coefficient plots for  $\lambda = 2.5$ ,  $\lambda = 2.75$ , and  $\lambda = 3$

Figure 5.15 below shows two subplots. The top plot is the combined power coefficient of one turbine over a single revolution for a tip speed ratio of 2.75. The bottom plot in this figure is the power coefficient for each turbine blade over a single revolution for a TSR of 2.75. These two plots demonstrate how each blade's peaks correspond to the turbine's overall power output. Each blade produces a significant peak in power corresponding to the primary peak in power observed in the combined plot. Therefore, the magnitudes of the peaks in power are related to the number of blades in the system. Increasing the number of blades would decrease the magnitude of spikes in power output. The overall efficiency would decrease slightly; however, this would, in turn, decrease the load on the individual components of the system, causing a longer lifespan.

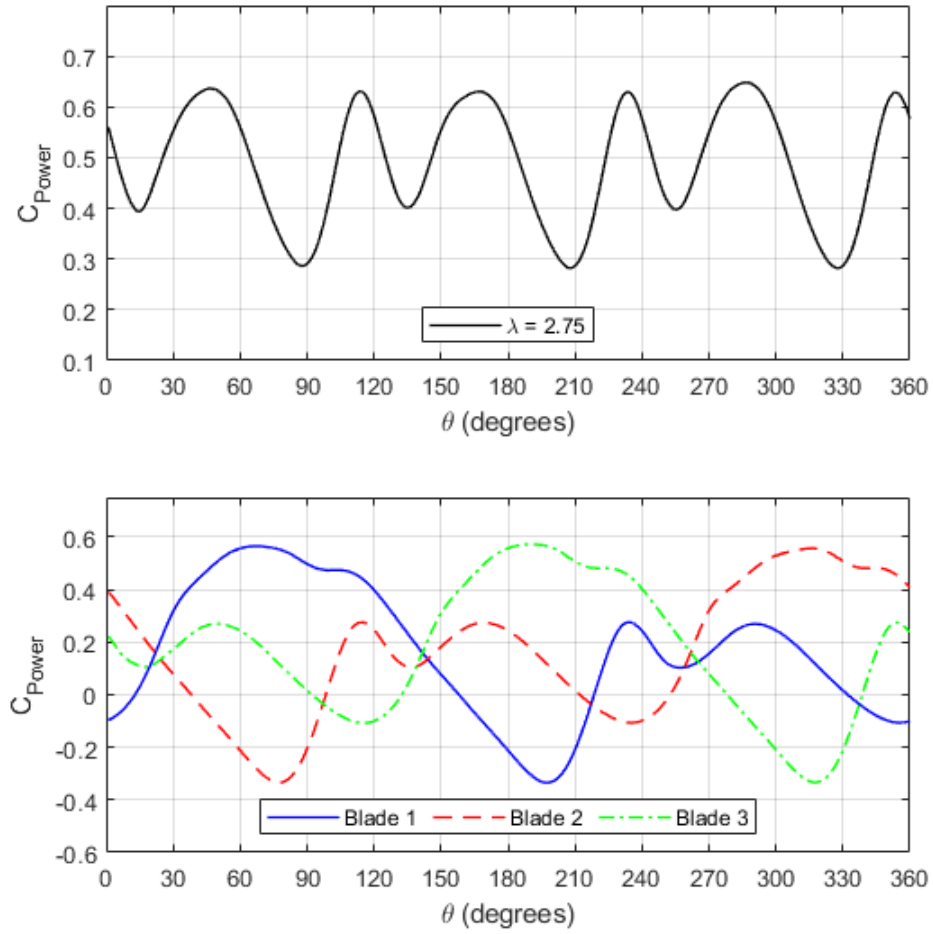


Figure 5.15: Individual blade vs combined power coefficient over a single revolution

### 5.1.3 Torque Ripple

The torque coefficient for all three blades combined over a single revolution is given in figure 5.16. The torque coefficient gives insight into the self-starting profile of a turbine. Darrieus turbines typically have problems with self-starting capability, one of their significant drawbacks. This is due to the relatively large peaks in torque generated from one blade and the associated drop in the transition section before the torque of the next blade. Several variations of Darrieus turbines have tried to improve this self-starting capability, such as helical shapes with different angles of attack along the blade at all times.

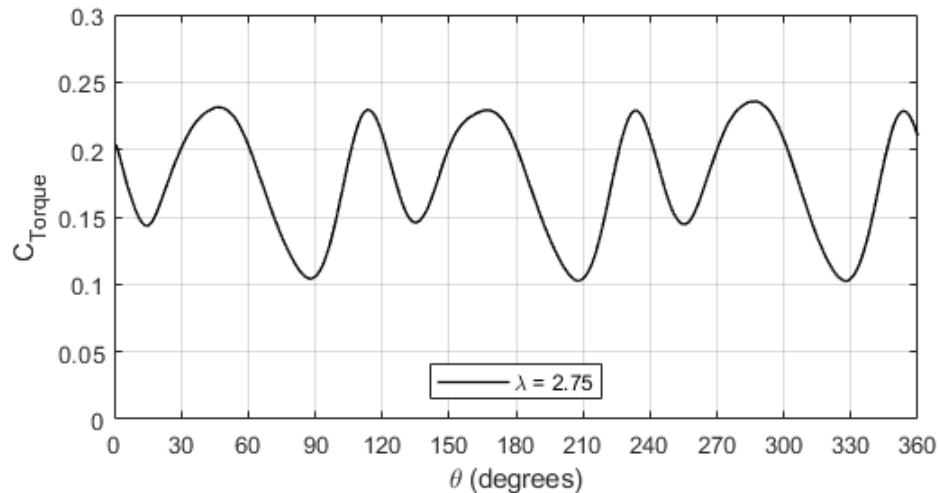


Figure 5.16: Torque coefficient for the tip speed ratio of  $\lambda = 2.75$

Torque ripple is a mechanical phenomenon in any turbine, whether a vertical or horizontal axis-based system. Torque ripple is defined as the time variations in torque that are transmitted throughout all components of the system while it is in operating conditions. In a vertical-axis turbine, this torque ripple is generated by the blades constantly changing the angle of attack from the apparent flow direction. The equation for the torque ripple used for this thesis is defined as the harmonic oscillation of torque about a mean value and is given in equation 5.1 [70].

$$TRF = \frac{T_{max} - T_{min}}{T_{avg}} \quad (5.1)$$

Lower TRF values signify smaller torque deviations from the mean torque value resulting in lower stresses on the system components. The reduction of material fatigue of components over time is significant to minimize in a marine environment due to the already harsh conditions that turbines are subjected to. In the case of the torque output for the small-scale turbine at a tip speed ratio of 2.75, the calculated torque ripple factor was 0.7493. The torque ripple factor of the other tip speed ratios analyzed previously for the power coefficient was calculated from  $\lambda = 1.5$  to  $\lambda = 2.75$ . The torque ripple factor for all tip speed ratios is plotted in figure 5.17. A TSR of  $\lambda = 1.5$  has a considerable variation from the mean value, and therefore there is a large amount of stress throughout the system. There is a drastic drop in the TRF from a TSR of  $\lambda = 1.5$  to  $\lambda = 2$ , where the rate of decrease is much slower. Based on this data, the tip speed ratio of the turbine system should stay at or above  $\lambda = 2$  to avoid the most harmful high torque variations that occur below this number. There will inevitably be some torque variations based on the nature of vertical-axis turbines.

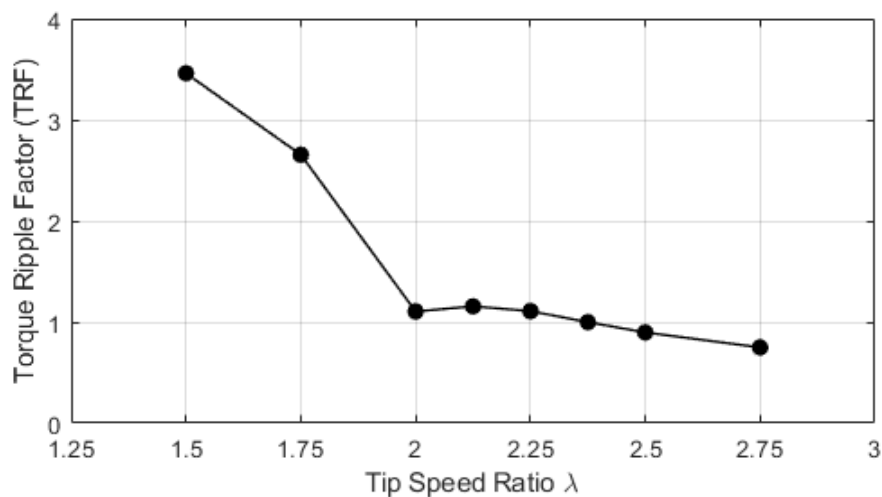


Figure 5.17: Torque ripple factor as a function of tip speed ratio

#### 5.1.4 Flow Field Analysis

The flow field in the region between the two closest turbine blades is focused on in this section. The secondary peak in torque corresponds directly to the point where the blades pass each other. Contour plots of the flow field were captured in 15-degree azimuth angle increments to give a sufficient resolution of the transient flow field. Due to the periodic nature of the power curve, only the first instance of the blades passing each other was analyzed; however, it can be assumed that the same flow pattern occurs for blades 2 and 3 as they pass by each other. The turbine blades are precisely apart from each other at  $\theta = 120$ . Therefore, the azimuth angles  $\theta = 105$  and  $\theta = 135$  were chosen to be analyzed to understand the flow before and after this occurrence. The contour plots of the velocity magnitude, pressure coefficient, and vorticity in the z-direction are plotted for the above azimuthal positions. These contour plots allow the flow field corresponding to the second peak to be further analyzed. In addition, the pressure coefficient for all three blades of a single turbine was plotted in 15-degree increments from  $\theta = 0$  to  $\theta = 135$ . These contour plots allow for understanding how the pressure changes on each blade during 1/3 of the rotation of the turbine.

The pressure coefficient for azimuth angles  $\theta = 105$ ,  $\theta = 120$ , and  $\theta = 135$  are given in figures 5.18a - 5.18c. The pressure coefficient allows relatively high and low-pressure regions in the flow field to be visualized. There are a few interesting things to note in the pressure coefficient figures. In all three contour plots, there is a high-pressure region at the airfoil's leading edge. This corresponds to the stagnation point on the airfoil, where the fluid velocity becomes zero. Figures 5.19a- below give the velocity magnitude contour plots for azimuth angles  $\theta = 105$ ,  $\theta = 120$ , and  $\theta = 135$ . It can be observed from these figures that there is a decrease in velocity around the leading edge of the turbine blade, which goes along with the increase in pressure.

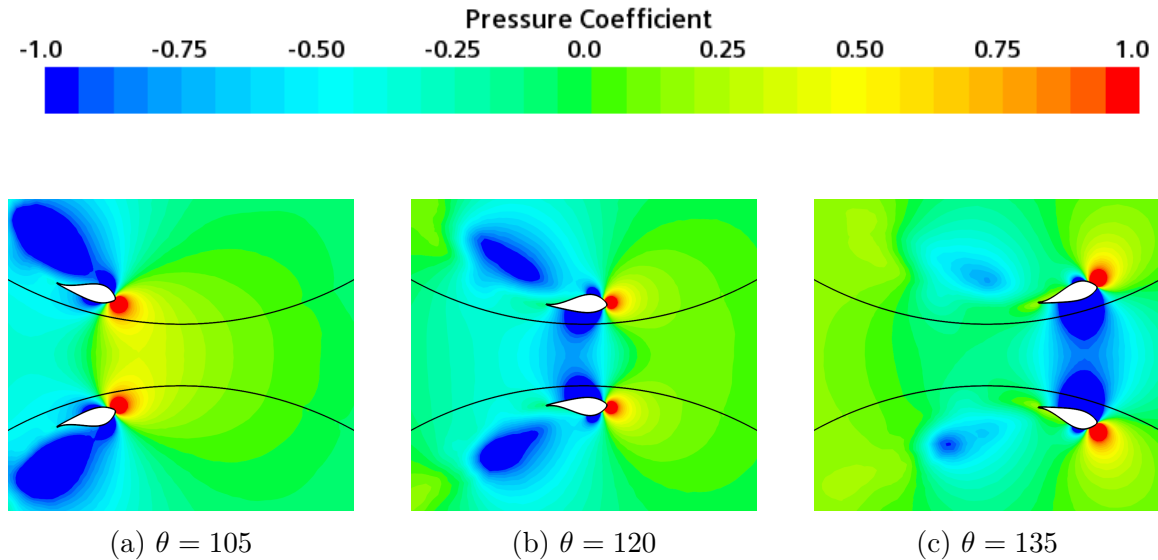


Figure 5.18: Instantaneous pressure coefficient contours

The second interesting thing to note is the decrease in pressure on the upper surface of the airfoils. Figure 5.18a shows the pressure contour for an azimuth angle of  $\theta = 105$  and is representative of the flow as the two blades approach each other. In this figure, there is a small low-pressure zone on the top surface of the turbine blade. In the wake region of the blade, there is a sizeable low-pressure zone which is expected due to the high tangential speed of the airfoil as compared to the freestream velocity. When the turbine blades move from an azimuth angle of  $\theta = 105$  to an azimuth angle of  $\theta = 120$ , there is a change in the low-pressure area on the upper surface of the turbine blade and is visualized in figure 5.18b. A large low-pressure region occurs between the two blades. This azimuth angle is where the secondary peak in torque occurs. This is hypothesized due to the interaction in low-pressure regions generated between the two blades. This low pressure on the upper surface occurs in single turbine systems; however, there is an increase in the magnitude of these low-pressure zones due to a combination effect from a second turbine. The increase in low pressure on the suction surface of the airfoil contributes to an increase in lift on that particular blade and helps increase the force further in the direction of rotation.

Figure 5.18c shows the pressure coefficient contour for an azimuth angle of  $\theta = 135$ . This is where the turbine transitions from the secondary peak in torque to the primary peak in power. The low-pressure region on the suction surface of the airfoil is more extensive in magnitude than for an azimuth angle of  $\theta = 120$ . As the rotation of the blade continues past an azimuth angle of  $\theta = 135$ , this low-pressure region gets even more prominent. This decrease in pressure on the upper surface compared to the lower surface contributes to a differential in pressure, producing lift. The increase in lift on the blade propels it further in the direction of rotation, creating a moment upon the center axis, causing what is seen as the primary peak in power. The proximity of the two turbine systems, therefore, increases the available power generated by both of the turbines by the mechanisms of increased velocity and decreased pressure in the near region of the two closest blades.

Figures 5.19a-5.19c below show the velocity contours of this region between the two turbine systems. It is interesting to note in these images the wake generated by the blades as they pass each other. Figure 5.19a shows a wake region with a relatively high velocity compared to the freestream velocity. As the blade moves from an azimuth angle of  $\theta = 105$  to  $\theta = 135$ , the velocity magnitude decreases in this wake region. An associated increase in pressure coefficient is given in figure 5.18. The increase in velocity magnitude and decrease in pressure in the wake region of the blades means there is a possibility that cavitation is occurring. Cavitation occurs when the pressure drops below the fluid's vapor pressure causing vapor-filled bubbles to form. When the pressure increases, these pockets of vapor collapse, causing a shock wave. If the shock wave of these pockets occurs next to a solid wall, such as the surface of turbine blades, damage to that surface can happen. This can cause blades and other parts to fail and raise costs. Further research would need to be conducted into this phenomenon. If cavitation occurs, the tip speed ratio would need to be reduced to remove this effect, even at the expense of lowering overall efficiency. The last important aspect of the

velocity magnitude contours is the lack of a recirculation zone in the region between the turbine blades. Due to the flow's nature, vortices shed from the trailing edge of the blades in the region between turbines appear to be washed out by the freestream velocity. Vortex-blade interactions typically occur inside the turbine's swept area and can cause a loss of lift and, therefore, a decrease in overall efficiency. Vortices appear not to affect the blades as the turbines pass each other.

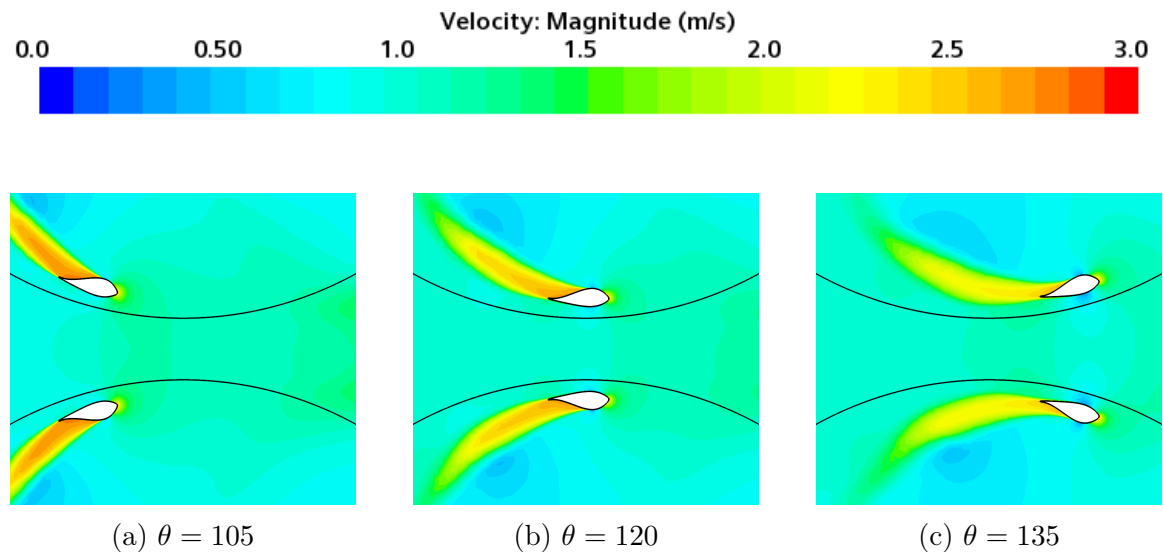


Figure 5.19: Instantaneous velocity magnitude contours

Figure 5.20 given below shows the pressure coefficient contours for the right turbine over a third of a revolution from  $\theta = 15$  to  $\theta = 135$ . The pressure field for all three blades can be visualized in this figure as their relationship with the peaks in power output. The primary peak in power corresponds to blade 1, producing lift from approximately  $\theta = 15$  in figure 5.20a to  $\theta = 45$  in figure 5.20c. A high-pressure region occurs on the bottom surface of the airfoil that is caused due to the rotation of the blades through the water and the pressure from the freestream flow field. A low-pressure region forms on the top side of the blade, causing the blade to produce lift.

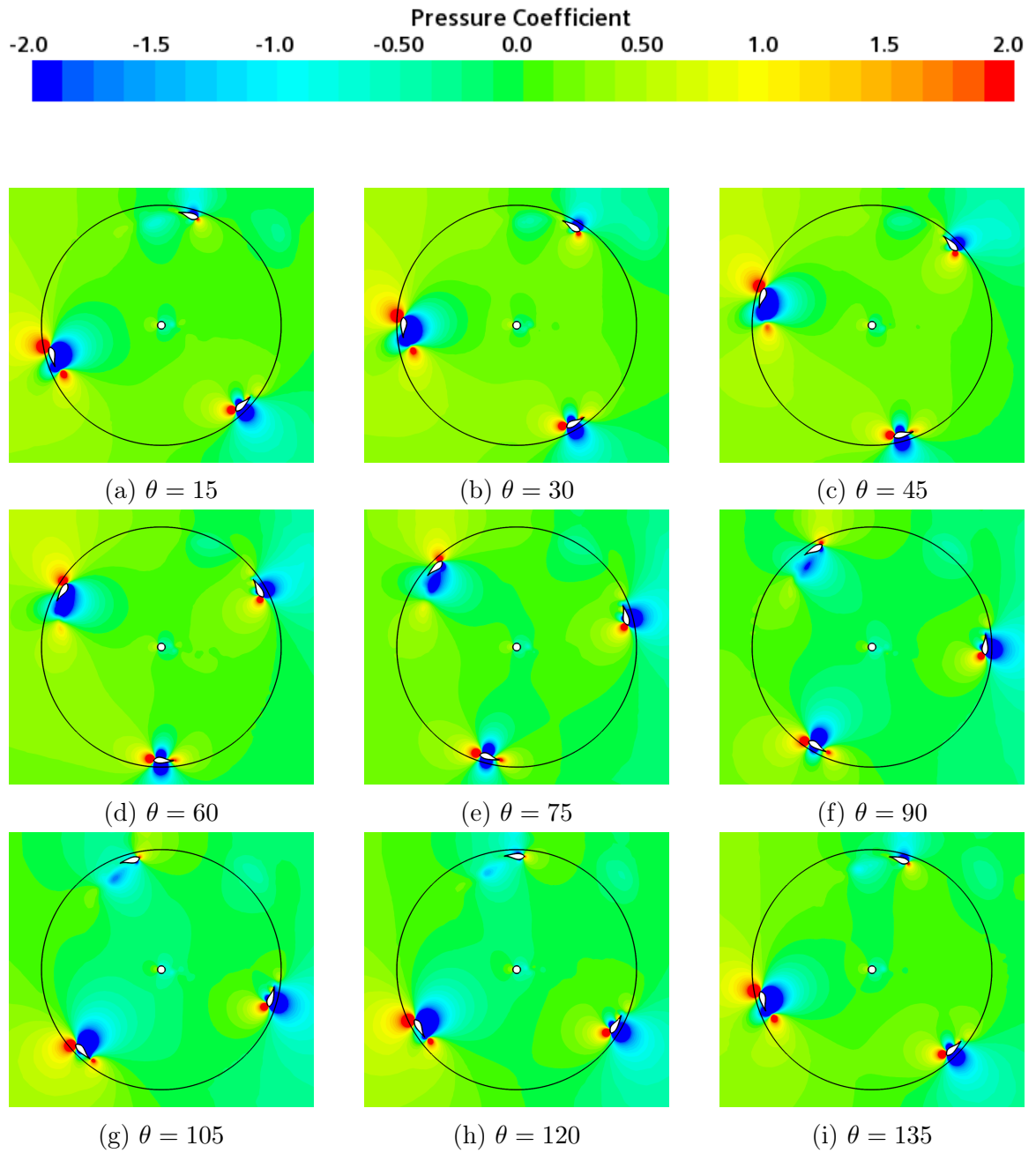


Figure 5.20: Pressure coefficient contours for the right turbine over a third of a revolution from  $\theta = 15$  to  $\theta = 135$

### 5.1.5 Dynamic Performance Analysis

The overall performance of the counter-rotating system is based on the average power coefficient calculated in the tip speed ratio study. The average overall power coefficient for the most optimal tip speed ratio of 2.75 was calculated as 0.4895. The power coefficient in this context can be considered the aerodynamic efficiency. This aerodynamic efficiency is how efficiently the blades take the flow's kinetic energy and transfer it to the turbine shaft's mechanical energy. The aerodynamic efficiency is where the most significant losses in a turbine system are located. The maximum aerodynamic efficiency of any turbine is  $16/27$  (59.3%) according to Betz's law, or a power coefficient of 0.593 [71]. The other two areas that contribute to overall efficiency are mechanical losses and electrical losses. The proposed system has eliminated the gearbox to reduce mechanical losses. Therefore, the only other losses are due to converting the power generated from the shaft into usable electrical energy. The performance in terms of total power generated in this section is based on the aerodynamic efficiency, not the overall efficiency. However, the losses due to electrical efficiency are small; therefore, the calculated power approximates the actual power output and helps determine suitable applications for small and larger-scale turbine systems.

The performance in terms of the power of the small-scale prototype used in the PIV experimentation along with full-scale-sized turbines is analyzed in this thesis. Many applications of marine turbines require different power outputs, and therefore both sizes are analyzed. There are some applications where a full-scale turbine would not be appropriate such as in areas where size is a concern. There are some applications, such as water desalination, where reliability is more important than the overall magnitude of power output that a full-scale turbine could provide.

Multiple full-scale-sized turbines are analyzed to show their power outputs. All turbine sizes are increased proportionally to the small-scale turbine to ensure that

the same power coefficient can be applied. The performance of the full-scale turbine systems was achieved by using the concept of similitude. In typical aerodynamic scaling, the small-scale and full-scale models must meet three criteria: geometrical, kinematic, and dynamic similitude. The geometrical similitude is defined as both models having the same geometrical proportions. The kinematic similarity is defined as the velocity at any point on the scaled model must be proportional to the velocity at any point on the full-scale model. The third and most critical criterion is dynamic similarity. The inertial to viscous forces ratio must be equal for both the scale and full-size models. The ratio of these two forces is defined as the Reynolds number and given in equation 3.28.

When specifically scaling a turbine, these three criteria are met by ensuring the following are valid for the small and large scale. The first is that both turbines must operate at the same tip speed ratio. The second is that the blade profiles, number of blades, and surface material must be equal. The third is that the full-scale model was scaled from the small scale size in all dimensions, including overall radius, height, and chord length. All of these were met by scaling the turbine proportionally and using the same tip speed ratio of 2.75, allowing the same power coefficient of 0.4895 to be used for the large-scale turbines. Table 5.4 below shows the radius, height, swept area, and overall power generated for the 3D geometry of both the small-scale and different large-scale turbines.

Table 5.4: Small-scale and full-scale turbine geometry parameters

Size Factor	Radius ( $m$ )	Height ( $m$ )	Swept Area ( $m^2$ )	Power( $w$ )
Small Scale	0.2540	0.2159	0.1097	26.76
2	0.4318	0.5080	0.4387	107.05
5	1.0795	1.2700	2.7419	669.04
10	2.1590	2.5400	10.9677	2676.17

The small-scale turbine was analyzed along with three full-sized turbines at 2, 5, and 10 times the size. The average power coefficient is the most accurate way to characterize the performance of a turbine when compared with different designs and operating conditions. Since this analysis is a phase one study, many factors were not considered that could impact how much overall power is generated. This is especially true due to the generator design and potential losses with electrical output not factoring into the numbers. However, it is essential to estimate how much power the turbine system generates at the prototype scale and how much it produces when scaled up to different sizes. It is possible to calculate the power generated for full-scale turbines based on the average power coefficient and the total amount of potential energy flowing into that given turbine, given a proportional-sized turbine system and an operating tip speed ratio of 2.75. The power curve based on the turbine size was calculated for the optimal tip speed ratio of 2.75 and two smaller tip speed ratios of 2.5 and 2. Figure 5.21 shows the total power based on the turbine radius.

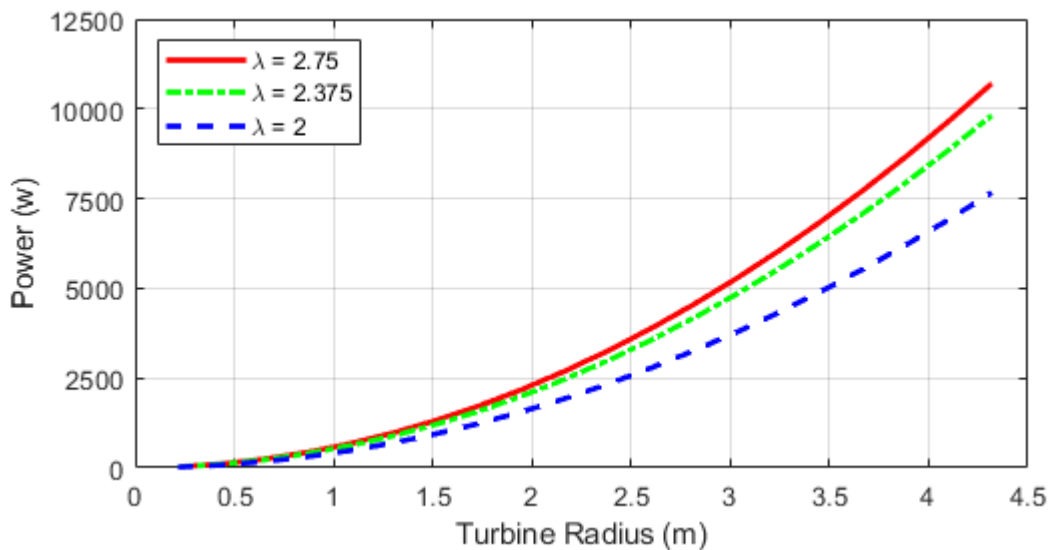


Figure 5.21: Power output as a function of turbine radius for various tip speed ratios

Since cavitation is an issue with a tip speed ratio of 2.75, the turbine might need to be operated at a lower tip speed ratio which would lower the power output. It

can be seen from figure 5.21 that a decrease in tip speed ratio does affect the power output. The power produced from lower speed tip speed ratios seems to be within an order of magnitude of the energy created from the optimal tip speed ratio of 2.75.

## CHAPTER 6: CONCLUSIONS

The ultimate goal of this work was to conduct a computational design analysis study of a hydrokinetic horizontal parallel stream direct-drive (no gearbox) counter-rotating Darrieus turbine system. A two-dimensional (2D) and three-dimensional (3D) computational fluid dynamic (CFD) simulation study was conducted to assess the hydrokinetic performance of the design. Results such as power coefficient, pressure coefficient, flow pattern behavior, torque coefficient, and ripple effect, which provide information on torque smoothing, were obtained and discussed. The flow analysis also showed that the hydrofoils generate sufficient lift to rotate, extract the energy from the flow, and produce the optimum power needed.

- The DD-VADHT design presented in this work appears to be able to extract more energy from a double-swept area than a single-swept area as compared to previous designs when analyzing the ripple effect, torque coefficient, and power coefficient.
- The DD-VADHT design promises reasonable torque smoothing and possibly good self-starting capabilities. However, more work should be done (i.e., CFD, one-dimensional data code analyses, and experimental analysis) for verification.
- The counter-rotating element of the DD-VADHT design appears to produce a higher power output than a single-rotor design.

There are multiple aspects of the analysis that were not covered in this thesis that should be considered in future research. These involve more in-depth simulations to understand the current design's flow field and possible geometry changes to increase the overall turbine hydrodynamic efficiency further.

- Transient 3D CFD simulation studies to further investigate the flow field in the region between blades and determine a more accurate optimal tip speed ratio that considers tip effects.
- Use a Large-Eddy Simulation (LES) study for analyzing recirculating regions and eddies around curved surfaces and between the rotating domains.
- Analyze different blade shapes in a counter-rotating system for overall efficiency and the torque ripple effect to determine the most efficient turbine rotor configuration.
- Dynamic Fluid Body Interaction studies to allow flow to rotate the turbine and test how the rotational velocity varies with the change in inlet velocity.
- Run a transient PIV experiment with a smaller scale model that has the framing removed in combination with a periscope laser to understand the counter-rotating blade interaction

## Bibliography

- [1] A. Olabi and M. Abdelkareem, *Energy storage systems towards 2050*, 2021.
- [2] X.-W. Han, W.-B. Zhang, X.-J. Ma, X. Zhou, Q. Zhang, X. Bao, Y.-W. Guo, L. Zhang, and J. Long, “Technologies and materials for water salinity gradient energy harvesting,” *Journal of The Electrochemical Society*, 2021.
- [3] C. Xia, Y. Zhu, S. Zhou, H. Peng, Y. Feng, W. Zhou, J. Shi, and J. Zhang, “Simulation study on transient performance of a marine engine matched with high-pressure scr system,” *International Journal of Engine Research*, p. 14 680 874 221 084 052, 2022.
- [4] L. Ren, F. Kong, X. Wang, Y. Song, X. Li, F. Zhang, N. Sun, H. An, Z. Jiang, and J. Wang, “Triggering ambient polymer-based li-o<sub>2</sub> battery via photo-electro-thermal synergy,” *Nano Energy*, vol. 98, p. 107 248, 2022.
- [5] S. Shafiee and E. Topal, “When will fossil fuel reserves be diminished?” *Energy policy*, vol. 37, no. 1, pp. 181–189, 2009.
- [6] J. S. Apte, J. D. Marshall, A. J. Cohen, and M. Brauer, “Addressing global mortality from ambient pm<sub>2.5</sub>,” *Environmental science & technology*, vol. 49, no. 13, pp. 8057–8066, 2015.
- [7] I. C. Dedoussi and S. R. Barrett, “Air pollution and early deaths in the united states. part ii: Attribution of pm<sub>2.5</sub> exposure to emissions species, time, location and sector,” *Atmospheric environment*, vol. 99, pp. 610–617, 2014.
- [8] Q. Di, Y. Wang, A. Zanobetti, Y. Wang, P. Koutrakis, C. Choirat, F. Dominici, and J. D. Schwartz, “Air pollution and mortality in the medicare population,” *New England Journal of Medicine*, vol. 376, no. 26, pp. 2513–2522, 2017.
- [9] H. D. Pritchard, J. Turner, *et al.*, “State of the global climate in 2020,” 2021.

- [10] K. Vohra, A. Vodonos, J. Schwartz, E. A. Marais, M. P. Sulprizio, and L. J. Mickley, "Global mortality from outdoor fine particle pollution generated by fossil fuel combustion: Results from geos-chem," *Environmental Research*, vol. 195, p. 110 754, 2021.
- [11] O. Ellabban, H. Abu-Rub, and F. Blaabjerg, "Renewable energy resources: Current status, future prospects and their enabling technology," *Renewable and sustainable energy reviews*, vol. 39, pp. 748–764, 2014.
- [12] K. Gunn and C. Stock-Williams, "Quantifying the global wave power resource," *Renewable Energy*, vol. 44, pp. 296–304, 2012.
- [13] K. Soleimani, M. J. Ketabdari, and F. Khorasani, "Feasibility study on tidal and wave energy conversion in iranian seas," *Sustainable Energy Technologies and Assessments*, vol. 11, pp. 77–86, 2015.
- [14] T. J. Hammons, "Tidal power," *Proceedings of the IEEE*, vol. 81, no. 3, pp. 419–433, 1993.
- [15] P. G. Novo and Y. Kyojuka, "Tidal stream energy as a potential continuous power producer: A case study for west japan," *Energy Conversion and Management*, vol. 245, p. 114 533, 2021.
- [16] M. Chowdhury, K. S. Rahman, V. Selvanathan, N. Nuthammachot, M. Suklung, A. Mostafaeipour, A. Habib, M. Akhtaruzzaman, N. Amin, and K. Techato, "Current trends and prospects of tidal energy technology," *Environment, development and sustainability*, vol. 23, no. 6, pp. 8179–8194, 2021.
- [17] D. Dunnett and J. S. Wallace, "Electricity generation from wave power in canada," *Renewable Energy*, vol. 34, no. 1, pp. 179–195, 2009.
- [18] M. Khanjanpour, A. Javadi, and M. Akrami, "Cfd analyses of a tidal hydro-turbine (tht) for utilising in sea water desalination," 2019.

- [19] P. des Nations unies pour le développement, N. Unies, and C. mondial de l'énergie, *World energy assessment: energy and the challenge of sustainability*. United Nations development programme, 2000.
- [20] F. d. O. Antonio, "Wave energy utilization: A review of the technologies," *Renewable and sustainable energy reviews*, vol. 14, no. 3, pp. 899–918, 2010.
- [21] A. Gallego, J. Side, S. Baston, S. Waldman, M. Bell, M. James, I. Davies, R. Murray, M. Heath, A. Sabatino, *et al.*, "Large scale three-dimensional modelling for wave and tidal energy resource and environmental impact: Methodologies for quantifying acceptable thresholds for sustainable exploitation," *Ocean & Coastal Management*, 2016.
- [22] M. Träsch, A. Déporte, S. Delacroix, G. Germain, B. Gaurier, and J.-B. Drevet, "Wake characterization of an undulating membrane tidal energy converter," *Applied Ocean Research*, vol. 100, p. 102222, 2020.
- [23] P. Damacharla and A. J. Fard, "A rolling electrical generator design and model for ocean wave energy conversion," *Inventions*, vol. 5, no. 1, p. 3, 2020.
- [24] W. Liu, L. Liu, H. Wu, Y. Chen, X. Zheng, N. Li, and Z. Zhang, "Performance analysis and offshore applications of the diffuser augmented tidal turbines," *Ships and Offshore Structures*, pp. 1–10, 2022.
- [25] M. Mohamed, "Performance investigation of h-rotor darrieus turbine with new airfoil shapes," *Energy*, vol. 47, no. 1, pp. 522–530, 2012.
- [26] W. Batten, A. Bahaj, A. Molland, J. Chaplin, S. E. R. Group, *et al.*, "Experimentally validated numerical method for the hydrodynamic design of horizontal axis tidal turbines," *Ocean engineering*, vol. 34, no. 7, pp. 1013–1020, 2007.
- [27] J. Thiébot, P. B. Du Bois, and S. Guillou, "Numerical modeling of the effect of tidal stream turbines on the hydrodynamics and the sediment transport–

- application to the alderney race (raz blanchard), france,” *Renewable Energy*, vol. 75, pp. 356–365, 2015.
- [28] W. Batten, A. Bahaj, A. Molland, and J. Chaplin, “Hydrodynamics of marine current turbines,” *Renewable energy*, vol. 31, no. 2, pp. 249–256, 2006.
- [29] M. E. H. Al-Kharbasy, “Enhancement protection and operation of the doubly fed induction generator during grid fault,” *South Valley University-Qena-Egypt*, 2012.
- [30] D. G. J. Marie, *Turbine having its rotating shaft transverse to the flow of the current*, US Patent 1,835,018, Dec. 1931.
- [31] F. Castellani, D. Astolfi, M. Peppoloni, F. Natili, D. Buttà, and A. Hirschl, “Experimental vibration analysis of a small scale vertical wind energy system for residential use,” *Machines*, vol. 7, no. 2, p. 35, 2019.
- [32] S. Antheaume, T. Maitre, and J.-L. Achard, “Hydraulic darrieus turbines efficiency for free fluid flow conditions versus power farms conditions,” *Renewable Energy*, vol. 33, no. 10, pp. 2186–2198, 2008.
- [33] M. R. Castelli, A. Englaro, and E. Benini, “The darrieus wind turbine: Proposal for a new performance prediction model based on cfd,” *Energy*, vol. 36, no. 8, pp. 4919–4934, 2011.
- [34] M. Islam, D. S.-K. Ting, and A. Fartaj, “Aerodynamic models for darrieus-type straight-bladed vertical axis wind turbines,” *Renewable and sustainable energy reviews*, vol. 12, no. 4, pp. 1087–1109, 2008.
- [35] R. Templin, “Aerodynamic performance theory for the nrc vertical-axis wind turbine,” National Aeronautical Establishment, Ottawa, Ontario (Canada), Tech. Rep., 1974.
- [36] R. E. Wilson and P. Lissaman, “Applied aerodynamics of wind power machines,” 1974.

- [37] I. Paraschivoiu, “Double-multiple streamtube model for studying vertical-axis wind turbines,” *Journal of propulsion and power*, vol. 4, no. 4, pp. 370–377, 1988.
- [38] H. Larsen, “Summary of a vortex theory of the cyclogiro, proceedings of the 2<sup>nd</sup> us national conference on wind engineering research,” *Colorado State University*, vol. 8, 1975.
- [39] J. H. Strickland, B. Webster, and T. Nguyen, “A vortex model of the darrieus turbine: An analytical and experimental study,” 1979.
- [40] I. H. Hirsch and A. Mandal, “A cascade theory for the aerodynamic performance of darrieus wind turbines,” *Wind Engineering*, pp. 164–175, 1987.
- [41] T. Maitre, J.-L. Achard, L. Guittet, and C. Ploesteanu, “Marine turbine development: Numerical and experimental investigations,” *Scientific Bulletin of the Politehnica University of Timisoara*, no. 50 (64), pp. 59–66, 2005.
- [42] J. A. Clarke, G. Connor, A. Grant, and C. Johnstone, “Design and testing of a contra-rotating tidal current turbine,” *Proceedings of the Institution of Mechanical Engineers, Part A: Journal of Power and Energy*, vol. 221, no. 2, pp. 171–179, 2007.
- [43] Y. Usui, T. Kanemoto, and K. Hiraki, “Counter-rotating type tidal stream power unit boarded on pillar (performances and flow conditions of tandem propellers),” *Journal of Thermal Science*, vol. 22, no. 6, pp. 580–585, 2013.
- [44] D. H. Didane, N. Rosly, M. F. Zulkaffi, and S. S. Shamsudin, “Performance evaluation of a novel vertical axis wind turbine with coaxial contra-rotating concept,” *Renewable Energy*, vol. 115, pp. 353–361, 2018.
- [45] A. Janon and T. Boonsuk, “A parametric study of starting time profile for a novel direct-drive vertical axis darrieus hydrokinetic turbine with an axial-flux

- permanent magnet generator,” in *2019 9th International Conference on Power and Energy Systems (ICPES)*, IEEE, 2019, pp. 1–6.
- [46] A. Janon, K. Sangounsak, and W. Sriwannarat, “Making a case for a non-standard frequency axial-flux permanent-magnet generator in an ultra-low speed direct-drive hydrokinetic turbine system,” *AIMS Energy*, vol. 8, no. 2, pp. 156–168, 2020.
- [47] Y. Hara, N. Horita, S. Yoshida, H. Akimoto, and T. Sumi, “Numerical analysis of effects of arms with different cross-sections on straight-bladed vertical axis wind turbine,” *Energies*, vol. 12, no. 11, p. 2106, 2019.
- [48] H. Abusannuga and M. Özkaymak, “The effect of geometry variants on the performance of vawt-rotor with incline-straight blades,” *AIP Advances*, vol. 11, no. 4, p. 045307, 2021.
- [49] T. Villeneuve, G. Winckelmans, and G. Dumas, “Increasing the efficiency of vertical-axis turbines through improved blade support structures,” *Renewable Energy*, vol. 169, pp. 1386–1401, 2021.
- [50] M. Mosbahi, A. Ayadi, Y. Chouaibi, Z. Driss, and T. Tucciarelli, “Experimental and numerical investigation of the leading edge sweep angle effect on the performance of a delta blades hydrokinetic turbine,” *Renewable Energy*, vol. 162, pp. 1087–1103, 2020.
- [51] V. Jayaram and B. Bavanish, “A brief study on the implementation of helical cross-flow hydrokinetic turbines for small scale power generation in the indian shp sector,”
- [52] S. Yagmur and F. Kose, “Numerical evolution of unsteady wake characteristics of h-type darrieus hydrokinetic turbine for a hydro farm arrangement,” *Applied Ocean Research*, vol. 110, p. 102582, 2021.

- [53] I. A. Tunio, M. A. Shah, T. Hussain, K. Harijan, N. H. Mirjat, and A. H. Memon, “Investigation of duct augmented system effect on the overall performance of straight blade darrieus hydrokinetic turbine,” *Renewable Energy*, vol. 153, pp. 143–154, 2020.
- [54] M. Basumatary, A. Biswas, and R. D. Misra, “Experimental verification of improved performance of savonius turbine with a combined lift and drag based blade profile for ultra-low head river application,” *Sustainable Energy Technologies and Assessments*, vol. 44, p. 100 999, 2021.
- [55] M. Mosbahi, M. Derbel, M. Lajnef, B. Mosbahi, Z. Driss, C. Aricò, and T. Tucciarelli, “Performance study of twisted darrieus hydrokinetic turbine with novel blade design,” *Journal of Energy Resources Technology*, vol. 143, no. 9, 2021.
- [56] S. Yagmur, F. Kose, and S. Dogan, “A study on performance and flow characteristics of single and double h-type darrieus turbine for a hydro farm application,” *Energy Conversion and Management*, vol. 245, p. 114 599, 2021.
- [57] J. M. Crooks, R. L. Hewlin, and W. B. Williams, “Computational design analysis of a hydrokinetic horizontal parallel stream direct drive counter-rotating darrieus turbine system: A phase one design analysis study,” *Energies*, vol. 15, no. 23, p. 8942, 2022.
- [58] A. Sleiti and J. Kapat, “Comparison between evm and rsm turbulence models in predicting flow and heat transfer in rib-roughened channels,” in *Heat Transfer Summer Conference*, vol. 46911, 2004, pp. 531–542.
- [59] M. A. Allard, “Performance and wake analysis of a darrieus wind turbine on the roof of a building using cfd,” Ph.D. dissertation, Concordia University, 2020.
- [60] G. Alfonsi, “Reynolds-averaged navier–stokes equations for turbulence modeling,” *Applied Mechanics Reviews*, vol. 62, no. 4, 2009.

- [61] J. R. Khan, "Comparison between discrete phase model and multiphase model for wet compression," in *Turbo Expo: Power for Land, Sea, and Air*, American Society of Mechanical Engineers, vol. 55195, 2013, V05AT20A010.
- [62] A. Alaimo, A. Esposito, A. Messineo, C. Orlando, and D. Tumino, "3d cfd analysis of a vertical axis wind turbine," *Energies*, vol. 8, no. 4, pp. 3013–3033, 2015.
- [63] T. J. Hall, *Numerical simulation of a cross flow marine hydrokinetic turbine*. University of Washington, 2012.
- [64] I. Murgan, F. Bunea, A. Nedelcu, and G. D. Ciocan, "Experimental setup to study two phase flows for environmental applications," in *E3S Web of Conferences*, EDP Sciences, vol. 85, 2019, p. 07 010.
- [65] M. Raffel, C. E. Willert, J. Kompenhans, *et al.*, *Particle image velocimetry: a practical guide*. Springer, 1998, vol. 2.
- [66] S. E. Hellman, "Experimental investigation of turbulent wake structures and dynamic coupling of tandem lifting bodies in a hydrodynamic channel," Ph.D. dissertation, The University of North Carolina at Charlotte, 2012.
- [67] W. Thielicke and E. Stamhuis, "Pivlab—towards user-friendly, affordable and accurate digital particle image velocimetry in matlab," *Journal of open research software*, vol. 2, no. 1, 2014.
- [68] R. D. Keane and R. J. Adrian, "Theory of cross-correlation analysis of piv images," *Applied scientific research*, vol. 49, no. 3, pp. 191–215, 1992.
- [69] P. J. Roache, "Perspective: A method for uniform reporting of grid refinement studies," 1994.
- [70] Y. Nabavi, "Numerical study of the duct shape effect on the performance of a ducted vertical axis tidal turbine," Ph.D. dissertation, University of British Columbia Vancouver, BC, Canada, 2008.

- [71] A. Betz, *Introduction to the theory of flow machines*. Elsevier, 2014.